2013

# Raman-based imaging and thermal characterization in near-field laser heating

Xiaoduan Tang
*Iowa State University*

# Raman-based imaging and thermal characterization in near-field laser heating

by

**Xiaoduan Tang**

A dissertation submitted to the graduate faculty

in partial fulfillment of the requirements for the degree of

DOCTOR OF PHILOSOPHY

Major: Mechanical Engineering

Program of Study Committee:
Xinwei Wang, Major Professor
Gap-Yong Kim
William Ross Morrow
Chenxu Yu
Wei Hong

Iowa State University
Ames, Iowa
2013

**TABLE OF CONTENTS**

## LIST OF FIGURES

# LIST OF TABLES

## ACKNOWLEDGEMENTS

I would like to first thank my advisor Dr. Xinwei Wang for the opportunity to work on these advanced projects and experience the complete research process. Without Dr. Wang's continuous guidance and support, I would not have been able to obtain these great achievements. The valuable discussions with Dr. Wang encouraged me to solve research problems and motivated me to achieve my goals persistently. The helpful and friendly attitude of my advisor was of great encouragement and happiness in my PhD's study. The edification from Dr. Wang would be beneficial for my whole life.

In addition, I would like to thank Dr. Gap-Yong Kim, Dr. William Ross Morrow, Dr. Chenxu Yu, and Dr. Wei Hong for serving in my committee. I am also grateful to Dr. Cheryl Ann Farr and Dr. Song Zhang for providing a review of my work. I want to also offer my appreciation to all of my colleagues in the Micro/Nanoscale Thermal Science Laboratory who provided assistance to me during my study, especially Shen Xu, Jingchao Zhang, Guoqing Liu, Xiangwen Chen, and Yanan Yue. Thanks to my friends for making my time at Iowa State University a memorable experience. The financial support of this work by the National Science Foundation (CMMI-0926704, CMMI-1200397, and CBET-0932573) is gratefully acknowledged.

Lastly but not the least, I would like to thank my family for their encouragement and my wife Can Zhu for her invaluable support, respect and love. Without my wife's continuous encouragement and help, I would not have been able to finish this work. Her good-to-

excellent care is the foundation of my success in my doctoral study. The happiness and painfulness shared with her is of great value in my life. It is the interaction of our life makes me enjoy the colorful and meaningful world.

## ABSTRACT

Micro/nanoparticle induced near-field laser ultra-focusing and heating has been widely used in laser-assisted nanopatterning and nanolithography to pattern nanoscale features on a large-area substrate. Probing of the temperature, stress, and optical fields induced by the nanoscale near-field laser heating remains a great challenge since the heating area is very small (~100 nm or less) and not immediately accessible for sensing. Raman scattering method is a promising tool for noncontact temperature and thermal stress measurements.

In this work, the first experimental study is reported on nanoscale mapping and thermal probing of particle- and fiber-induced thermal, stress, and optical fields by using a single laser for both near-field excitation and Raman probing. The mapping results based on Raman intensity variation, wavenumber shift, and linewidth broadening all give consistent conjugated thermal, stress, and near-field focusing effects with an accuracy of 20 nm ($< \lambda/26$, $\lambda = 532$ nm). Nanoscale mapping of near-field effects of monolayer microparticles, a single microparticle, and a single microfiber demonstrates the strong capacity of such technique. A new strategy has been developed to de-conjugate the effects of temperature, stress, and near-field focusing from Raman mapping. The temperature rise and stress in the nanoscale heating region is evaluated at different particle diameters and laser energy levels. For stronger laser fluence and larger particle size, the corresponding temperature and stress are higher. With a laser fluence of $3.9\times10^9$ W/m$^2$ and for a single 1.21 μm silica particle induced laser heating, the maximum temperature rise and local stress are 58.5 K and 160 MPa, respectively. Experimental results are explained and consistent with three-dimensional high-fidelity

optical, thermal, and stress field simulations.

Graphene has attracted great research interests owing to its unique mechanical and electronic properties. In its application, graphene is of high possibility to be supported by a bulk substrate in 3-D devices. The knowledge of the interfacial phonon coupling and the energy exchange capacity at graphene/substrate interfaces is critical in the heat dissipation of graphene-based devices. In this work, the interfacial thermal characterization at CVD graphene/Si, epitaxial graphene/SiC, and CVD graphene/glass interfaces are explored. Temperature differences of graphene layers and the adjacent substrates under laser heating are distinguished at the nanoscale simultaneously by Raman spectroscopy. Linewidth broadening yields interfacial thermal resistances of graphene/Si, graphene/SiC, and graphene/glass as $5.46\times10^{-3}$, $2.27\times10^{-3}$, and $3.76\times10^{-3}$ $Km^2W^{-1}$, respectively. The experimental results are much higher than the molecular dynamics simulation results. The high thermal contact resistances indicate poor contact at the interfaces. The wavenumber method reveals consistent results with the linewidth method, suggesting little stress experienced in the graphene. The thermal resistances obtained by intensity methods are significantly smaller than that based on linewidth and wavenumber methods. Light interference at the air layer between graphene and substrate interprets the small thermal resistance values based on intensity, which further proves the rough contact. Strategies are developed to evaluate the increments of separation distances between graphene and substrates after laser heating. AFM images are taken to verify the corrugation of graphene on substrates and the increments of separation distances after heating.

# CHAPTER 1. INTRODUCTION

Micro/nanoscale particles play an important role in many fields due to their characteristic optical properties, large surface to volume ratio and large surface energy. Bar *et al.* reported that the microstructure of monolayer particles is a significant factor determining the optical properties of dendrimer-modified silicon oxide surfaces [1]. The reflectivity of glasses is reduced without sacrificing other optical properties due to monolayers of small silica particles [2]. Natural opal skeleton can be achieved from 3-D ordered small silica particles [3]. Artificially produced opals can be used to study photonic band gap phenomena [4]. Uniform nanoparticles have novel optical properties [5], and can be used to synthesize opaline materials which exhibit photonic band gaps effect in the visible range [6]. Nanoparticles can be used to produce nanotextured surfaces with enhanced physical and/or chemical properties, known as nanotexturing. Nanotexturing can also make substrates superhydrophobic or superhydrophilic, depending on the surface chemistry [7, 8]. Metal nanoparticles are suitable materials for fabricating conductive features such as electrodes, conductive lines, and conductive patterns, due to their low temperature melting ability [9]. Monolayer layer of nanoparticles are attractive due to the generation of surface textures [10]. Surface textures used in optically enhanced solar cells and high-resolution x-ray detectors have all been produced using self-assembly. It is known that spherical particles can act as spherical lens and heat the substrates under laser irradiation [11]. A laser beam can be focused in a small area of sub-wavelength in dimension by micro/nano particles. Particles-induced damage in the irradiated surface area has been reported [12]. Laser-assisted nanopatterning and nanoimprinting lithography has been proved to be able to pattern sub-10

nm features on a large-area substrate [13-19]. Large-area fabrication of nanoscale photonic structures using laser-assisted nanoimprinting of self-assembled particles has been reported [13]. Pit arrays have been created on metallic surfaces using particle-enhanced laser irradiation [20].

### 1.1. Near-field Laser Focusing

Due to the wide application of particles, theoretical studies about optical field enhancement by micro/nano particles have been reported. Analytical calculations [21, 22] of a dielectric sphere under laser irradiation has been performed by using the Mie scattering theory [23]. Li *et al.* employed HFSS software to simulate the optical field distribution of a model [14, 15], in which an 800 nm silica particle was placed on an aluminum film under normally irradiated laser beam ($\lambda$ = 248 nm). Due to the laser focusing by the silica particle, the magnitude of electric field increased 6-7 times. McLeod *et al.* developed a finite-difference time-domain (FDTD) model for light ($\lambda$ = 355 nm) passing through a 760 nm polystyrene particle in water on a polyimide substrate [16]. It is reported that the intensity of light increased by about 14 times relative to the incident wave. Another method was also developed to solve the "particle-on-substrate" problem: a silica particle (D = 950 nm) on an aluminum surface under a laser beam ($\lambda$ = 248 nm) [20, 24], which showed that the laser fluence at the contacting point between particle and substrate was greatly enhanced with an optical enhancement of 14. Only a few articles reported the temperature calculation inside a substrate beneath particles under laser irradiation. Simulation of laser interaction with materials (SLIM) was used to theoretically calculate the temperature of a substrate beneath particles with laser irradiation [15, 20]. To our knowledge, no experiment about temperature

measurement inside a substrate under micro/nano particles has been reported. Such measurement is very challenging since the near-field heating area in the substrate is quite small, usually around 200 nm or even smaller. In addition, this area is just below the particle, so retrieving the thermal information of this region is really difficult. As there is a research gap in near-field heating and thermal probing using the laser method, it is of great importance to conduct symmetric experimental and simulation research regarding temperature inside a substrate-particle system.

### 1.2. Nanoscale Surface Thermal and Stress Imaging

The conventional optical microscope is diffraction-limited in imaging resolution to about half of the illuminating wavelengths. Some near-field techniques can help to improve the resolution, which is achieved by placing the detector very close to the object. Scanning probe microscopy (SPM) without light probe has been invented and developed in 1980's. Scanning tunneling microscopy (STM) and atomic force microscopy (AFM), utilizing a tunneling current and force between the tip and the sample respectively, can image surfaces at the atomic level. With light probe, near-field scanning optical microscopy (NSOM) is capable of breaking the optical resolution limit by extensively employing the properties of evanescent waves. NSOM can achieve an image resolution smaller than 100 nm, substantially lower than the wavelength of light. It has been improved down to 25 nm by using a tip-on-aperture probe [25]. More recently, optical imaging at 1 nm scale resolution was achieved using interferometric apertureless NSOM [26]. However, NSOM has slow scanning speed and low imaging depth and the probe must be very close to the object. Taubner *et al.* improved subwavelength imaging of buried objects by using a silicon carbide superlens based near-

field microscopy [27]. Another superlens used a silver slab with periodic corrugations to enhance the evanescent waves of an object and convert them into propagating waves, so that the object could be imaged in the far-field [28]. The superlens was physically placed in the near-field of an object, however. An imaging technique called stochastic optical reconstruction microscopy (STORM) provided a high imaging resolution of approximately 20 nm by controlling the fluorescence emission from a single molecule, limited only by the number of photons emitted per switch cycle [29].

Whereas these techniques are nearsighted, FSLs capable of imaging beyond the diffraction limit in the far field were developed. A FSL used optically transparent microspheres to overcome the diffraction limit with a resolution between $\lambda/8$ and $\lambda/14$ [30]. A spherical hyperlens was designed to project 2-D near-field optical images with hyperbolic dispersion and reached a 160 nm resolution ($\lambda/2.6$) [31]. A magnifying superlens based on a multilayer photonic metamaterial consisting of alternating layers of positive and negative refractive index was demonstrated with a resolution of 70 nm ($\lambda/7$) [32]. A magnifying optical cylindrical hyperlens consisting of a curved periodic stack deposited on a half-cylindrical cavity was capable of sub-diffraction-limited imaging at a resolution of 130 nm ($\lambda/2.8$) [33]. Nanoscale solid immersion lenses (nSILs) were developed for high-quality imaging which can resolve 220 nm line objects ($\lambda/2.2$) [34]. However, it is hard to resolve objects below 50 nm with visible light.

Regarding nanoscale surface thermal and stress imaging, scanning thermal microscopy

(SThM) has been reported as an established technique to measure nanoscale temperature distributions by attaching a temperature sensor on the apex of a tiny tip. The imaging of phonon temperature distribution for electrically heated carbon nanotube circuits was reported with a spatial resolution of ~50 nm [35]. A near-field SThM (NSThM) operating in ultrahigh vacuum was developed to provide thermal imaging for a sample with a resolution of a few nanometers [36]. In thermometry, apertureless NSOM has been proposed by using AFM tip or nanoparticle. Temperature probing of silicon under AFM tip focused laser heating at a sub-10 nm scale was conducted via apertureless NSOM based on Raman thermometry [37]. Nanoscale thermal probing of graphene on 4H-SiC in the thickness direction was reported using Raman spectrometer with a resolution down to 1 nm [38]. The temperatures of graphene (1 nm thickness) and SiC (a few microns) were measured and distinguished by studying their distinct Raman peaks. Surface stress mapping in a doped polysilicon microheater and a silicon microcantilever has been reported using Raman spectroscopy [39, 40]. Recently, Reserbat-Plantey *et al.* developed a non-invasive optical probe to provide stress mapping at nanoscale within a nanoelectromechanical system by combining Raman spectroscopy with Fizeau interferometry [41]. Raman spectroscopy is employed in this work as it is a unique far-field technique sensitive to both temperature and stress fields [39, 40].

### 1.3. Interfacial Thermal Characterization between Graphene and Substrate

As a two dimensional material, graphene exhibits unique physical properties, which gives the opportunity for broad potential applications [42-45]. Measurements of thermal conductivity of graphene revealed a high value from 630-5300 $Wm^{-1}K^{-1}$ in a temperature range of 300-600 K [46-49]. Molecular dynamics simulations determined an even higher

thermal conductivity from 8,000-10,000 W $m^{-1}$ $K^{-1}$ at room temperature for graphene sheets [50]. Balandin reviewed the thermal properties of graphene and indicated the prospects of applications of graphene for thermal design of electronics [51]. The ultra-high thermal conductivity of graphene prompts potential applications for heat removal in semiconductor devices [46, 52-54]. It is possible for this two dimensional material to effectively dissipate heat in the next generation 3-D electronics. In its application, graphene is either supported by a bulk substrate or embedded in a 3-D structure, for a two dimensional material cannot exist in the free-standing state. Heat dissipation in the in-plane direction would be greatly impeded due to the thin thickness of graphene (0.35 nm for a single layer) [46, 47]. The thermal transport to the adjacent materials plays the major role in heat dissipation on graphene based electronic devices. Therefore, the knowledge of energy coupling at the interface is important to evaluate this out-of-plane heat dissipation.

To this end, very little research has been done on thermal transport at the interface between graphene and its substrate [38, 55-58]. The first work by Chen *et al.* used a second metal coating (Au) on a sandwiched graphene between two $SiO_2$ layers to facilitate the measurement with the 3ω technique [55]. Koh *et al.* and Hopkins *et al.* reported the thermal conductance at Au/Ti/graphene/$SiO_2$ and Al/graphene/$SiO_2$ interfaces [56, 57]. In these ways, the graphene was sandwiched between structures, and the flexural phonon behavior was strongly constrained. Also the graphene-substrate contact can be significantly altered during this sandwiched structure preparation. The thermal conductance of the graphene/$SiO_2$ interface was determined varying from 2,000 to 11,000 $Wcm^{-2}K^{-1}$ by Mak *et al.* in 2010 [58]. The large dispersion reflected the relatively poorly defined nature of interface between

exfoliated graphene and $SiO_2$. Work by Yue *et al.* reported a anomalous interfacial thermal resistance as $5.30\times10^{-5}$ $Km^2W^{-1}$ between epitaxial graphene and SiC [38]. The reason was speculated to be the delamination of graphene and SiC at the interface under heating. The contact condition at the graphene and substrate interface is a main factor in determining the interfacial phonon coupling and energy exchange. In the study of free-standing graphene, it has been demonstrated that ripples are an intrinsic feature of graphene sheets [59]. Intrinsic and extrinsic corrugation of graphene on $SiO_2$ was later examined and confirmed [60]. It was found that graphene is partly bonded with its substrate and to some extent freely suspended on the substrate. Further research is necessary in simultaneously exploring the interfacial contact and energy coupling between graphene and its substrate, and such research has been very rare to date.

### 1.4. Raman Scattering and Thermometry

To measure the temperature and stress of a substrate-particle system, the Raman scattering method is employed. Many researchers selected the Raman scattering method to study the temperature of materials [61-63]. Stokes and anti-Stokes Raman signals are generated during the interaction of the photon and molecules. It is defined as Stokes shift when the emitted photon shifts to a low wavenumber while as anti-Stokes when it has a high shift. Due to the different transition of energy level of molecule, the Stokes signal is much stronger than the anti-Stokes signal. Thus the Stokes signal is often used in the Raman analysis. Stokes Raman signal is strongly dependent on temperature and thermal stress. In Raman thermometry, the temperature of materials can be determined by using the Raman intensity, wavenumber and linewidth (FWHM: full width at half maximum) of the Raman

signals [64]. As the temperature of the material increases, the intensity and wavenumber of the Raman peak decreases [65, 66], and the linewidth of the peak broadens [67]. The peak intensity and wavenumber are of the high sensitivity to the temperature and stress, while the linewidth is of low sensitivity. To define the peak position precisely, a Raman spectrometer with considerably high resolution and a sharp peak are required. The sensitivity of the intensity based approach is much higher than that of wavenumber or linewidth based methods. The shortage of intensity based method is the result is often disturbed by the focal level of lens in the spectrometer. Yue *et al.* discussed how to select these methods based on the intrinsic characteristics of the material [37, 68].

In this work, all the three Raman parameters, *i.e.*, intensity, wavenumber, and linewidth are employed in temperature and stress determination. The sharp Raman peaks of silicon, graphene, and silicon carbide and the small focal spot of the probing laser are important to the success of the Raman measurement. The laser focal level, which is critical to the experimental results, is fixed during the thermal probing experiment in order to obtain high accuracy and precision of Raman signal. Moreover, a new strategy based on Raman intensity is developed for physical analysis. The laser focal level is taken into account, and the effects of temperature, stress, and near-field focusing from Raman mapping are de-conjugated. The temperature rise and stress in the nanoscale heating region are both evaluated.

### 1.5. Scope of Present Work

Understanding the thermal response of a substrate under microparticle or microfiber induced laser focusing is the main purpose of this work. The near-field focusing under self-

assembled particles is investigated in Chapter 2. Chapter 3 explores the nanoscale mapping of self-assembled particles induced thermal, stress, and optical fields by using a single laser for both near-field excitation and Raman probing. A new strategy is developed to de-conjugate the effects of temperature, stress, and near-field focusing from Raman mapping. Thermal probing of a single microparticle and microfiber induced near-field focusing on a substrate with laser light is conducted in Chapter 4, as well as the nanoscale Raman mapping of conjugated optical, thermal, and stress effects. For all the experiments, the effects of particle size and laser energy level on temperature rise in the substrate are examined. The electric field, temperature field, and stress distributions are simulated using the finite element method to compare with and interpret the measurement results. In Chapter 5, the interfacial thermal characterization at CVD graphene-Si, epitaxial graphene-SiC, and CVD graphene-glass interfaces are explored using Raman spectroscopy while the graphene is under a second well-defined laser heating. Phonon coupling and energy exchange capacity at the graphene-substrate interfaces is investigated. Chapter 6 summarizes the conclusions and presents the future work, which is about the characterization of the ripples of graphene and the technique to smooth its wrinkle.

# CHAPTER 2. SUB-WAVELENGTH TEMPERATURE PROBING IN NEAR-FIELD LASER HEATING BY PARTICLES

In this chapter, symmetric experimental and simulation research regarding temperature measurement inside a substrate under micro/nano particles is reported. To determine the temperature, both the wavenumber method and the linewidth method are employed mainly due to the sharp Raman peak of silicon and the small focal spot of probing laser. The relationships between wavenumber and linewidth of silicon and temperature are calibrated first. The thermal response of a silicon substrate beneath silica particles under laser irradiation is measured by using the Raman thermometry for the first time. The electric field distribution and temperature distribution are simulated using the finite element method to compare with and interpret the measurement results.

## 2.1. Experiment Setup and Details

### 2.1.1 Sample preparation

Samples are prepared by laying monolayer silica particles on silicon wafers, where the near-field heating is generated because of the particle-focused laser illumination. A close-packed monolayer can be achieved on silicon, aluminum or glass substrates by using many methods. As is well-known, the production of a latex particle monolayer film is usually achieved by evaporation of particle solutions on a substrate. Iler reported an approach to ordering amorphous monolayers of silica particles with diameters from 15 - 200 nm on a black glass in 1972 [69]. Fischer *et al.* reported a method to form monolayer colloidal particles in 1981 [70]. After that, many researchers showed their interests in this research

topic. Deckman *et al.* developed two different colloidal coating techniques [71]. Dimitrov *et al.* [72], Denkov *et al.* [73], Hulteen *et al.* [74], and Micheletto *et al.* [75] reported their approaches to forming monolayer of nanoparticles. To date, more techniques, such as spin-coating [76-79], dip coating [80, 81], Langmuir-Blodgett deposition [81, 82], wire-wound rod coating [83], and tilting technique [77] have been developed.

In this work, the tilting method is adopted to prepare samples. Surfactant (triton-X: methanol = 1:400 by volume) is mixed with monodisperse silica particle suspensions. The surfactant is used to assist in wetting the surfaces of silicon substrates [76]. The suspensions have silica particles with a solid percentage of 10 % suspended in water. Silica spheres with diameters of 400 nm (Polysciences, Inc), 800 nm, and 1210 nm (Bangs Laboratories, Inc) are used in the experiment without any surface treatment. All these three different particles are prepared on silicon wafers in the same way. The quality of the monolayer films depends strongly on the properties of the substrates, so great efforts are taken in cleaning the substrates. Three pieces of silicon (100) wafers (University Wafer) are cleaned in acetone and then deionized water for one hour with ultrasonic agitation. These wafers are placed on tilted glass slides with an angle of about 10° [77]. The mixture is dispersed onto substrates using syringes and left to dry for about a half hour in the air. The evaporation of mixture started from the top of sample to the bottom until it is completely dry. Two-dimensional monolayer particles are formed on the substrates, and the underlying mechanism is the hydrodynamic pressure due to the water flux from the bulk suspension towards the drying array, and the lateral capillary immersion forces which will attract the particles to each other [84]. Large areas of monolayer particles can be found with a scanning electron microscope

(SEM, FEI Quanta 250). Figure 2.1 shows a typical SEM image of two-dimensional monolayer array of silica particles (800 nm) assembled on a silicon wafer via the tilting technique. As shown in Figure 2.1, some good areas of monolayer particles assembled close together on the sample. There are also some loose areas where particles are separated, and some bilayer or several layers of particles. The excellent packing in good areas can extend over a large area, up to 1 $cm^2$, which is much larger than the laser spot size used in our experiments (8 $\mu m^2$).

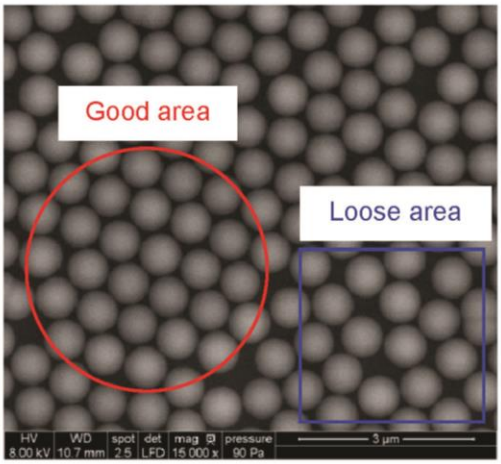


**Figure 2.1 A typical scanning electron microscope image of 2-D monolayer array of silica particles with a diameter of 800nm assembled on a silicon wafer.**

2.1.2 Experimental method for near-field focusing and temperature probing

Figure 2.2 shows schematic of the experimental setup for near-field heating and sub-wavelength temperature measurement. The Raman scattering system consists of a confocal Raman spectrometer (Voyage$^{TM}$, B&W Tek, Inc.) and a microscope (Olympus BX51). Raman spectra are taken at room temperature by using a 532 nm laser line at a power of 4 to 16 mW. The laser beam is focused by a 50× objective lens (LMPLFLN 50×, NA = 0.50). The spot size of the incident light is about 8 $\mu m^2$ on the sample. The sample is placed on a 3-

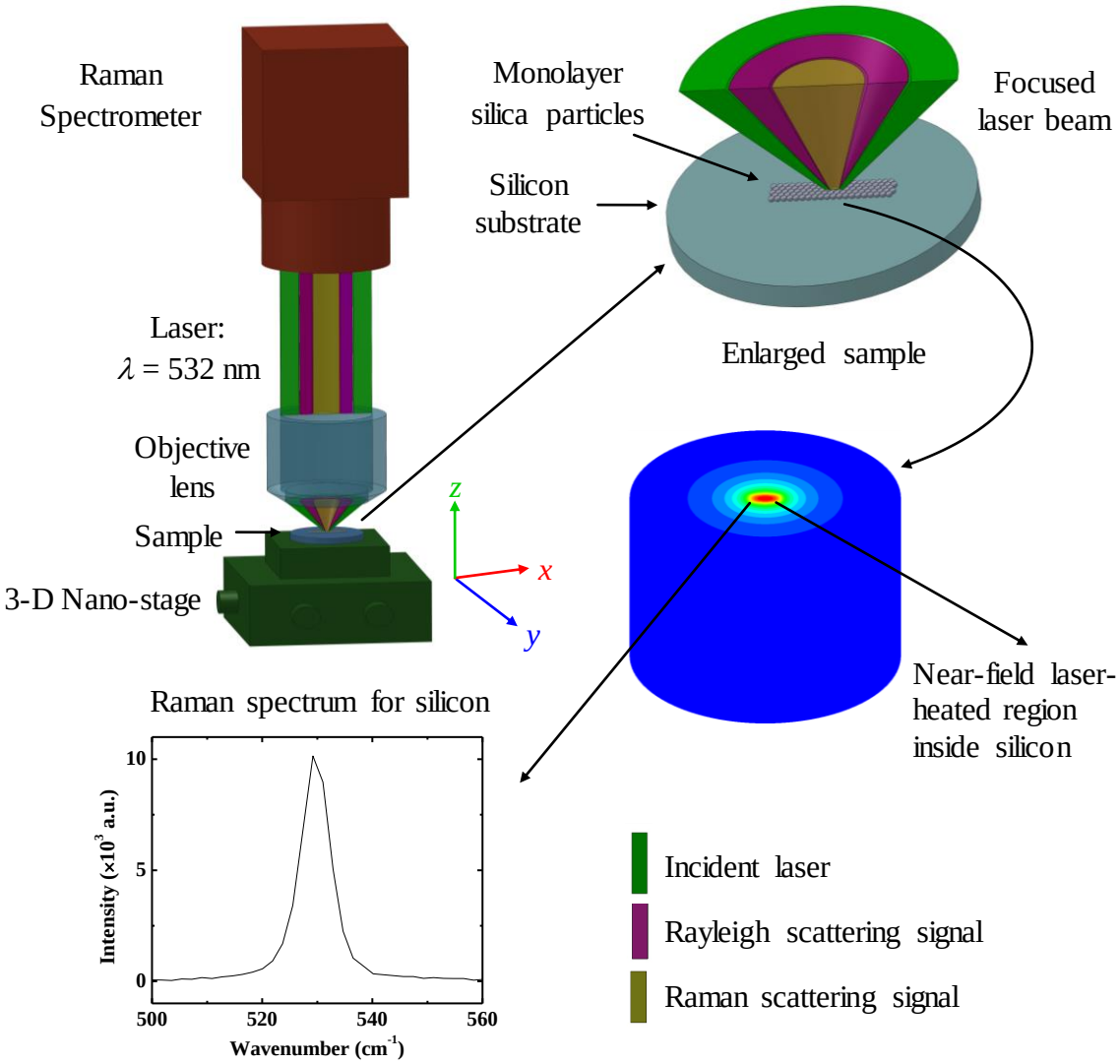


**Figure 2.2 Schematic of the experimental setup for near-field heating and temperature probing (not to scale). A sample that is set on a 3-D piezo-actuated nano-stage is located under the focused laser beam from a Raman spectrometer. The sample is a monolayer of silica particles formed on a silicon substrate. The incident laser, which is used as both temperature probing and heating source, is focused on the substrate by the particles. The spot size of the incident laser is about 2 $\times 4$ $\mu m^2$ in the *x*-*y* plane on the sample. The substrate is heated by the laser in a sub-wavelength region ($r \sim 200$ nm) right beneath the particles. During the experiment, the laser beam is fixed, and the sample moves vertically in the *z* direction controlled by the 3-D nano-stage electrically without any touch of the sample and other equipment. The step of movement is 0.53 μm in a range of about 10 μm, covering the laser focal depth. The temperature rise inside the substrate achieves the highest value at the focal spot.**

D piezo-actuated nano-stage (ThorLabs MAX312). The travel range of the 3-D nano-stage is 20 μm in each direction, with a resolution of 20 nm. The nano-stage is aligned to make sure that the laser is incident vertically from the top of the sample. The incident laser, used as both Raman probing and heating source, is focused by the objective lens on the silica particles at first. Due to the effect of particle, the laser beam is further focused on the silicon substrate and heat up the substrate. The excited Raman scattering signal and Rayleigh scattering signal are collected through the same objective. The whole experimental setup is placed in the air.

The level of temperature rise inside the silicon substrate is affected by factors including the particle diameter, energy flux and focal level of laser. The particle size and laser energy flux can be determined before conducting the experiments. In the experiments, it is critical to pay attention to the laser focal level in order to obtain high accuracy and precision of Raman signal. Figure 2.3 shows how wavenumber, linewidth and intensity for a bare silicon wafer vary with the focal level of the incident laser. Four groups of Raman spectra for bare silicon are obtained at room temperature at different times. The 3-D nano-stage is adjusted along the *z*-axis (vertical direction) to change the position of the sample around the laser focal spot. For each data group, the focal level is adjusted near the focal spot in a range from about -6 to +3 μm, with a step of 0.53 μm. The focusing situation is monitored by using a CCD camera to ensure the reliability and repeatability. Raman spectra are obtained at each focal level, and the background signal is subtracted to obtain sound Raman signal of silicon. Each Raman spectrum is measured 3 times automatically and averaged. The integration time for group 1 & 2 is 4 s, while for group 3 & 4 is 3 s. When moving the sample from below the focal spot to approaching the focal spot, the laser spot size decreases. For group 1 & 2, the linewidth

decreases from about 12.0 $cm^{-1}$ to 6.5 $cm^{-1}$, the wavenumber increases from about 525.8 $cm^{-1}$ to 530.1 $cm^{-1}$, and the Raman intensity increases from about 11,000 to 45,000. For group 3 & 4, the linewidth decreases from about 11.0 $cm^{-1}$ to 6.7 $cm^{-1}$, the wavenumber increases from about 525.9 $cm^{-1}$ to 529.5 $cm^{-1}$, and the Raman intensity increases from about 10,000 to 33,000. Reversely, after the sample moves across the focal spot to an even higher position, the laser spot becomes larger, the Raman intensity and linewidth start to decrease, and the wavenumber shifts to a lower value. The maximums of wavenumber and the minimums of linewidth appear at the same focal level, while the maximums of Raman intensities occur about 0.5 μm ahead. The reason may be due to the beam deflection caused by thermal

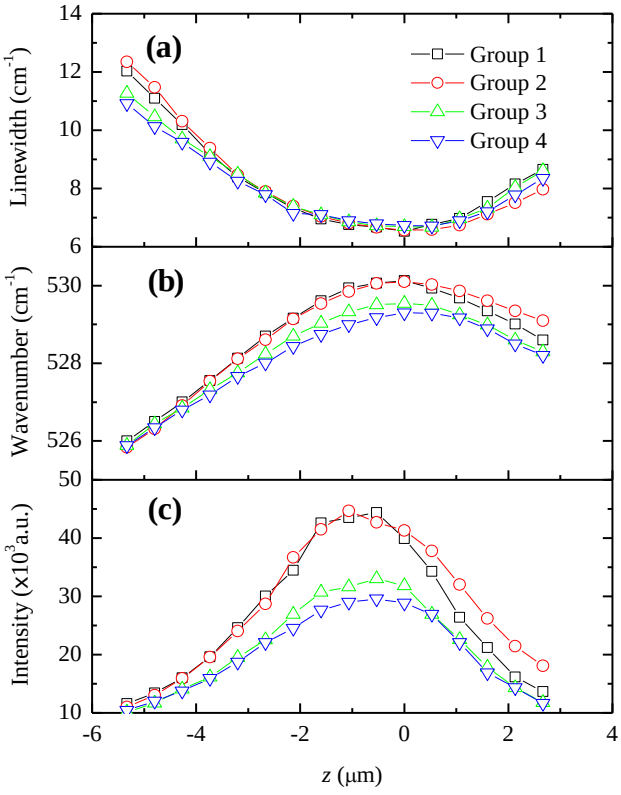


**Figure 2.3 Variations of (a) linewidth, (b) wavenumber, and (c) Raman intensity for bare silicon under laser irradiation along the *z* direction location around the laser focal spot. The laser is incident at room temperature with an energy flux of 8.6 × $10^8$ W/$m^2$.**

expansion. The local silicon is heated by the laser beam and expands. The heated silicon surface is no longer perpendicular to the propagation direction of the laser, which causes beam deflection. The beam deflection influences the Raman intensity. Each group of data indicates that wavenumber, linewidth and intensity are affected by the focal level while other environmental situations are kept the same. So, for each Raman spectrum used later in this work, a group of Raman spectra are obtained respectively. The spectrum with the highest wavenumber and smallest linewidth in each group is selected to represent the result.

The differences among the four data groups in Figure 2.3 indicate a system error. These differences relate to different environmental situations. Change of room temperature, slight shift of objective, and a small change of wavelength of the incident laser, all these environmental factors could lead to a Raman spectrum difference. The maximum system induced error could be about 0.8 $cm^{-1}$ in wavenumber and 0.2 $cm^{-1}$ in LINEWIDTH. In order to determine Raman signal difference between the two situations of bare silicon and silicon with particles, the Raman spectra are obtained under the same environmental experimental situation for both bare silicon and silicon with particles. The following experimental process is employed to eliminate the system error. First, a sample is fixed onto the 3-D nano-stage under a Raman spectrometer and a microscope. The sample consists of a round silicon substrate and some monolayers of silica particles in the center of the substrate. At the edge of sample is bare silicon. A group data of Raman spectra for silicon with silica particles are obtained under laser irradiation. To obtain the Raman spectra of bare silicon under the same environmental situations with that of silicon with particles, the round sample is moved to its margin, where bare silicon is located. The movement is controlled remotely without any

touch of the sample, stage, Raman spectrometer, microscope and other related equipment that would affect the quality of Raman signal. The bare silicon is then adjusted under the laser focal spot, and a group data of Raman spectra for bare silicon are obtained immediately. The integration time and averaged measurement times are the same for both situations. By using this method, the variation in environment and system between bare silicon and silicon with particles is suppressed to a negligible level.

### 2.2. Calibration Result

Raman spectra of silicon for situations of bare silicon substrate and silicon substrate with silica particles are obtained and fitted using Gaussian function. Selected Raman spectra for bare silicon and silicon with silica particles (1210 nm) on the top are shown in Figure 2.4(b). The wavenumber of bare silicon is higher than that of silicon with silica particles. This means the temperature of silicon beneath particles is higher than that of bare silicon. The solid curves are fitted results for the experimental Raman data using Gaussian function. They show good agreement between the experimental data and fitting. In order to determine the thermal response of the silicon substrate under laser irradiation by using Raman thermometry, the relationships between wavenumber and linewidth and temperature for silicon are needed. Researchers have studied the temperature dependences of wavenumber [37, 39, 61, 63, 64, 85-88] and linewidth [39, 61, 62, 64, 89, 90] for silicon. Balkanski *et al.* presented two theoretical models of the wavenumber and linewidth changing with temperature from 5 to 1400 K, and indicated that the relationships were both linear at low temperatures [61]. The linear fitting slope of wavenumber against temperature reported in literatures varies from

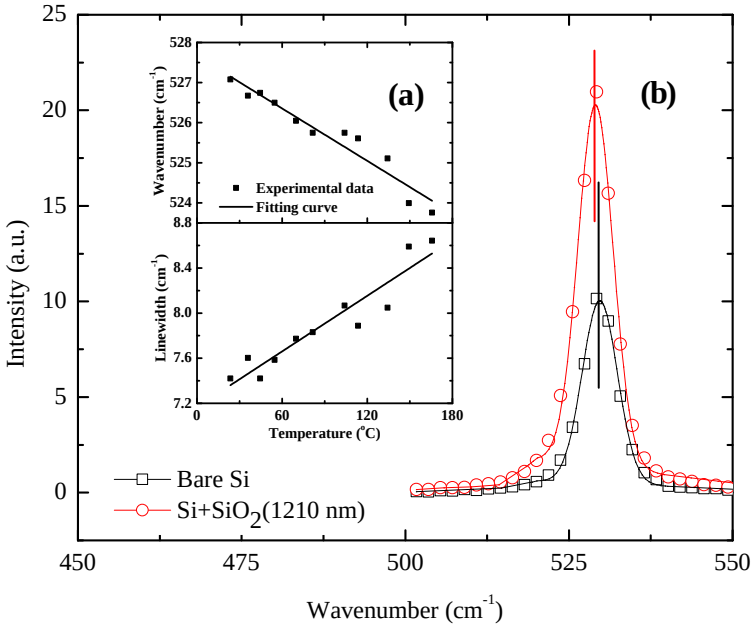


**Figure 2.4 Calibration for wavenumber and linewidth of silicon against temperature. (a) The slope of the linear fitting for wavenumber against temperature is -0.022 $cm^{-1}$/K. For linewidth against temperature, it is 0.0082 $cm^{-1}$/K. (b) A comparison of Raman spectra between bare silicon and silicon under silica particles. The diameter of silica particle is 1210 nm. The solid curves are the Gaussian fittings for the experimental Raman data. The difference of the two straight lines shows that the Raman peak shifts due to temperature rise in near-field heating.**

-0.02 to -0.03 $cm^{-1}$/K within temperatures of 300 - 600 K [39, 61, 64, 88, 91, 92]. The slope of the linear fit for the linewidth and temperature is 0.01 $cm^{-1}$/K [40]. In this work, the calibrations for wavenumber and linewidth of silicon against temperature are conducted before the sub-wavelength thermal sensing experiment. The sample, a silicon wafer, is cleaned in acetone for about one hour. A round electric heater with a controlled power is used to heat the silicon sample from room temperature to 160 °C, with an increasing step of 10 °C. A T-type thermocouple is attached on the sample near the laser spot to measure the temperature. The incident laser energy flux is $8.6 \times 10^8$ $W/m^2$. The integration time is 1 second and two rounds of measurements are averaged for each Raman spectrum. Each temperature point is measured three times and their average value is adopted. As shown in

Figure 2.4(a), the slope of the linear fitting for the wavenumber and temperature is -0.022 $cm^{-1}/K$ and the slope for the linewidth *vs.* temperature is 0.0082 $cm^{-1}/K$ in a temperature range from 20 - 160 °C, which agree well with the literature values.

### 2.3. Thermal Probing of Silicon under Silica Particles

In the experiments, the focal level, particle size and laser energy are important factors for determining the near-field heating. The spot size of the laser is about $2 \times 4\ \mu m^2$, which is determined using a blade method. The laser spot widths covering 90 % of the laser energy are chosen to represent the spot size. The diameters of particles are 0.4, 0.8, and 1.21 μm, respectively. Silicon substrates with these three silica particles on the top are used in the experiments to study the effect of particle size on sub-wavelength heating. In order to investigate the near-field heating effect caused by laser irradiation, Raman scattering is performed with four laser powers of 2.0, 3.0, 5.5 and 6.9 mW, corresponding to energy fluxes of $2.5\times10^8$, $3.8\times10^8$, $6.9\times10^8$ and $8.6\times10^8$ $W/m^2$, respectively.

During the experiments, the group for silica particles with diameter of 1210 nm under laser energy flux of $8.6\times10^8$ $W/m^2$ is first conducted. To assure accuracy, the experimental methods explained in Section 2.2 are employed. Two groups of Raman spectra for bare silicon and silicon with 1210 nm diameter silica particles on the top are obtained, with integration time of 1 s. The Raman linewidth, wavenumber and intensity follow the trends shown in Figure 2.3. The linewidth for bare silicon and silicon with particles are 6.31 $cm^{-1}$ and 6.77 $cm^{-1}$, respectively. It indicates a temperature rise of 55.8 K based on the broadening

of linewidth (0.46 $cm^{-1}$). The wavenumber shifts for bare silicon and silicon with particles are 529.70 $cm^{-1}$ and 529.06 $cm^{-1}$, respectively. Based on the wavenumber method, the wavenumber difference (0.64 $cm^{-1}$) between the two values gives a temperature rise of 29.3 K. As shown in Figure 2.5, the temperature rises assessed based on the wavenumber are lower than those based on the linewidth method. The differences between the two methods are mainly due to the temperature gradient and compressive stress around the laser-heated spot [39, 40, 92]. As the temperature increases, the number of phonons rises and the lifetime decreases. The increase of linewidth indicates the temperature rise inside silicon, as linewidth is little influenced by thermal stress. The wavenumber is affected by both temperature difference and thermal stress. The laser beam heats up the sample within an extremely focusing area. The heated area tends to expand and raise pressure to the nearby

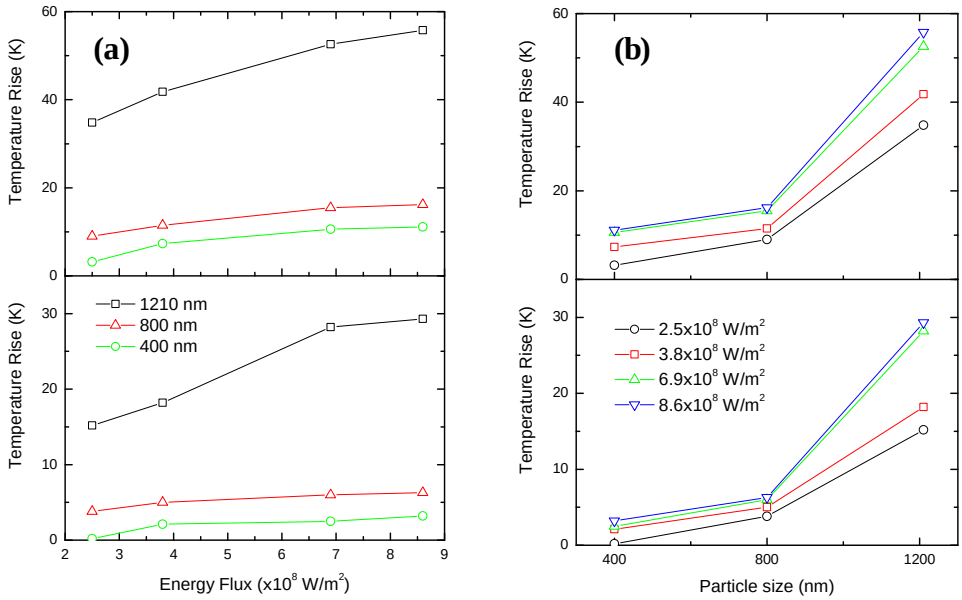


**Figure 2.5 The relationship between temperature rise in silicon against (a) energy flux of incident laser and (b) diameter of silica particle. The upper figures show the temperature rise assessed based on the linewidth, and the lower figures are based on the wavenumber method.**

cold silicon substrate. The local pressure causes a distortion of the crystal lattice and the equilibrium positions of the atoms are changed, which causes lattice variation. An additional shift is added in wavenumber due to the stress besides temperature rise. The stress effect induced by particle-focused laser heating drags the Raman peak to the higher wavenumber (lower temperature) direction. Therefore, the temperature rise obtained based on the wavenumber method is lower than that based on the linewidth method. The combined use of these two methods gives comprehensive understanding of how high the sample can be heated up and whether there exists any thermal stress.

The same experimental method is employed to measure the temperature rise for the situation of silica particles with 1210 nm diameter under three other laser energy fluxes of $2.5\times10^{8}$, $3.8\times10^{8}$, and $6.9\times10^{8}$ W/m$^2$. All the experimental procedures for silica particles with 800 and 400 nm diameters under four different laser energy fluxes are the same with that of 1210 nm particles. Figure 2.5(a) shows how the temperature rise changes against the laser energy. Based on the linewidth broadening, the temperature rise increases almost linearly from 34.8 to 55.8 K, as the laser energy flux increases from $2.5 \times 10^{8}$ to $8.6\times 10^{8}$ W/m$^2$. While for silica particles of 800 nm, the temperature rise increases from 9.0 to 16.2 K, and for silica particles of 400 nm, it increases from 3.2 to 11.1 K. As expected, when the energy flux of the incident laser increases, more energy will be focused on silicon and absorbed. As a result, the temperature inside the silicon increases more. Figure 2.5(b) shows the relationship between temperature rise of silicon and silica particle size. With the increase of particle size, the incident laser is more focused on the silicon substrate, and the temperature rise is higher. Under energy flux of $8.6\times10^{8}$ W/m$^2$, the temperature rise is 11.1

K for silica particles of 400 nm diameter, 16.2 K for those of 800 nm, and 55.8 K for those of 1210 nm, according to the linewidth method. As the particle size increases from 400 to 800 nm, the temperature rise increases by about 45%. When the particle size increases to 1210 nm, the temperature rise goes up to 5 times that for 400 nm particles. Similar trends for temperature rise can be found in the results for other laser energy fluxes. All the curves conclude that the temperature rise increases exponentially with silica particle diameter in the range from 400 to 1210 nm.

## 2.4. Physics behind Experimental Observation

### 2.4.1. Electrical field distribution inside particle and substrate

In order to explore the mechanism of the temperature rise in the silicon substrate under silica particles, numerical simulation of the electric field enhancement is conducted with the finite element method (FEM) [30, 59]. The modeling is performed by using HFSS V13 (ANSYS, Inc.), a full-wave high-frequency 3D finite element modeler of Maxwell's equations. Due to the different sizes of silica particles, different models are employed in the simulation. For the particle of 400 nm diameter, as the laser spot size is about $2\times4\ \mu m^2$, a total of 45 particles are considered to be covered under the laser spot. The whole computational domain consists of 45 silica particles on a silicon substrate in the air. For consideration of computational cost and mesh density for HFSS, the domain is set symmetrical in both electric and magnetic directions. Thus, a reduced domain is needed in the simulation. Maxwell's equations are solved across a reduced rectangular computational domain with dimensions of 400 nm $\times$ 348 nm $\times$ 2800 nm: containing a half and two quarters of silica particles, a silicon substrate under the particles, and the air around the particles. A

plane wave with a wavelength of $\lambda = 532$ nm is incident normally from the top of the domain. Perfect *E* and perfect *H* symmetry boundaries are adopted at the symmetrical planes perpendicular and parallel to the electric field direction, respectively. Absorbing (radiation) boundaries are applied for the other boundary planes in the domain. The distance from the absorbing boundary to the nearest particle is set to 400 nm, which is much greater than $\lambda/4$ (= 133 nm). The application of absorbing boundary in the simulation is satisfied. The whole domain is divided into tetrahedral grids with a maximum length of 58 nm, which is less than $\lambda/4$. The electric field amplitude of the incident wave is set to 1 V/m. Therefore, the near-field enhancement value, the ratio of scattered to incident electric field amplitude, is the same as the electric field amplitude of the scattered light.

At an incident wavelength of 532 nm, the dielectric permittivities of silica and silicon are $\varepsilon = 2.13 + 0i$ and $\varepsilon = 17.22 + 0.428i$, respectively [93]. The electric conductivities of silica and silicon are 0 and $1.34 \times 10^5$ S/m, respectively. The simulation is performed on a platform consisting of a 3.72 GHz AMD $\times 6$ processor and 16 GB RAM. The computational results converge and a total of 13 passes are finished for the 400 nm-particle case. A similar size-reduced computational domain is also adopted to calculate the electric field distribution for the 800 nm-particle case. About 15 particles of 800 nm diameter are considered to be covered under the laser beam. The reduced computational domain for 800 nm-particle case is set at 800 nm × 696 nm × 3200 nm, which is much larger than that for 400 nm. The completed total number of computational passes is reduced to 10 and the maximum grid length in the particle and substrate is 82 nm. As the silica particle of 1210 nm diameter is very large, the

laser beam can only cover about 6 - 7 particles. We need to reduce the amount of calculation to improve the quantity of mesh in modeling. The reduced domain used for the 1210 nm particle case is simpler than those for 400 and 800 nm. In the computation, only one silica particle of 1210 nm on a silicon substrate is considered. Perfect *E* and perfect *H* symmetry boundaries are also applied in the domain. Thus, only a quarter of silica particle is computed, which reduces the amount of computation a lot. The reduced domain is set at 605 nm $\times$ 605 nm $\times$3810 nm. Absorbing (radiation) boundaries are applied for the other boundary planes. The distance from the absorbing boundary to the nearest particle is 600 nm, greater than $\lambda/4$. The completed total number of computational passes is reduced to 4. The maximum grid length in the particle and substrate is 95 nm, still less than $\lambda/4$.

Figure 2.6 shows the electric field distributions inside a particle and the substrate beneath the particle for all the three particle diameters. Symmetric electric field distributions are observed. The electric field is enhanced mainly inside and under the particles in varying degrees for different diameters. In Figure 2.6(a), for the 400 nm-particle case, the strongest electric field is 1.6 V/m inside the silica particle. The electric fields are enhanced both in the upper and lower parts of the particle. Inside the silicon substrate, the strongest electric field is about 0.5 V/m, which appears mostly right beneath the particle. The shape of the electric field enhancements on the top of the substrate is elliptical, with an about 200 nm diameter in the magnetic field direction (*r* direction) and a 150 nm diameter in electric field direction. The length of enhanced electromagnetic field along the magnetic field direction is longer than that along the electric direction. At skin depth, the electric field amplitude drops to $e^{-1}$ of that on the surface. The laser energy is mostly absorbed within a small elliptical cone with a

skin depth of about 878 nm near the surface of silicon under the particle, and attenuates from the surface to the inside. Observed from Figure 2.6(b), for the 800 nm-particle case, the strongest electric field enhancements factor is about 3.1 inside the silica particle, which is twice of that for the 400 nm-particle case. The electric fields are enhanced both in the upper and lower parts of the particle, but more in the lower part, near the contacting point between the particle and substrate. The center of the electric field enhancement in the particle moves downwards towards the substrate when the particle size increases. The strongest electric field is 1.2 V/m on the top of the silicon substrate, and it forms an ellipse shape with a 220 nm diameter in the magnetic field direction and 180 nm in the electric field direction. The electric field impinges into the substrate with a skin depth of about 1094 nm.

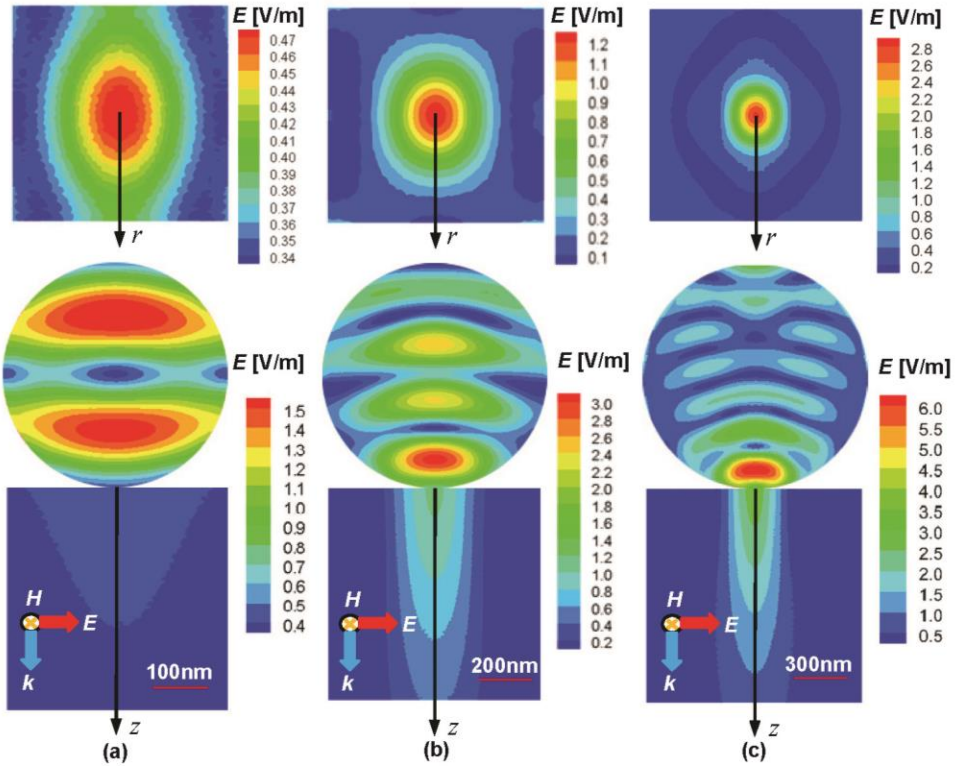


**Figure 2.6 Electric field distribution inside the substrates and particles of (a) 400, (b) 800 and (c) 1210 nm diameter. In figures (a), (b) and (c), the upper figures are top view of the substrates beneath the particles, and the lower figures are central cross-section view of the particles and substrates. The amplitude is equal to the enhancement factor.**

It is noticed from Figure 2.6(c) that, for the 1210 nm-particle case, the strongest electric field inside the silica particle is 6.4 V/m. The electric field is enhanced mostly in the lower part of the particle, close to the contacting point between particle and substrate. The center of the electric field enhancement inside the particle is about 100 nm away from the contacting point. It moves towards the substrate when the particle size increases from 400 to 1210 nm. While inside the silicon substrate, the value of the strongest electric field enhancements is 2.8, due to high absorption of laser for silicon. Most of the laser energy is absorbed inside the silicon substrate normally beneath the particle. The strongest enhanced area on the top of the substrate is about $180 \times 150$ nm$^2$. The skin depth inside the substrate is about 1013 nm. As shown in Figure 2.7(a), the electric field intensity is the highest in the center of the region and attenuates along the surface of silicon. As a laser beam propagates, the intensity of the optical field decays with the square of the electric field. The laser focal spot sizes under each particle, *i.e.* the distances for the optical intensity to decay by a factor of $e^{-1}$ along the radial direction of the particle, are about 200, 150 and 130 nm for the 400, 800 and 1210 nm-particle cases, respectively. The regions within the focal spot sizes are the main source of the Raman signal, which basically represent the probing resolution of temperature. The skin depth for electric field is $\delta = \lambda / (2\pi\kappa)$, where $\kappa$ is the extinction coefficient. At $\lambda = 532$ nm, $\kappa = 0.0516$ for silicon, and the theoretical skin depth is $\delta = 1.64$ μm. In Figure 2.7(b), the skin depths in silicon are 878, 1094 and 1013 nm for the 400, 800 and 1210 nm-particle cases, respectively. They are a little smaller than the theoretical value since the particle-focused light is not incident normally to the silicon surface. Considering the optical field, the skin depths are 513, 620 and 584 nm for the 400, 800 and 1210 nm-particle cases, respectively.

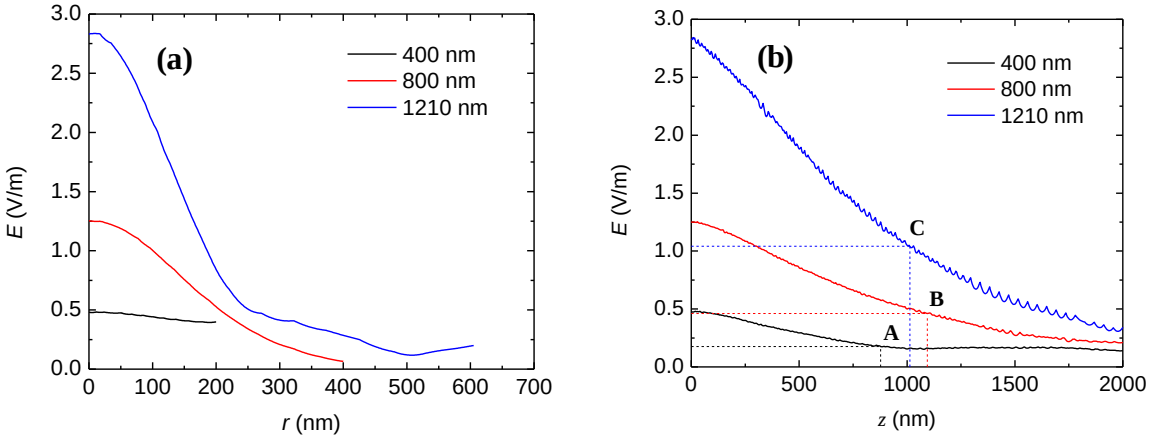


**Figure 2.7 Electric field profile inside the substrates. (a) Electric field inside silicon in the *r* direction (along the magnetic field direction). (b) Electric field inside silicon in the *z* direction. At points A, B and C, the amplitude of electric field drops to $e^{-1}$. The *z*-axis values of A, B and C are 878, 1094 and 1013 nm, respectively.**

2.4.2. Temperature distribution inside silicon substrate

The temperature distribution inside the silicon substrate can be simulated using ANSYS FLUENT (V12, Ansys, Inc) with the knowledge of the electric field distribution. As the temperature distribution inside the substrate is symmetric, a quarter-cylinder computational domain with a radius of 15 μm and a height of 20 μm is employed in the simulation. The thermal conductivity of silicon is 148 W $m^{-1}$ $K^{-1}$ at 300 K. The heat transferred through the surrounding air by convection and heat transferred by radiation to the environment can be neglected for the high thermal conductivity of silicon. So it is reasonable to set the top end surface of silicon as adiabatic. Both vertical cross-sections use symmetric boundary conditions. The peripheral and foot end surfaces of the domain are set to 300 K. The initial temperature of the substrate is 300 K. The heat source is distributed in the center of the cylinder within a small volume of less than $0.5 \times 0.7 \times 2.0$ $\mu m^3$ following the laser illumination situation calculated by HFSS. The numbers of particles considered to be covered

under the laser spot are 45, 15 and 7 for the 400, 800 and 1210 nm-particle cases, respectively. The heat generation rate per unit volume can be calculated from $\dot{q} = I\beta$, where $I$ is the laser intensity inside the silicon substrate, $\beta = 4\pi\kappa/\lambda$ is the absorption coefficient, $\kappa$ is the extinction coefficient, and $\lambda$ the wavelength of incident laser in free space. The laser intensity inside the substrate equals the Poynting vector, $I = P = 0.5c\varepsilon_0 nE^2$ . Here $c = 3\times10^8$ m/s is the light speed in free space, $\varepsilon_0 = 8.854\times10^{-12}$ F/m is the vacuum permittivity, $n = 4.15$ is the refractive index of silicon, and $E$ (V/m) the time-average intensity of the electric field, which is calculated using HFSS.

As the temperature rise inside the substrate increases nearly linearly with the incident laser energy, for all the four energy flux cases used in our experiments, we only study the cases with the maximum energy flux, $5.6\times10^8$ W/m$^2$. Other cases with different energy fluxes can be scaled proportionally. The steady state temperature distributions inside the silicon substrates are shown in Figure 2.8. Symmetric temperature field distributions are observed in Figure 2.8(a) to Figure 2.8(c). The heat conduction in the silicon substrate is very quick due to its high thermal conductivity. From Figure 2.8(d) we can see that the highest temperature rises are located under the center of particles. In Figure 2.8(e), the calculated maximum temperature rises inside the silicon are 2.8, 4.0 and 9.0 K for 400, 800 and 1210 nm-particle cases, respectively.

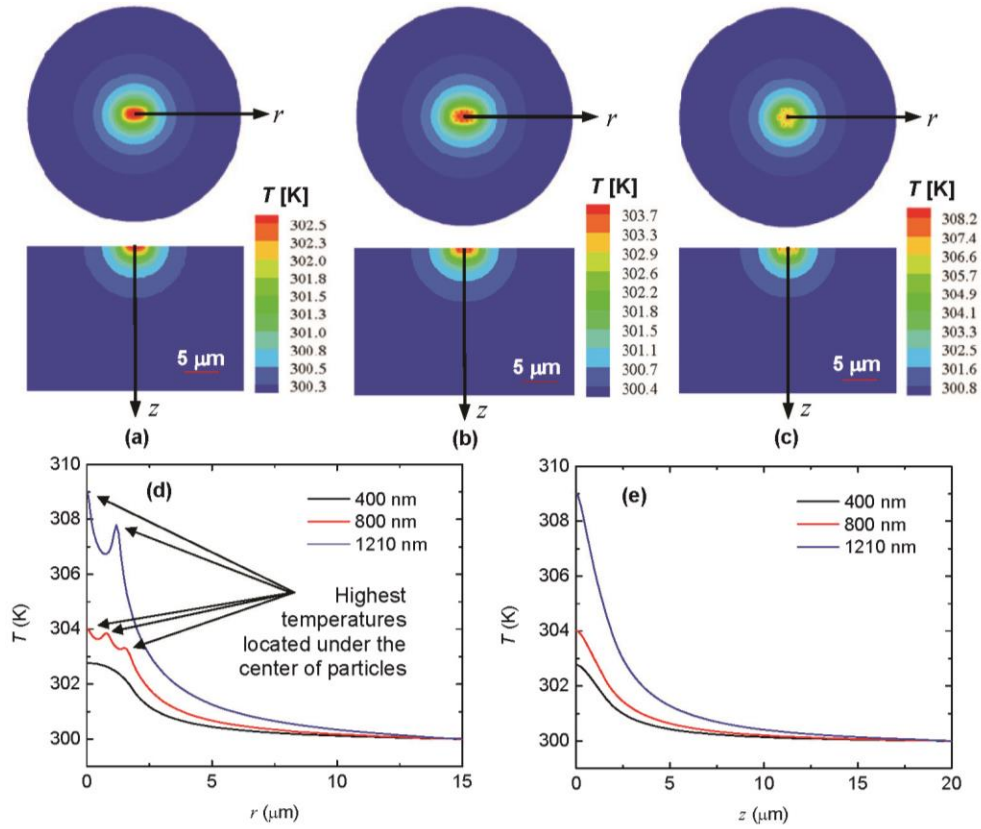


**Figure 2.8 Temperature distributions inside silicon substrates under particles of (a) 400, (b) 800 and (c) 1210 nm diameter. In figures (a), (b) and (c), the upper figures are top view of the substrates beneath the particles, and the lower figures are central cross-section view of the substrates. (d) Temperature profile inside silicon in the radial direction. (e) Temperature profile inside silicon in the vertical direction. The initial temperature of the substrates is 300 K.**

The calculated values are smaller than the results based on the wavenumber method, and are even much smaller than linewidth temperature values. From Figure 2.4(a) we know that the linewidth method has lower temperature sensitivity than the wavenumber method. In addition, while fitting Raman spectra using the Gaussian function, the effect of the subtracted baseline on linewidth is more than that on the wavenumber shift. However, the linewidth temperatures are closer to reality as they are less affected by the thermal stress. Both the calculated and measured temperature rises increase exponentially with the increase of the

particle size. The difference between them could be due to three main factors. First, the incident laser employed in the electric field simulation is a uniform plane wave, while in the experiments the laser is focused by a $50\times$ objective lens before it irradiates the sample. The focal length is about 25 mm, and the angle of incidence is about $20^\circ$. More laser energy should be focused on the particle-substrate sample due to the already focused light. Second, during the simulation of electromagnetic field by HFSS, the dimensions of the computational domain increase as the diameter of particle increases. As a result, the mesh density drops and the length of the mesh grids increases. Due to the drop of the mesh quality, the precision of the computational results for bigger particles is less accurate than that for smaller particles. So, the difference between the computational and experimental results for bigger particles is larger than those for smaller particles. Therefore, the temperature acquired in the model is underestimated to some extent. Third, a part of the Raman signal came from the silicon wafer from the spacing among particles. As the laser beam was pre-focused on the particles by the objective lens, the focal level for the silicon beneath the particles was at a higher position than the focal spot. From Figure 2.3 we know that the wavenumber of the silicon shifted to a lower value, and the linewidth broadened. As a result, the obtained experimental temperatures are higher. However, as the spacing among particles only accounted for about 10 % of the total area, and the laser was not directly focused on the silicon, which leads to a low Raman intensity, so the contribution from this part of silicon to the total Raman signal was not significant.

# CHAPTER 3. NANOSCALE PROBING OF THERMAL, STRESS, AND OPTICAL FIELDS UNDER NEAR-FIELD LASER HEATING

In this chapter, far-field nanoscale mapping of conjugated thermal, stress, and near-field focusing effects in a silicon substrate beneath silica particles under laser irradiation is conducted for the first time using Raman spectroscopy at a 20 nm lateral resolution ($< \lambda/26$). Methodologies are developed to separate the optical, thermal, and stress effects and evaluate the temperature rise and local stress in particle-induced near-field focusing. The electromagnetic and temperature fields inside the substrate-particle system are simulated to interpret the measurement results.

## 3.1. Experiment Setup and Details

### 3.1.1 Sample preparation

Silica particles are patterned on silicon wafers in a monolayer using a tilting technique [77]. Surfactant (triton-X: methanol = 1:400 by volume) is mixed with monodisperse silica particle suspensions [94]. The suspensions have silica particles with a solid percentage of 10 % suspended in water. As-received silica spheres of 200 nm (Corpuscular), 400 nm (Polysciences), 800 nm, and 1210 nm (Bangs Laboratories) diameters are used without any surface treatment. Silicon (100) wafers (University Wafer) are cleaned in acetone and then deionized water for an hour with ultrasonic agitation. These wafers are placed on glass slides, which are tilted on a table with an angle of about 10 ° [77]. The mixture is dispensed onto substrates using a syringe and left to dry for about a half hour in the air. Then a 2-D monolayer of particles is formed on the substrate. Large areas of monolayer particles can be

identified under scanning electron microscope (SEM). Figure 3.1 shows typical SEM images of silica monolayer of 1210 nm diameter assembled on silicon wafers. The compact assembled area can extend over a large area, up to 1 $mm^2$, which is much larger than the laser spot area used in our experiments (~0.5 $\mu m^2$). The average diameter of the particles shown in Figure 3.1(b) is about 1120 nm, a little smaller than the nominal diameter reported by the company.

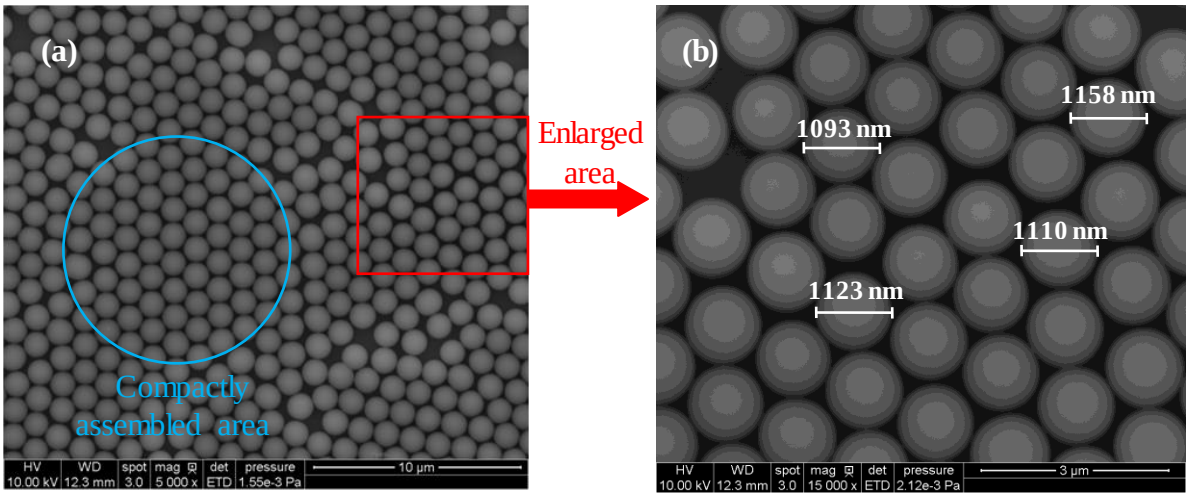


**Figure 3.1 SEM images of 2-D monolayer array of silica particles assembled on a silicon wafer. The average diameter of the particles is about 1120 nm.**

3.1.2 Nanoscale Mapping

Figure 3.2 shows schematic of the experimental setup for the nanoscale structural imaging. The Raman scattering system consists of a confocal Raman spectrometer (Voyage$^{TM}$, B&W Tek) and a microscope (Olympus BX51). Raman spectra are taken at room temperature by using a 532 nm laser line at variable power from 1.2 - 4.7 mW. The laser beam is focused by a 100× objective lens (NA = 0.80). The movements of the sample are controlled by a piezo-actuated nano-stage (ThorLabs NFL5DP20) in the *x* direction (imaging direction) and a motorized translation stage (ThorLabs MT1-Z8) in the *z* direction.

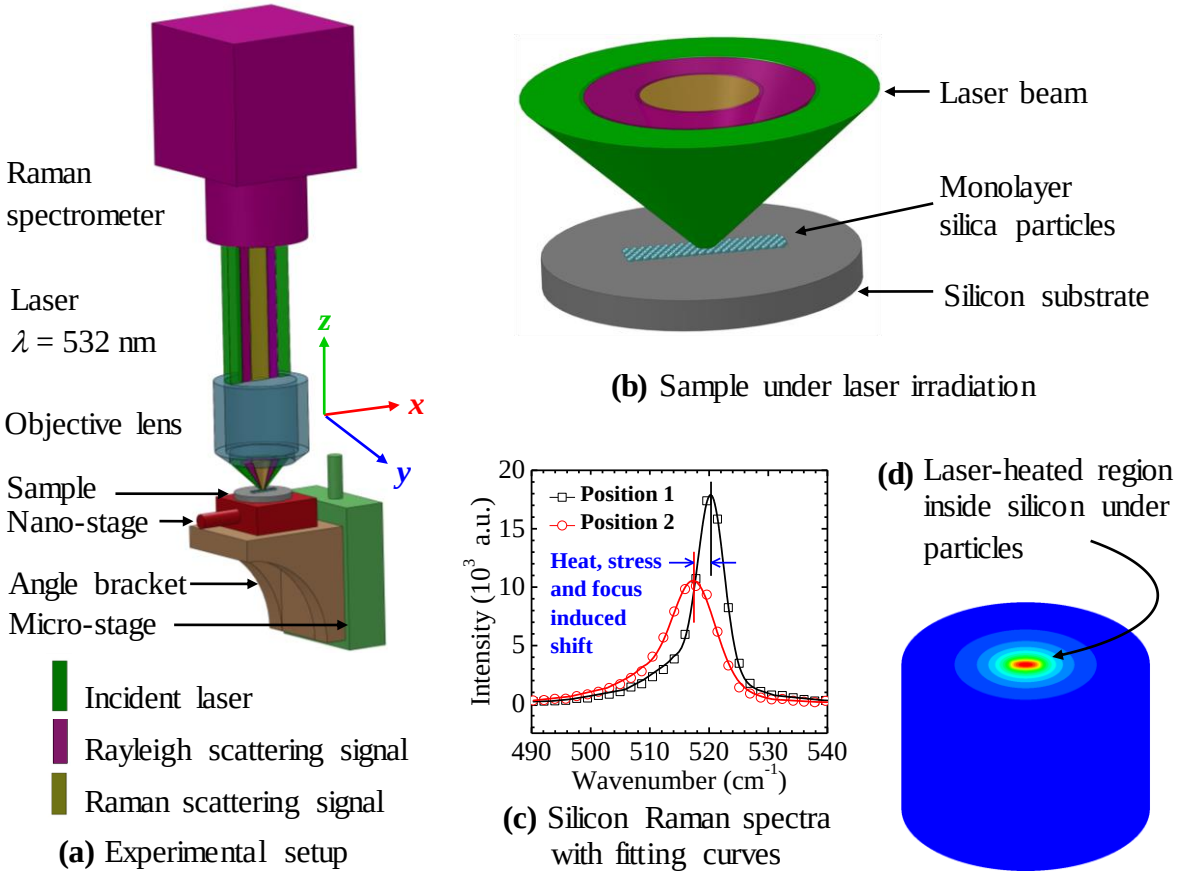


**Figure 3.2 Schematic of experimental setup for far-field nanoscale imaging (not to scale). (a) A sample is located under an objective-focused laser beam from a Raman spectrometer. The movement of sample in the *x* direction is controlled by a piezo-actuated nano-stage. The focal level of the laser on the sample in the *z* direction is controlled by a motorized micro-stage. (b) The sample consists of a silicon substrate and a monolayer of silica particles. The spot size of the incident laser is about 0.5 μm2 in the *x*-*y* plane on a silicon substrate. (c) The Raman spectrum shifts to left due to the near-field laser heating, stress, and the out-of-focus effect. (d) The silicon substrate is heated in a sub-wavelength region (r ~ 200 nm) right beneath the particles.**

These two stages are vertically assembled together. The piezo-actuated range of the nano-stage is 20 μm with a resolution of 20 nm. The sample position in the *z* direction is adjusted by the motorized stage to change the focal level of the incident laser within a range of 12 mm and a location accuracy of ±0.1 μm. The incident laser used as both Raman probing and heating source is focused on the silica particles by the objective lens. Due to the effect of

particles, the laser beam is further focused on the silicon substrate under the particles and heats up the substrate. The excited Raman scattering signals and Rayleigh scattering signals are collected by using the same objective. Raman spectra of silicon substrate with silica particles on the top at different positions in the *x* direction are obtained and fitted using the Gaussian functions.

The near-field heating and thermal stress inside the silicon substrate is affected by factors including the particle diameter, energy flux and focal level of the laser. The particle diameter and laser energy flux can be determined precisely before the experiments. In the experiments, it is critical to pay attention to the laser focal level in order to obtain high accuracy and repeatability of Raman signals. The position of the sample is adjusted near the focal plane within a distance of about 6 μm. Raman spectra are obtained at each level and the background noise is subtracted to obtain sound Raman signal. Wavenumber, linewidth and intensity are affected by the focal level when other environmental factors are fixed. Wavenumber and intensity decrease, and linewidth broadens when the sample moves away from the focal plane in the *z* direction [95].

A group of Raman spectra are obtained in the *z* direction before imaging in order to determine the focal level. The focal level is selected with the highest Raman intensity in the group. The sample is then fixed to the focal level without vertical shift. Environmental factors such as the change of room temperature and movement of the objective would lead to a Raman spectrum difference. Therefore, the imaging process is followed immediately to minimize the effect of environmental factors. The sample is scanned along the *x* direction in

a maximum range of 4.0 μm with a step of 27 or 53 nm, as shown in Figure 3.3. The movement is controlled electrically without any touch of the sample, stage, Raman spectrometer, microscope and other related equipment that would affect the quality of Raman signal. The Raman spectra change with the nanoscale movement of the sample is finally obtained. The highest energy flux is first used in the experiment, following by 79 %, 50 %, and 25 % of the maximum energy.

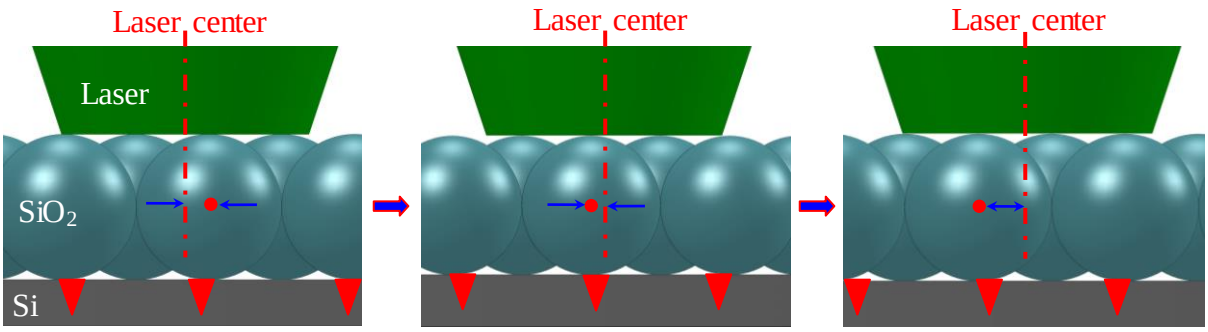


**Figure 3.3 Movements of sample relative to the incident laser in the *x* direction. During the experiment, the position of the laser beam is fixed, and the sample moves along the *x* direction controlled by the nano-stage electrically without any touch of the sample and other equipment.**

3.1.3 De-Conjugation of Thermal, Stress, and Optical Fields

In order to investigate the temperature rise and thermal stress caused by particle near-field focusing, experiments on silicon with particles on the surface and bare silicon are both conducted. The incident laser is first focused on the particles of the sample. The Raman spectra for silicon under monolayer silica particles are taken under four energy fluxes. Bare silicon is located around the particles in the margin of the sample. Without any movement of Raman spectrometer, the margin of the sample is moved to the laser center to obtain the Raman spectra for bare silicon. The laser is then adjusted to focus on the silicon and four energy fluxes are used as well. The integration time and measurement average are the same

for those for silicon with particles. A group data of Raman spectra at different focal levels around the focal plane are obtained for each case. The Raman spectrum with the highest intensity is selected to represent each result. By using this method, the differences between the environmental situations for both bare silicon and silicon with particles are suppressed to the minimal level.

## 3.2. Result and Discussion

### 3.2.1 Nanoscale mapping for near-field heating under 1210 nm particles

Four laser energy percentages of 25 %, 50 %, 79 %, and 100 % are used in our experiments, with the highest energy flux of $3.9 \times 10^9$ W/m$^2$. The Raman intensity increases with the energy flux. The highest Raman intensities ($I_{max}$) are $1.30 \times 10^4$, $2.08 \times 10^4$, $3.83 \times 10^4$ and $4.67 \times 10^4$ for energy percentages of 25 %, 50 %, 79 %, and 100 %, respectively. As the variation trends of the structure are the same for different energy fluxes, here we only analyze the case for $3.1 \times 10^9$ W/m$^2$, of which the energy percentage is 79 %. Other cases can be treated similarly. The Raman intensity $I$, wavenumber $\omega$ and linewidth $\Gamma$ of silicon vary periodically along the $x$ direction and are shown in Figure 3.4. About three periods are observed within the travel range in the figure. The period length decreases from the left to the right. The difference may due to the diameter difference, the interspace among particles, and the backlash of the stage while moving. For the first 3/4 period, half of the period length is 906 nm, much longer than the average particle radius (560 nm). For the second and third period, the period lengths are 1226 and 1013 nm, respectively, close to the average particle diameter (1120 nm). In the second period, the intensity difference between $I_{max}$ and $I_{min}$ is $2.37 \times 10^4$, with a maximum intensity ratio ($I_{max}/I_{min}$) of 2.58. As shown in the inset of

Figure 3.4(a)], within a distance of 20 nm in the sample moving direction, there is a Raman intensity difference of about 3000, and the intensity ratio within this distance is 1.12. The difference can be distinguished at this scale in our experiment. As the intensity is the raw datum without any further processing, it is the best quality to specify the imaging resolution. It is conclusive that the imaging resolution based on the Raman intensity difference can be down to 20 nm, although the step length in the experiments is 53 nm.

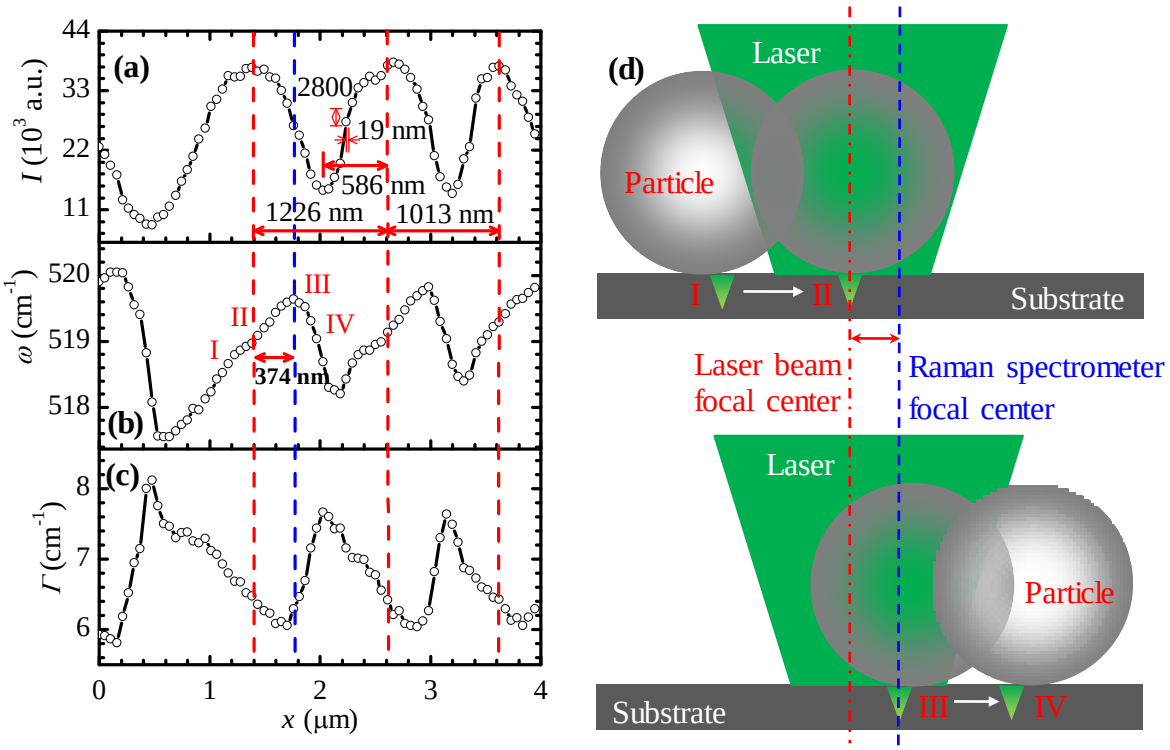


**Figure 3.4 Nanoscale mapping for near-field heating under 1210 nm particles. The *x* direction variation of (a) Raman intensity *I*, (b) wavenumber $\omega$, and (c) linewidth $\Gamma$ for silicon under particles of 1210 nm diameter with laser irradiation. (d) The relative position of a silica particle and the laser beam to explain the observed Raman variation in space.**

In the period, $\omega$ changes in a range from 518.2 - 519.6 cm$^{-1}$, with a maximum shift of 1.4 cm$^{-1}$. At position II in Figure 3.4(b), $\omega$ is about 519.0 cm$^{-1}$, where $I_{max}$ is located. $\omega$ increases to the maximum at position III with a distance of 374 nm, then decreases to the minimum

within 426 nm, and finally rises to 519.0 $cm^{-1}$ again. $\Gamma$ changes from 6.0 to 7.7 $cm^{-1}$, with a maximum difference of 1.7 $cm^{-1}$. The variation of $\Gamma$ is contrary to that of $\omega$. It first decreases from 6.4 to 6.0 $cm^{-1}$, then increases to 7.7 $cm^{-1}$, and finally decreases to 6.4 $cm^{-1}$ again. The total increasing and total decreasing distances are not equal in a period for both $\omega$ and $\Gamma$, separately. There are three main reasons that can account for the difference. First, the focal spot of the excitation laser and the focal spot of the Raman spectrometer are off a little (not exactly confocal). The transverse distances between the most excited Raman signal point and the Raman spectrometer center are shown in Figure 3.4(d). The Raman signal point is the same as the laser focusing point, while the Raman spectrometer center represents the center of the Raman signal collecting system. When the sample moves relative to the laser, the variations of the $\omega$ and $\Gamma$ curves are not symmetric. However, if the laser beam focal center is coincident with the Raman spectrometer focal center, the $\omega$ and $\Gamma$ curves would be symmetric.

As the laser spot size is more or less the same with the particle diameter, it can cover about only one particle. Figure 3.4(d) illustrates four relative positions of a particle to the laser, corresponding to the four positions marked in Figure 3.4(b). The red center line shows the center of the laser beam, and the blue dash line represents the signal collecting center of the Raman spectrometer. When the particle is at position I, the laser irradiates the right part of the particle. The laser is focused on the substrate by the particle. As the laser center is of distance from the signal collecting center line, the Raman scattering signal, which comes back to the objective, is not at the laser focal plane. This out-of-focus effect leads to the

variation of Raman signal. It would decrease the wavenumber and increase the linewidth as discussed before. At position II, the laser focal spot through the particle is coincident with the laser beam center. Raman scattering signals are most excited. The Raman intensity reaches maximum. The laser focal point is near the Raman spectrometer center line but not coincident. As a result, the out-of-focus effect still exists. The wavenumber keeps increasing and linewidth continues decreasing when the particle moves towards position III. At position III, the laser focal spot is at the Raman spectrometer center line. Raman scattering signals are well collected by the spectrometer. Wavenumber and linewidth are at their extreme values because the collected Raman signals are from the focal plane of the Raman collecting optical path. There is no out-of-focus effect at position III. The Raman intensity is not quite high because part of the particle is outside of the laser beam. From position III to IV, the collected Raman signals become more out of focus. Thus, the wavenumber reduces and the linewidth rises. In addition, the laser is focused only by part of the particle, so the Raman intensity is becoming weaker. Based on this analysis and the distance between the intensity peak and $\omega$ peak [Figure 3.4(b)] we conclude that the laser focal center and the focal center of the Raman collecting optical path is off by about 374 nm under the 1210 nm particle near-field focusing. Under 400 nm silica particle focusing, the distance between these two focal centers becomes smaller, around 159 nm.

The second reason is that part of the Raman signals come from the silicon wafer under the spacing among particles. As the laser beam is pre-focused on the particles by the objective lens, the focal level for the silicon beneath the particles is at a higher position than the focal plane. This affects the wavenumber and linewidth of silicon. The third reason may

be due to the beam deflection caused by thermal expansion. The local silicon under the particle center is heated by the laser beam and expands. The heated silicon surface is no longer perpendicular to the propagation direction of the laser, which causes beam deflection. The beam deflection affects the Raman signal of silicon.

### 3.2.2 De-conjugation of thermal, stress, and optical effects

For the nanoscale imaging (Figure 3.4) based on Raman intensity, wavenumber, and linewidth, their variation against location reflects a combined effect of near-field optical heating, local stress, and optical field variation in space. Physically, it is possible to de-conjugate these three effects and obtain quantitative information about the nanoscale local stress and temperature. To do this, the Raman spectra for silicon under monolayer silica particles and for bare silicon are compared under four energy fluxes, respectively. The highest energy flux is $3.9 \times 10^9$ W/m$^2$, and the four energy percentages are 25 %, 50 %, 79 %, and 100 %. The integration time is 2 s. The Raman spectra at various sample positions and focal levels are obtained, and position II, as shown in Figure 3.4, is selected to determine the thermal response in silicon. At this position, Raman intensity reaches its maximum value.

First of all, by studying the Raman intensity variation against laser energy, the temperature rise under near-field heating is evaluated. The Raman intensity for silicon under silica particles ( $I_{SiO_2}$ ) and that for bare silicon ( $I_{Si}$ ) are shown in Figure 3.5(a). $I_{SiO_2}$ is higher than $I_{Si}$ for each energy percentage because of the particle focusing. The normalized intensity ratio $I_{SiO_2} / I_{Si}$ decreases linearly with the energy. From the decreasing trend, the

temperature rise information can be extracted. The physics is as follows. There are three main factors that would affect the Raman intensity. Thus the Raman intensity can be expressed as $I = f_1 f_2 f_3(\Delta T)$ where $f_1$ denotes the intensity change due to the system alignment; $f_2$ represents the laser energy effect; and $f_3(\Delta T)$ is the intensity variation induced by the temperature rise. For silicon with silica particles, we have $I_{SiO_2} = f_1 f_2 f_3(\Delta T)$. But for bare silicon, $I_{si}=f_1 f_2$, as the temperature rise is negligible here because of the large thermal conductivity of silicon. $I_{Si}$ is acquired immediately after $I_{SiO_2}$, so $f_1$ and $f_2$ are the same for both $I_{SiO_2}$ and $I_{Si}$ separately. Thus, the intensity ratio is only relative to temperature rise: $I_{SiO_2} / I_{Si} = f_3(\Delta T)$. The Raman intensity of silicon reduces with the increase of temperature. This is because high temperature, which is caused by particle induced heating, changes the band structure in silicon, and it restricts the photon interactions necessary to generate Raman signals. The state density and energy of phonons increase as temperature rises, leading to a reduction of Raman intensity. In order to determine the thermal response inside silicon under laser irradiation, the temperature dependence of Raman intensity is needed. In our calibration, shown in the inset of Figure 3.5(b), the normalized intensity $I/I_0$ for bare silicon decreases with temperature, where $I_0$ is the intensity of silicon at 292.0 K. The attained linear fitting slope for normalized Raman intensity against temperature is -0.00249 $K^{-1}$ at temperatures from 290 to 440 K. Figure 3.5(b) shows that the normalized intensity ratio ($\left[I_{SiO_2} / I_{Si}\right] \Big/ \left[I_{SiO_2} / I_{Si}\right]_{E=0}$) reduces when energy flux increases. Based on the assumption that the decreasing trend of normalized intensity ratio with temperature in the experiments is the same with that in the calibration, the temperature rise inside silicon due to particle

focused laser heating is obtained. Figure 3.5(c) illustrates that $\Delta T$ increases from 10.0 to 56.1 K when the energy percentage goes up from 25 % to 100%. The uncertainty of temperature rise can evaluated according to the uncertainty of intensity ratio at zero laser energy, which is about ±7.0 K.

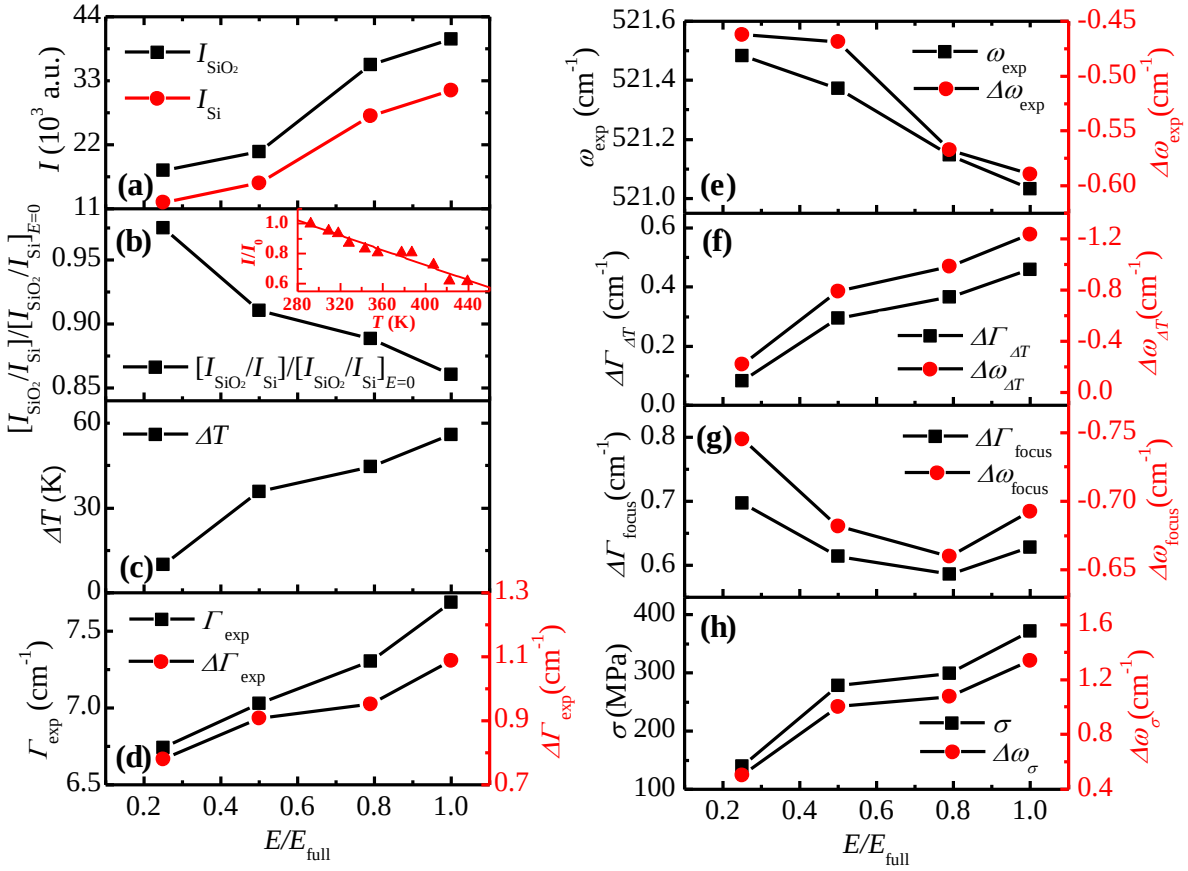


**Figure 3.5 Temperature rise and thermal stress inside silicon under particle-focused laser irradiation. (a) How Raman intensity of silicon under 1210 nm silica particles ( $I_{SiO_2}$ ) and that of pure silicon ( $I_{Si}$ ) vary with energy percentage ($E/E_{full}$). (b) Normalized Raman intensity ratio ( $\left[I_{SiO_2}/I_{Si}\right]/\left[I_{SiO_2}/I_{Si}\right]_{E=0}$ ) and (c) temperature rise ($\Delta T$) versus energy percentage. The inset in figure (b) shows the linear relation between normalized Raman intensity of silicon ($I/I_0$) and temperature with a slope of -0.00249 K$^{-1}$. $I_0$ is the intensity of silicon at 292.0 K. (d) Linewidth and (e) wavenumber of silicon under particles and their differences with those of pure silicon. (f) Wavenumber and linewidth differences due to temperature rise. (g) Wavenumber and linewidth differences due to out-of-focus effect. (h) Thermal stress ($\sigma$) and wavenumber difference induced by stress under different laser energies.**

In order to determine the thermal stress $\sigma$ inside silicon, combined use of wavenumber $\omega$ and linewidth $\Gamma$ is necessary. When the temperature of the material increases, $\omega$ decreases and $\Gamma$ broadens [64]. $\Gamma$ has lower temperature sensitivity than $\omega$. $\Gamma$ is stress insensitive to the first order, while stress causes a shift in $\omega$ [39, 96]. Considering the temperature rise and out-of-focus effect for silicon, the experimental linewidth difference can be expressed as $\Delta\Gamma_{exp} = \Delta\Gamma_{\Delta T} + \Delta\Gamma_{focus}$, where $\Delta\Gamma_{exp}$ is the Raman linewidth difference between silicon under particles and bare silicon; $\Delta\Gamma_{\Delta T}$ is the linewidth difference due to temperature rise; and $\Delta\Gamma_{focus}$ is the linewidth difference because of the out-of-focus effect. For the experimental wavenumber difference, $\Delta\omega_{exp} = \Delta\omega_{\Delta T} + \Delta\omega_{focus} + \Delta\omega_{\sigma}$, where $\Delta\omega_{exp}$ is the wavenumber difference between silicon under particles and bare silicon; $\Delta\omega_{\Delta T}$ is the difference due to temperature rise; $\Delta\omega_{focus}$ is the difference because of the out-of-focus effect; and $\Delta\omega_{\sigma}$ denotes the wavenumber induced by thermal stress. Figure 3.5(d) and (e) show the experimental linewidth and wavenumber of silicon under particles and their differences from those of bare silicon. The standard deviations for linewidth and wavenumber in the data fitting are 0.06 and 0.02 $cm^{-1}$, respectively. From our previous results, the Raman linewidth of silicon increases linearly with temperature and the slope is 0.0082 $cm^{-1}/K$, and the slope for the wavenumber against temperature is -0.022 $cm^{-1}/K$ [95]. Based on the temperature rise ($\Delta T$) calculated from intensity [Figure 3.5(c)], $\Delta\Gamma_{\Delta T}$ and $\Delta\omega_{\Delta T}$ can be obtained according to the slopes [Figure 3.5(f)]. So the Raman linewidth difference due to focus effect is achieved by $\Delta\Gamma_{focus} = \Delta\Gamma_{exp} - \Delta\Gamma_{\Delta T}$. $\Delta\omega_{focus}$ needs to be calculated from $\Delta\Gamma_{focus}$. The experiments to determine the relation between wavenumber and linewidth at different focal levels has been conducted in our lab [95]. The experimental data give a relation of $\Delta\omega_{focus} = -0.21055 -$

$0.76742\Delta\Gamma_{focus}$. Thus, the wavenumber difference due to focus effect is obtained and shown in Figure 3.5(g). The wavenumber induced by stress is given by $\Delta\omega_\sigma = \Delta\omega_{exp} - \Delta\omega_{\Delta T} - \Delta\omega_{focus}$. A relation between the shift of wavenumber $\Delta\omega_\sigma$ and the stress $\sigma$ inside silicon has been developed with a proportionality constant of -3.6 $cm^{-1}$/GPa [39]. Finally, the thermal stress $\sigma$ inside silicon is acquired according to the relation. In Figure 3.5(h), $\sigma$ increases from 140 to 370 MPa as energy percentage of laser goes up from 25 % to 100%. The uncertainty of thermal stress is about ±40 MPa, calculated from the uncertainty of $\Delta\omega_\sigma$. Comparing Figure 3.5(c) and (h), thermal stress goes up as local temperature rise increases, because the developing thermal stress is induced by the temperature gradient. The particle-focused laser beam heats up the silicon under the particle within a small area around 200 nm in radius. The localized heating of the beam causes thermal expansion in the heated area which is constrained by the nearby cold silicon. This constraint places a compressive stress on the heated region.

### 3.2.3 Nanoscale mapping for near-field heating under 800, 400 and 200 nm particles

The experimental method for the 1210 nm case is employed to attain nanoscale imaging for the 800, 400 and 200 nm cases. The results for the 800 nm case are illustrated in Figure 3.6(a). The total travel range along the *x* direction is 1.8 μm with a step of 53 nm. More than two periods are measured. The $I_{max}$ is $2.24 \times 10^4$, $2.82 \times 10^4$, $4.18 \times 10^4$ and $5.96 \times 10^4$ for the four energy percentages of 25 %, 50 %, 79%, and 100 %, respectively. For the 79 % case with energy flux of $3.1 \times 10^9$ W/$m^2$, the second intensity period is 853 nm. The intensity difference and ratio of $I_{max}$ and $I_{min}$ are $2.27 \times 10^4$ and 2.24, respectively. Within a distance

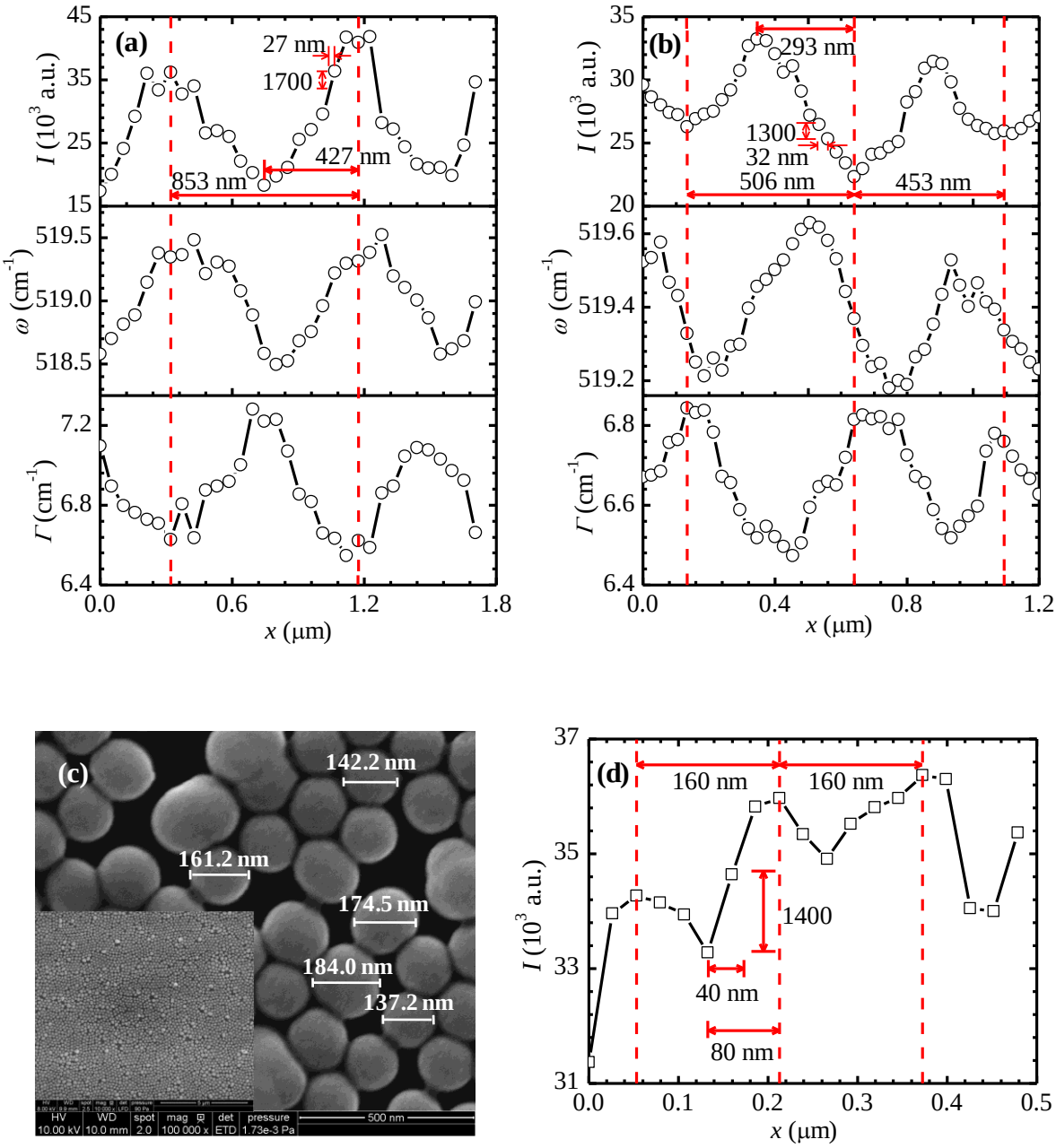


**Figure 3.6 Nanoscale mapping for different sizes of particles. The Raman intensity *I*, wavenumber $\omega$, and linewidth $\Gamma$ for silicon under particles of (a) 800 nm and (b) 400 nm diameters with laser irradiation. (c) SEM images of 200 nm particles on a substrate. The average diameter of the particles is about 160 nm. (d) The Raman intensity of silicon under particles of 200 nm diameter along the *x* direction.**

of 30 nm in the *x* direction, the intensity difference and ratio are 3400 and 1.10, respectively, as shown in Figure 3.6(a). It indicates that the resolution can be reached at about 30 nm in this case. In this period, $\omega$ varies from 518.5 to 519.5 $cm^{-1}$, with a maximum shift of 1.0 $cm^{-1}$. $\Gamma$ varies in a range of 6.5 - 7.3 $cm^{-1}$, with a maximum difference of 0.8 $cm^{-1}$. The variation curves of $\omega$ and $\Gamma$ along the *x* direction are not symmetric, and the reasons are similar with those for the 1210 nm case.

Figure 3.6(b) shows the variation of silicon Raman intensity along the *x* direction for the 400 nm case. The total travel range in the *x* direction is 1.2 μm with a step of 27 nm. The $I_{max}$ is $1.40 \times 10^4$, $1.95 \times 10^4$, $3.36 \times 10^4$ and $4.32 \times 10^4$ for the four energy percentages of 25 %, 50 %, 79 %, and 100%, respectively. In the case of $3.1 \times 10^9$ $W/m^2$, of which the energy percentage is 79 %, the intensity period lengths are 506 and 453 nm. In the first period, the intensity difference between $I_{max}$ and $I_{min}$ is $1.09 \times 10^4$, with a ratio of 1.49. Within a distance change of 30 nm in the *x* direction, the intensity difference and ratio are 1300 and 1.05, respectively, as shown in Figure 3.6(b). In the period, $\Gamma$ varies in a range from 6.5 - 6.9 $cm^{-1}$. $\omega$ changes from 519.2 to 519.6 $cm^{-1}$. The $\Gamma$ and $\omega$ curves are not symmetric, either.

To explore the particle diameter limit of the far-field nanoscale imaging, 200 nm particles are used in the experiments. Figure 3.6(c) shows large areas of 200 nm monolayer particles on silicon. The average diameter of the particles shown in the SEM image is about 160 nm. Nanoscale imaging experiment is conducted along the *x* direction within a travel range of 500 nm with a step of 27 nm. The travel range covers about 3 particles. The laser energy flux is $3.9 \times 10^9$ $W/m^2$ (100 %). The variation of the Raman intensity with *x* is shown in Figure

3.6(d). The two distances between the highest intensities are both 160 nm, which agree well with the particle diameter observed under SEM. $I_{max}$ is about 3.64 $\times$ $10^4$ with a $I_{max}/I_{min}$ of about 1.08 for the first period. The intensity change is about 1400 in a quarter of a period, which is of 40 nm distance, and the intensity ratio is about 1.04 within this distance. For this imaging, it is conclusive the imaging resolution can reach 40 nm. Figure 3.7 shows how the maximum Raman intensity ratio ($I_{max}/I_{min}$) varies with particle diameter under different energy fluxes. $I_{max}/I_{min}$ drops exponentially with the decrease of the particle size, and increases with the energy flux. As the particle size decreases from 1120 to 160 nm, $I_{max}/I_{min}$ reduces from about 4.8 to 1.1. With the decreasing trend, when the diameter of particles drops to 140 nm, it would be hard to tell the intensity difference within a period. And the resolution improves with the increase of the particle size. The best resolution is about 20 nm when the particle diameter is 1120 nm in our experiments.

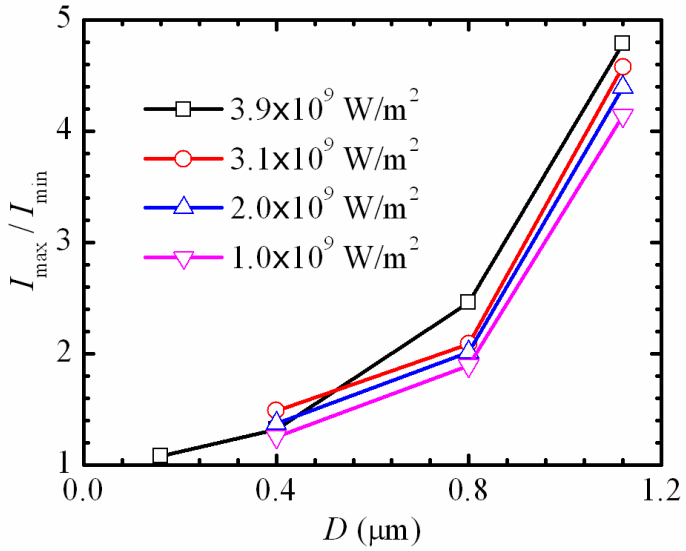


**Figure 3.7 The variation of maximum Raman intensity ratio of silicon with particle size under four laser energy fluxes.**

### 3.3. Physics behind Nanoscale Mapping

When a uniform laser beam interacts with a particle-substrate system, the laser is focused by the microparticle in a near-field region near the contacting point of the particle and the substrate. As the silica particle is transparent to green light, the particle absorbs little laser energy. Strong energy absorption occurs in the silicon substrate under the particle within a tiny elliptical cone near the surface. The amplitude of electric field in silicon at the contacting point is the highest, and it attenuates from the surface to the inside of the substrate. The photon's energy is converted into vibrations of the molecules called phonons in the substrate, which produces thermal energy. The temperature rises in the laser focusing and heating region and it causes thermal expansion. The thermal expansion of heated silicon is constrained by the nearby cold silicon, which places a compressive stress in the local region. To understand the mechanism of temperature and stress rise in the particle-substrate system, electromagnetic simulation is conducted with finite element analysis using the high frequency structure simulator (HFSS V14, ANSYS). Only the 1210 nm case is studied. Other cases can be treated similarly. In consideration of the amount of calculation and mesh density in HFSS, a quarter of the original model is employed. The remaining model is set to be symmetrical in both electric and magnetic directions. A plane wave ($\lambda$ = 532 nm) is incident normally from the top. In the experiment, the laser spot area is about the diameter size; only the particles in the spot area are under irradiation; no light irradiates the particles outside that area. To meet the experimental condition, only the parts of particles inside the laser spot area remain in the model. Other parts of particles outside the area are cut off to avoid receiving the plane wave. Perfect *H* and Perfect *E* symmetry boundaries are adopted at symmetrical planes. Absorbing (radiation) boundaries are applied for other boundary planes in the

domain. The electric field amplitude of the incident wave is set to 1 V/m. Therefore, the near-field enhancement value is the same as the electric field amplitude of the scattered light. Two typical cases regarding to different laser-particle positions in an imaging period are simulated. Figure 3.8 shows the electric field distributions inside the substrate-particle system for the two cases. In the left case, the particle center is under the laser spot center, where the maximum enhancement is achieved in an imaging period. In the right case, the particle center is at the fringe of the laser spot, and the enhancement is the minimum in a period. The highest enhancement values for the two cases are 2.8 and 1.6 inside the substrate, and 6.4 and 4.8 inside the substrate-particle system. The maximum enhancement ratio of light intensity in the simulation is only 3.1, smaller than the maximum Raman intensity ratio in the experiments (4.8). The reasons for the difference will be discussed later. The laser focusing areas in silicon are right beneath the particles which are under laser irradiation, with a radius of about 200 nm.

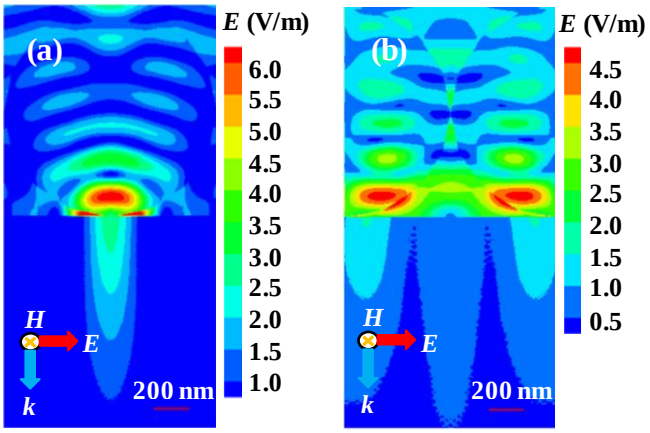


**Figure 3.8 HFSS modeling of a plane wave passing through a 1.21 μm silica sphere ($\varepsilon$ = 2.13 + 0*i*) in air above a silicon substrate ($\varepsilon$ = 17.22 + 0.428*i*). The amplitude of electric field is equal to the enhancement factor. (a) The particle center is under the laser spot center. (b) The particle center is at the fringe of the laser spot area.**

The temperature distribution inside the silicon substrate is simulated using FLUENT (V12.0.1, ANSYS) based on the electric field distribution. The 1210 nm case with the highest energy and electric field enhancement is simulated in this work. As the temperature distribution inside silicon is symmetric, a quarter-cylinder computational domain with a radius of 5 μm and a height of 10 μm is employed in the simulation. The top end surface of silicon is set as adiabatic. Both vertical cross-sections use symmetric boundary conditions. The peripheral and foot end surfaces of the domain and the initial temperature of the substrate are set at 300 K. The heat source is imported from the HFSS calculation results. The heat generation rate per unit volume can be calculated from $\dot{q} = I\beta$, where $\beta = 4\pi\kappa/\lambda$ is the absorption coefficient, $\kappa$ is the extinction coefficient, $\lambda$ is the wavelength of incident laser, and $I = P = 0.5c\varepsilon_0 nE^2$ is the laser intensity inside the silicon substrate, which is equal to the Poynting vector. The light speed in free space $c = 3 \times 10^8$ m/s, the vacuum permittivity $\varepsilon_0 = 8.854 \times 10^{-12}$ F/m, the refractive index of silicon $n = 4.15$, and $E$ (V/m) the time-average intensity of the electric field, which is acquired using HFSS. Other details of the temperature simulation can be found elsewhere [95]. Figure 3.9 shows the temperature profile inside silicon from the surface to the bottom under the particle. The inset illustrates the steady state symmetric temperature distribution on the surface of the silicon substrate. The calculated maximum temperature rise inside the silicon is 50.9 K, which is close to the experimental value (56.1 K).

For the 1210 nm particle case, the maximum enhancement ratio of light intensity in the simulation is only 3.1, smaller than the maximum Raman intensity ratio in the experiments

(4.8). There are four main factors considered leading to the differences between experiments and simulation. The first factor is the relationship between the collected Raman signal and the distance between the objective lens and the focusing point, as shown in Figure 3.10(a). The collected Raman signal is the strongest when the focusing point inside silicon is at the center of the objective lens; see position 1 in the figure. The signal decreases with the increase of the distance between focusing location and the lens center during the scanning process. Position 2 represents a situation that some Raman signals do not come into the lens through the particle. Instead, they are missed by the Raman spectrometer. So the amount of collected Raman signals reduces. As a result, the collected Raman intensity ratio between position 1 and 2 rises. Second, Raman intensity of silicon varies with focal level in the vertical direction, as shown in Figure 3.10(b). The Raman intensity reaches maximum at the focal plane, and decreases with the distance between the sample and laser focal plane position in the *z* direction. So the maximum Raman intensity at the focal plane is much higher than that at an out-of-focus status. Third, the incident laser employed in the electric field simulation is a uniform plane wave, while in the experiments the laser is focused by a 100× objective lens before it irradiates the sample. Although the laser is still uniformly distributed in space, the direction of propagation has been changed. The laser should be focused in an even smaller region by the particles, which brings in higher temperature rise in the focused region. Finally, during the simulation of electromagnetic field by HFSS, the dimensions of the computational domain are quite large. The grid is not fine enough, so the precision of the computational results may drop to a certain extent.

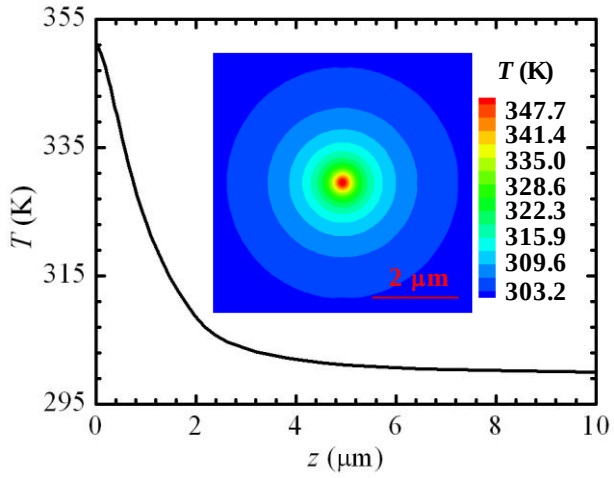


**Figure 3.9 Temperature profile inside a silicon substrate beneath a 1210-nm silica particle under laser irradiation. The inset shows the temperature distribution on the top of the substrate.**

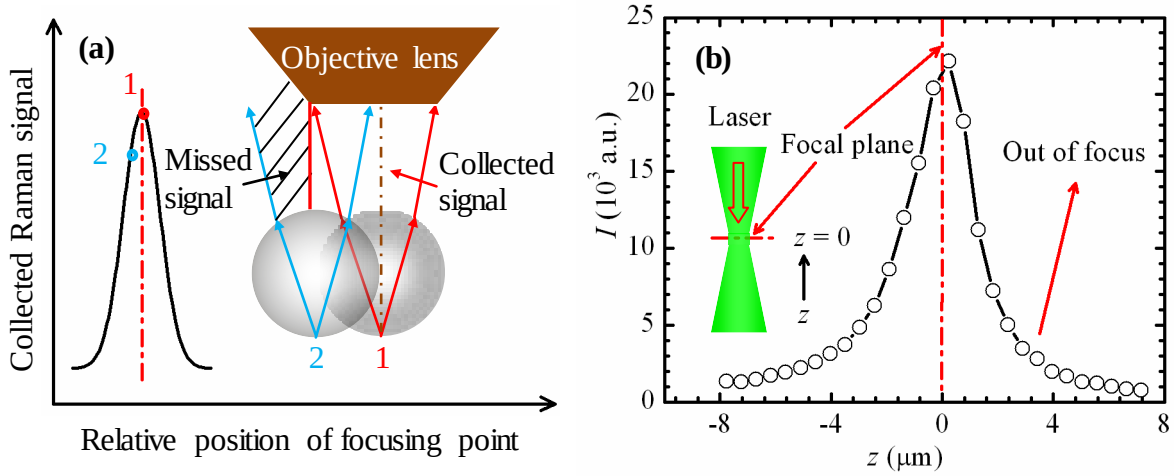


**Figure 3.10 Illustration of the difference between experimental and modeling results. (a) How the collected Raman signal varies with distance between the center of objective lens and laser focusing point in silicon. Position 1 represents the coincidence of the focusing point and the lens center, and position 2 shows a distance between them. (b) The variation of silicon Raman intensity with the laser focal level in the vertical direction.**

# CHAPTER 4. THERMAL PROBING IN SINGLE MICROPARTICLE AND MICROFIBER INDUCED NEAR-FIELD LASER FOCUSING

In this chapter, far-field nanoscale mapping of conjugated structural, thermal, and stress effects in silicon beneath a single microparticle and microfiber is conducted for the first time using Raman spectroscopy. The structural, thermal, and stress effects are de-conjugated from the Raman mapping. The thermal response of a silicon substrate beneath single silica particle and glass fiber with laser irradiation is performed. The intensity, temperature, and stress fields inside silicon are simulated to interpret the measurement results.

## 4.1. Experimental Setup and Details

Figure 4.1(a) shows schematic of the experimental setup for the near-field focusing. The Raman scattering system consists of a confocal Raman spectrometer (Voyage$^{TM}$, B&W Tek) and a microscope (Olympus BX51). The laser beam ($\lambda$ = 532 nm) is focused by a 100× objective lens (NA = 0.80). The movements of the sample are controlled by a piezo-actuated nano-stage (ThorLabs NFL5DP20) in the *x* direction and a motorized micro-stage (ThorLabs MT1-Z8) in the *z* direction. The piezo-actuated range of the nano-stage is 20 μm with a resolution of 20 nm. The control range of the micro-stage is 12 mm with a resolution of ±0.1 μm. With a locking screw, the micro-stage can remain at a desired vertical position without drift during the experiment. The incident laser used as both Raman probing and heating source is focused on a single silica particle by the objective lens. Due to the focusing effect of the particle, the laser beam is further focused on the silicon substrate and heats it up. The sample consists of several single 1.21 μm silica particles (Bangs Laboratories) and a silicon

(100) substrate (University Wafer). Single particles are patterned on a wafer using a tilting technique [77]. Monodisperse particle suspensions mixed with surfactant (triton-X: methanol = 1:400 by volume) are dispensed onto a wafer using a syringe and left to dry for 0.5 h in the air. The wafer is tilted on a table with an angle of about 10° to help in the flow of the mixture solution on the wafer. Figure 4.1(b) shows scanning electron microscope (SEM) images of single silica particles on a silicon wafer. The diameter of the particles is about 1.20 μm, while the laser spot size is about 0.5 μm under 100× magnification. The laser spot size is determined using a blade method. By moving a blade along two perpendicular directions to shade the laser beam, the laser energy is found decreasing linearly with the moving distance. The laser spot length covering 90 % of the laser energy is chosen to represent the spot size.

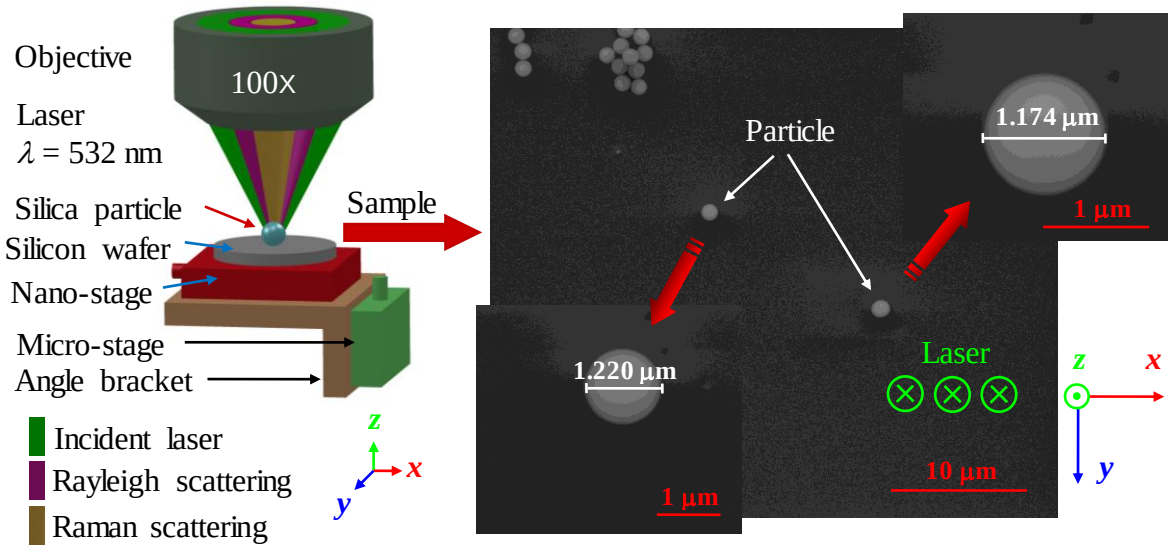


**(a) Experimental setup** **(b) Single silica particle on a silicon substrate**

**Figure 4.1 Schematic of experimental setup for near-field thermal probing (not to scale). (a) A sample is located under an objective-focused laser beam from a Raman spectrometer. The movement of sample in the *x* direction is controlled by a piezo-actuated nano-stage. The focal level of the laser on the sample in the *z* direction is controlled by a motorized micro-stage. (b) The sample consists of a silicon substrate and a monolayer of silica particles. The spot size of the incident laser is about 0.5 $\mu$m in the *x*-*y* plane on a silicon substrate.**

To conduct the Raman mapping experiments, a microparticle is identified under the microscope. The Raman intensity reaches its maximum value where the laser beam is focused on the particle center. A 3-D scanning process is employed to determine this focusing position. The sample is scanned along the *y* direction covering the particle center with a step of 53 nm. Raman spectra are obtained at all these positions and compared. The sample is moved back to the position where the maximum Raman intensity in the *y* direction is located. There is no sample movement in the *y* direction in the following process. A similar process is taken to determine the focusing position in the *x* direction. The scanning process in the *z* direction is followed in order to determine the focal level. Raman spectrum is affected by the focal level even other environmental factors are fixed. Wavenumber and intensity decrease, and linewidth broadens when the sample moves away from the focal plane in the *z* direction [95]. Raman intensity would decrease by at least 5 % when the sample position is of 533 nm distance from the laser focal position. In the experiments, the position of the sample is adjusted near the focal plane and Raman spectra are obtained at each focal level. The focal level is selected with the highest Raman intensity in the *z* direction. Now the sample is located where maximum intensity exists in all the three dimensions. The position of the sample in the *y* and *z* directions is then fixed. The sample is moved away from the center of the particle in the *x* direction to start the mapping experiment. The sample is scanned along the *x* direction, as shown in Figure 4.2. The movement is controlled electrically without any touch of the sample, stage, Raman spectrometer, microscope and other related equipment that would affect the quality of Raman signal. The variation of Raman spectra with the sample location is achieved at the nanoscale.

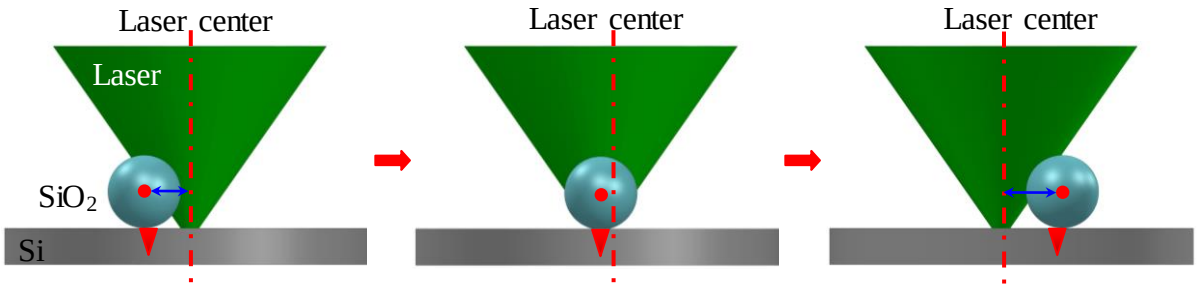


**Figure 4.2 Movements of sample relative to the incident laser in the *x* direction. During the experiment, the position of the laser beam is fixed, and the sample moves along the *x* direction controlled by the nano-stage electrically without any touch of the sample and other equipment.**

To evaluate the temperature rise and thermal stress in the particle-induced near-field laser focusing, experiments on silicon with single particles on the surface and bare silicon with no particles are both performed. A 3-D scanning process as mentioned above is also carried out to determine the focusing position. The incident laser is first focused on one single particle on the Si substrate, and the Raman spectra are taken under four energy levels. Bare silicon is located around the particle. Raman spectra of bare silicon are obtained under four energy levels after shifting the particle away to allow direct laser irradiation on bare silicon. The integration time and measurement average are all the same (detailed later). A group of data for Raman spectra at different focal levels around the focal plane is obtained for each case. The Raman spectrum with the highest intensity is selected to represent each result. The environmental differences among those cases are extremely minimized, and the temperature rise and local stress are determined.

## 4.2. Results and Discussion

### 4.2.1 Near-field focusing under a single microparticle

A single silica particle is found under the confocal microscope. Raman mapping for

silicon beneath the single particle is obtained under laser irradiation of $3.7 \times 10^9$ W/m$^2$ with an integration time of 2 s. The Gaussian function is employed to fit the experimental Raman data. The particle is moved relative to the laser along the *x* direction within a range of 3 μm with a step of 53 nm. The Raman intensity *I* of silicon first increases and then decreases with the movement of sample [Figure 4.3(a)]. The difference between the highest ($I_{max}$) and lowest ($I_{min}$) Raman intensities is 8000, with an intensity ratio ($I_{max}/I_{min}$) of 3.86. The distance from $I_{max}$ decreasing to $I_{min}$ is 692 nm. 1/32 of the distance is about 22 nm with an intensity difference and intensity ratio of about 400 and 1.08, respectively. As the intensity is the raw datum without any further processing, it is the best quality to specify the imaging resolution. It is conclusive that the imaging resolution based on the Raman intensity difference can be down to 22 nm, although the step length in the experiments is 53 nm. During the imaging process, wavenumber $\omega$ first increases from 519.1 to 520.0 cm$^{-1}$, and then keeps constant. At position I in Figure 4.3(a), as part of the particle is under laser irradiation, $\omega$ starts to increase. At position II, *I* reaches its maximum $I_{max}$, where $\omega$ is about 520.2 cm$^{-1}$. $\omega$ continues increasing to its maximum (520.5 cm$^{-1}$) at position III within a distance of 319 nm, and then decreases to its minimum. Linewidth $\Gamma$ changes in a range from 6.3 to 8.0 cm$^{-1}$, with a maximum difference of 1.7 cm$^{-1}$. The variation tendency of $\Gamma$ is contrary to that of $\omega$. It first decreases and then increases.

The increasing and decreasing distances for *I* and $\omega$ are not equal, and the positions of their maximums are not coincident. Figure 4.3(b) illustrates the mechanism behind these differences. The focal spot center of the excitation laser (black line) and the signal collecting

center of the Raman spectrometer (red line) are off a little (not exactly confocal). The Raman spectrometer, excitation laser, and microscope are designed to be confocal. However, due to the accuracy of the assembling process and the vibration during the transportation of the equipment, misalignment at a scale of a few nanometers occurs and it is difficult to avoid. For a regular sample with flat surface, the effect of the misalignment is not significant. However, the sample used in our experiment is a substrate with a focusing element (microparticle) on the surface. In addition, the diameter of the particle is comparable with the scale of the misalignment. Thus, the misalignment becomes an important factor in obtaining high measurement accuracy. In our experiments, when the sample moves relative to the laser, the variations of Raman curves are not symmetric. The four relative positions of the particle to the laser are corresponding to the same marks in Figure 4.3(a). At position I, the laser irradiates the right part of the particle and is focused on the substrate. As the laser center is of distance from the signal collecting central line, the Raman scattering signal, which comes back to the objective, is not at the focal plane. This out-of-focus effect leads to the variation of Raman signal. It would decrease $I$ and $\omega$. At position II, the laser focal spot through the particle is coincident with the laser beam center. Raman scattering signals are most excited and $I_{max}$ exists. The laser focal point is near the Raman spectrometer central line but not coincident. As a result, the out-of-focus effect still exists. $\omega$ keeps increasing and $I$ continues decreasing when the particle moves towards position III. At position III, the laser focal spot is at the Raman spectrometer central line. Raman scattering signals are well collected by the spectrometer. There is no out-of-focus effect at position III. $\omega$ reaches its maximum because the collected Raman signals from the focal plane of the Raman collecting optical path. $I$ is not quite high as part of the particle is outside of the laser beam. From

position III to IV, the collected Raman signal becomes more out of focus, so $I$ and $\omega$ go down. In addition, $I$ becomes weaker as the particle moves out of the laser beam. Based on this analysis and the distance between $I_{max}$ and $\omega_{max}$, we conclude that the laser beam axis and the Raman signal collecting optical path is off by about 319 nm under the 1210 nm particle near-field focusing. For different focusing elements, such as a microfiber, and diameters, the focusing conditions are different due to the geometry difference. The offset of the two axes on the sample would be different, which will be demonstrated in the next section.

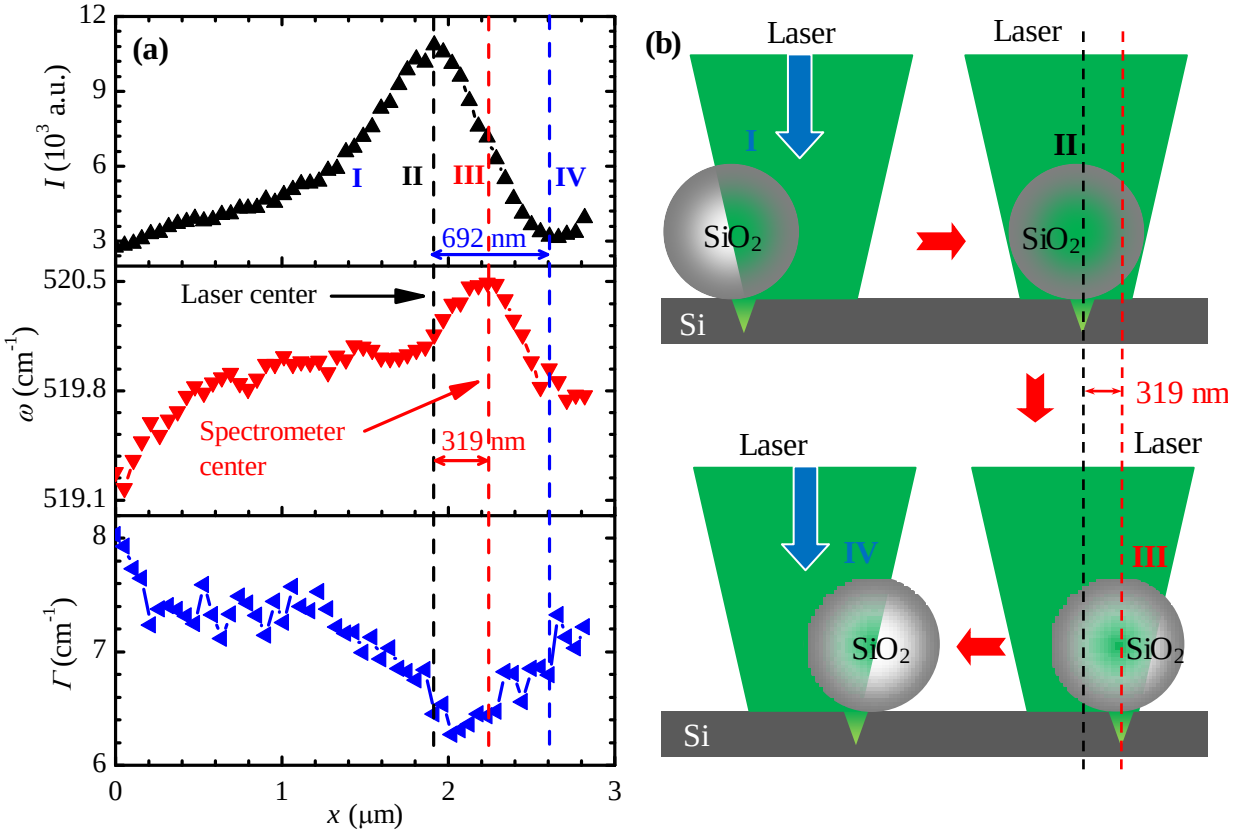


**Figure 4.3 Raman mapping inside silicon under single-particle-focused laser irradiation. (a) The *x* direction variation of Raman intensity *I*, wavenumber $\omega$, and linewidth $\Gamma$ for silicon under particles of 1210 nm diameter with laser irradiation. (b) The relative position of a silica particle and the laser beam to explain the observed Raman variation in space.**

For the nanoscale imaging based on Raman intensity, wavenumber, and linewidth, their variation against location reflects combined effects of near-field optical heating, local stress, and structural variation in space. These three effects are de-conjugated in this section to obtain quantitative information about the nanoscale local stress and temperature. To do this, the Raman spectra for silicon under a silica particle and those for bare silicon are compared. Four laser energy levels of 25 %, 50 %, 79 %, and 100 % are used in our experiments, with a full energy flux ($E_{\text{full}}$) of 3.9 $\times$ $10^9$ W/m$^2$. The temperature rise is first evaluated based on the Raman intensity ratio. The Raman spectra at various focal levels are obtained, and position II, as shown in Figure 4.3(a), is selected to determine the thermal response in silicon. At this focal level, Raman intensity reaches its maximum value. The Raman intensity for silicon under a silica particle ( $I_{\text{SiO}_2}$ ) is higher than that for bare silicon ( $I_{\text{Si}}$ ) due to the near-field focusing, as shown in Figure 4.4(a). Raman intensity can be expressed as $I = f_1 f_2 f_3(\Delta T)$, where $f_1$ denotes the effect of the system optical alignment; $f_2$ represents the laser energy effect; and $f_3(\Delta T)$ is the intensity variation induced by the temperature rise. For silicon with silica particles, $I_{\text{SiO}_2} = f_1 f_2 f_3(\Delta T)$ . But for bare silicon, we have $I_{\text{Si}} = f_1 f_2$ , as the temperature rise is negligible here because of the large thermal conductivity of silicon. $I_{\text{Si}}$ is acquired immediately after $I_{\text{SiO}_2}$, so $f_1$ and $f_2$ are the same for both $I_{\text{Si}}$ and $I_{\text{SiO}_2}$. Thus, the intensity ratio is only relative to temperature rise: $I_{\text{SiO}_2}/I_{\text{Si}} = f_3(\Delta T)$. The Raman intensity of silicon reduces with the increase of temperature for the reason that high temperature changes the band structure in silicon, and it restricts the photon interactions necessary to generate Raman signals. The temperature dependence of Raman intensity has been calibrated in our previous work [95]. The normalized Raman intensity of silicon decreases with temperature at

a slope of -0.00249 $K^{-1}$ within a temperature range of 290 - 440 K. In this experiment, the intensity ratios ( $I_{SiO_2}/I_{Si}$ ) at different energy levels are shown in the first panel of Figure 4.4(b). First of all, we obtain the original intensity ratio: $I_{SiO_2}/I_{Si}$, then based on this ratio change against the last energy, extrapolation is conducted to determine the ratio at zero laser energy $\left[I_{SiO_2}/I_{Si}\right]_{E=0}$. To eliminate the effect of particle-induced laser focusing condition, the normalized intensity ratio is introduced as $\left[I_{SiO_2}/I_{Si}\right]/\left[I_{SiO_2}/I_{Si}\right]_{E=0}$. The normalized intensity ratio is only dependent on the temperature rise, and is shown in the first panel of Figure 4.4(b). The percentage of intensity decrease in particle induced near-field heating determines the amount of temperature rise in silicon. According to the calibrated slope, the temperature rise ($\Delta T$) increases from 13.8 to 58.5 K when the energy level goes up from 25 % to 100%. The uncertainty of temperature rise can evaluated according to the uncertainty of intensity ratio at zero laser energy, which is 0.01167. Based on the relationship between intensity ratio and temperature change (-0.00249 $K^{-1}$), the error level of temperature rise is $\pm$ 4.7 K.

In order to determine the thermal stress $\sigma$ inside silicon, combined use of wavenumber $\omega$ and linewidth $\Gamma$ is necessary. When the temperature of the material increases, $\omega$ decreases and $\Gamma$ broadens [64]. $\Gamma$ is stress insensitive to the first order, while stress causes a shift in $\omega$ [39, 96]. Considering the temperature rise and out-of-focus effect for silicon, the experimental linewidth difference between silicon under particles and bare silicon can be expressed as $\Delta\Gamma_{exp} = \Delta\Gamma_{\Delta T} + \Delta\Gamma_{focus}$, where $\Delta\Gamma_{\Delta T}$ is due to temperature rise; and $\Delta\Gamma_{focus}$ is

because of the out-of-focus effect. For the experimental wavenumber difference, $\Delta\omega_{exp}$ = $\Delta\omega_{\Delta T}$ + $\Delta\omega_{focus}$ + $\Delta\omega_{\sigma}$, where $\Delta\omega_{\Delta T}$ is due to temperature rise; $\Delta\omega_{focus}$ is because of the out-of-focus effect; and $\Delta\omega_{\sigma}$ is induced by thermal stress. Raman linewidth of silicon increases linearly with temperature and the slope is 0.0082 $cm^{-1}$/K, and the slope for the wavenumber against temperature is -0.022 $cm^{-1}$/K [95]. Based on the temperature rise ($\Delta T$) calculated from intensity ratio, $\Delta\Gamma_{\Delta T}$ and $\Delta\omega_{\Delta T}$ can be obtained according to the slope, and the results are shown in the second panel of Figure 4.4(b). So $\Delta\Gamma_{focus}$ = $\Delta\Gamma_{exp}$ - $\Delta\Gamma_{\Delta T}$, and the result is shown in the third panel of Figure 4.4(b). $\Delta\omega_{focus}$ needs to be calculated from $\Delta\Gamma_{focus}$.

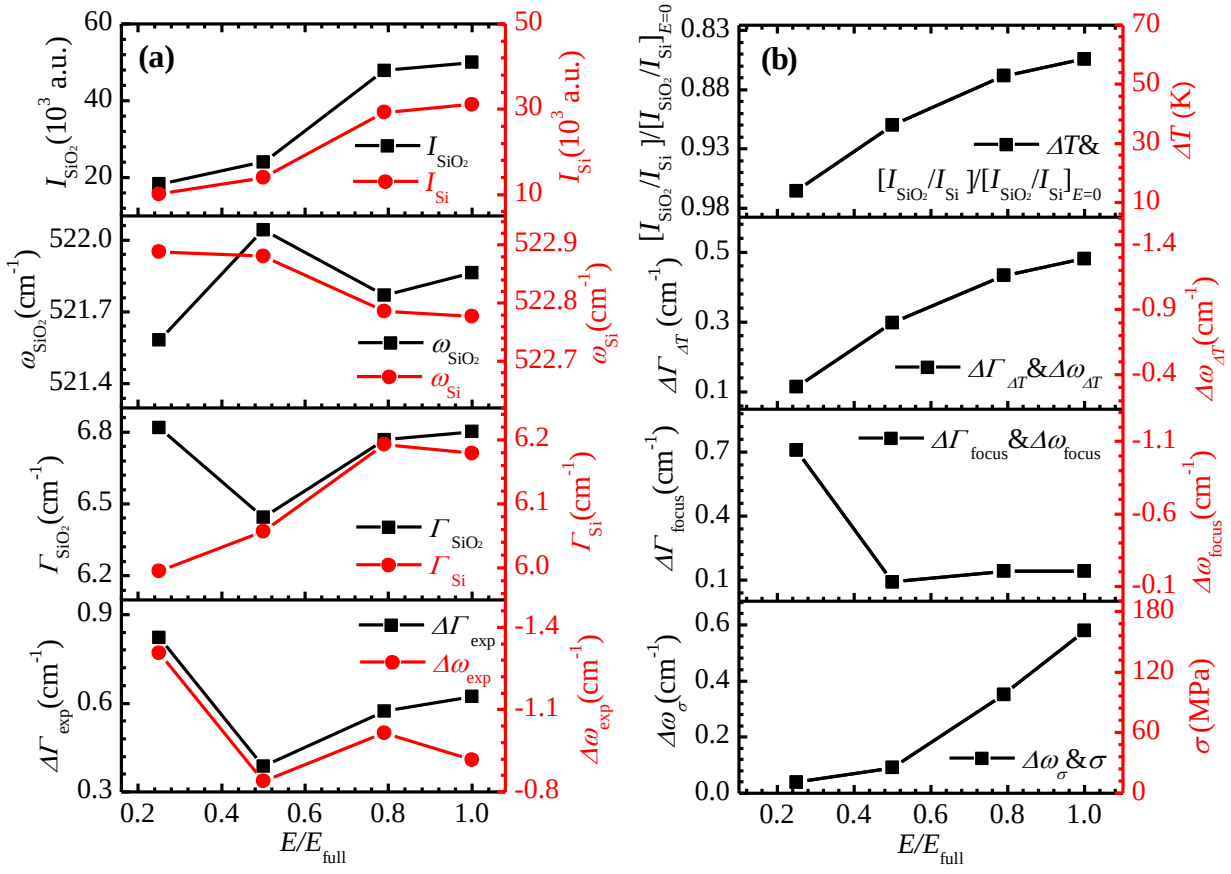


**Figure 4.4 Thermal probing inside silicon under single-particle-focused laser irradiation. (a) How Raman data of silicon under 1210 nm silica particle and that of pure silicon vary with energy percentage. (b) Temperature rise and thermal stress in silicon under different laser energies.**

The experiments to determine the relation between wavenumber and linewidth at different focal levels has been conducted in our group [95]. The experimental data give a relation of $\Delta\omega_{\text{focus}} = -0.21055 - 0.76742\Delta\Gamma_{\text{focus}}$, and the result is also included in the third panel of Figure 4.4(b). The wavenumber induced by stress is given by $\Delta\omega_{\sigma} = \Delta\omega_{\text{exp}} - \Delta\omega_{\Delta T} - \Delta\omega_{\text{focus}}$, and the values are shown in the fourth panel of Figure 4.4(b). A relation between the shift of wavenumber $\Delta\omega_{\sigma}$ and the stress $\sigma$ inside silicon has been developed with a proportionality constant of -3.6 $\text{cm}^{-1}$/GPa [39]. Finally, the thermal stress $\sigma$ inside silicon is acquired according to the relation, and is shown in the fourth panel of Figure 4.4(b). In Figure 4.4(b), $\sigma$ increases from 10 to 160 MPa as energy level goes up from 25 % to 100%. The uncertainty of $\sigma$ can be calculated from that of $\Delta\omega_{\sigma}$, which is $\Delta\omega_{\sigma} = \Delta\omega_{\text{exp}} - \Delta\omega_{\Delta T} - \Delta\omega_{\text{focus}}$. The experimental error of $\Delta T$ is $\pm 4.7$ K. Based on the relationship between wavenumber and temperature (-0.022 $\text{cm}^{-1}$/K), the uncertainty of $\Delta\omega_{\Delta T}$ is $\pm 0.10$ $\text{cm}^{-1}$. The experimental error of $\Delta\omega_{\text{exp}}$ is $\pm 0.02$ $\text{cm}^{-1}$. Here the error of $\Delta\omega_{\text{focus}}$ is pretty small, which can be negligible. Thus, the combined standard uncertainty of $\Delta\omega_{\sigma}$ is determined as about $\pm 0.10$ $\text{cm}^{-1}$. $\sigma$ is proportional to $\Delta\omega_{\sigma}$ with a slope of -3.6 $\text{cm}^{-1}$/GPa, so the uncertainty of thermal stress is $\pm 28$ MPa. The thermal stress goes up as local temperature increases, because the developing thermal stress is induced by the temperature gradient in space. The particle-focused laser beam heats up the silicon under the particle within a very small area around 200 nm in radius (detailed in the modeling section). The localized heating by the laser beam causes thermal expansion in the heated area which is constrained by the nearby cold silicon. This constraint places a compressive stress on the heated region.

4.2.2 Near-field focusing by a single silica microfiber

To explore the near-field effect in silicon beneath single microfiber under laser focusing, the mapping and thermal probing experiments are conducted with a 6 μm glass fiber. Figure 4.5(a) shows SEM images of a glass fiber (Mo-Sci Corp.) on a silicon wafer. The average diameter of the glass fiber is 6.24 μm. A 3-D scanning process is employed to ensure the laser focusing position. Raman mapping experiments are carried out twice for silicon beneath a single glass fiber under laser irradiation of $3.1 \times 10^9$ W/m$^2$. The laser is focused on glass fiber. The sample moves relative to the laser along the $x$ direction in a range of 16 μm with a step of 267 nm. The integration time is 4 s. Figure 4.5(b) illustrates the variations of $I$, $\omega$, and $\Gamma$ with $x$ for the first imaging experiment. In this experiment, we see little difference between the two imaging experiments, so only the first one is analyzed in detail. When the laser beam approaches the glass fiber, $I$ first decreases to $I_{min}$, and $\omega$ increases to $\omega_{max}$. This is because only a small portion of the laser beam is focused by the glass fiber at a position of about 2-3 μm away from the objective center in the $x$ direction, and the Raman signal is mostly missed by the collecting system. At position I as shown in Figure 4.5(b), the fiber center moves closer to the laser center; both $I$ and $\omega$ increase. When the laser focal center and the fiber center are coincident (position II, black line), $I$ reaches $I_{max}$, but $\omega$ would continue rising a little bit due to the out-of-focus effect. At position III, the laser focal center meets the Raman spectrometer central line (red line). $I$ is a little smaller than $I_{max}$ and $\omega$ reaches $\omega_{max}$. There is no out-of-focus effect at this situation. Then the fiber moves away from the laser center, and the variations of $I$ and $\omega$ are reverse to the situation of that the fiber approaches the laser

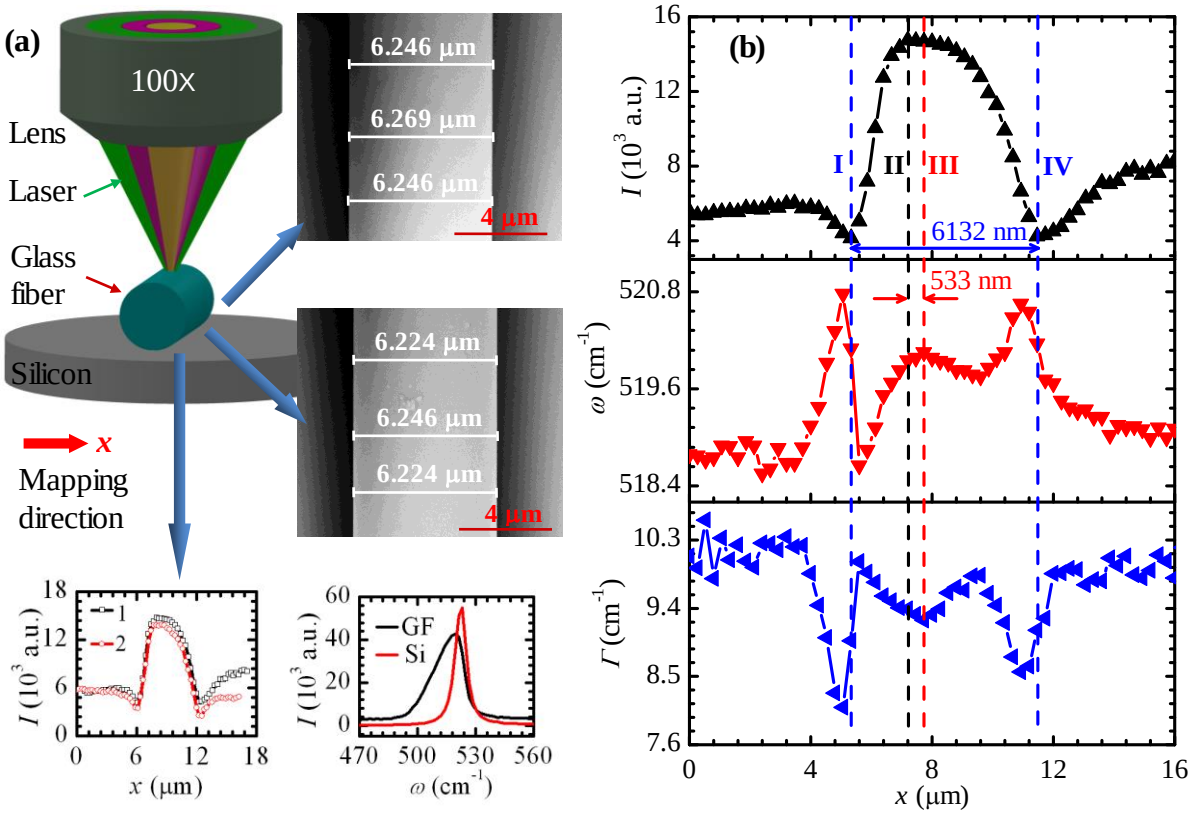


**Figure 4.5 Raman mapping inside silicon under single-fiber-focused laser irradiation. (a) SEM images of microfiber and Raman spectra and Raman intensity variation in the imaging direction. (b) The *x* direction variation of Raman intensity *I*, wavenumber $\omega$, and linewidth $\Gamma$ for silicon under microfiber with laser irradiation.**

beam. The maximum intensity difference ($I_{max}$-$I_{min}$) is 10600, with an intensity ratio ($I_{max}/I_{min}$) of 3.56. The distance between the two $I_{min}$s is 6.132 μm, close to the fiber diameter (6.240 μm). $\omega$ changes in a range from 518.6 - 520.8 $cm^{-1}$, and $\Gamma$ varies from 8.1 - 10.6 $cm^{-1}$. The variation of $\Gamma$ is contrary to that of $\omega$. As shown in Figure 4.5(b), we see more complicated variation of $\omega$ and $\Gamma$ against the location than that for the single particle discussed in the last section. This is largely due the geometry complication induced by the large size of the fiber.

Raman spectra for silicon under glass fiber and those for bare silicon are compared [Figure 4.6(a)] to de-conjugate the combined effect of near-field optical heating, temperature, and stress variation in space. Four laser energy percentages of 25 %, 50 %, 79 %, and 100 % are used with the highest energy flux of $3.9 \times 10^9$ W/m$^2$. Raman spectra for both cases are taken at different focal levels near focal spot to find the highest Raman intensities. The Raman spectra are chosen for analysis at position II as shown in Figure 4.5(b), where intensity reaches its maximum. Figure 4.6(a) shows the Raman intensity for silicon under glass fiber ($I_{GF}$) and that for bare silicon ($I_{Si}$). Also shown in Figure 4.6(a) are the related wavenumber, and linewidth. The integration time for $I_{GF}$ and $I_{Si}$ is 8s and 4s, respectively. The experimental wavenumber and linewidth for both cases, and their differences $\Delta\omega_{exp}$ and $\Delta\Gamma_{exp}$ are also obtained and shown in Figure 4.6(a). The wavenumber and linewidth differences due to the heating ($\Delta\Gamma_{\Delta T}$ and $\Delta\omega_{\Delta T}$), and the focusing effects ($\Delta\Gamma_{focus}$ and $\Delta\omega_{focus}$) are achieved following the same process for single silica particle. When the laser energy changes from 25 % to 100%, $\left[I_{GF}/I_{Si}\right]/\left[I_{GF}/I_{Si}\right]_{E=0}$ in Figure 4.6(b) reduces from 0.98 to 0.92, $\Delta T$ increases from 7.6 to 33.0 K, and $\Delta\omega_\sigma$ increases from 0.5 to 0.8 cm$^{-1}$. The stress $\sigma$ which is directly computed from $\Delta\omega_\sigma$ increases from 137 to 230 MPa while $E$ increases from 25 % to 100 %. Through extrapolation, the calculated stress is 110 MPa at $E$ = 0. However, it should be zero when the laser is off. There might be some reason that causes the calculated non-zero stress at zero laser energy. To make $\sigma$ = 0 at $E$ = 0, all the calculated stresses are subtracted by 110 MPa. The real compressive stress is obtained and shown in the last panel of Figure 4.6(b). $\sigma$ varies from 27 to 120 MPa as $E$ goes up from 25 % to 100 %. The uncertainty of temperature rise in this case is $\pm$ 1.9 K, according to the experimental error of

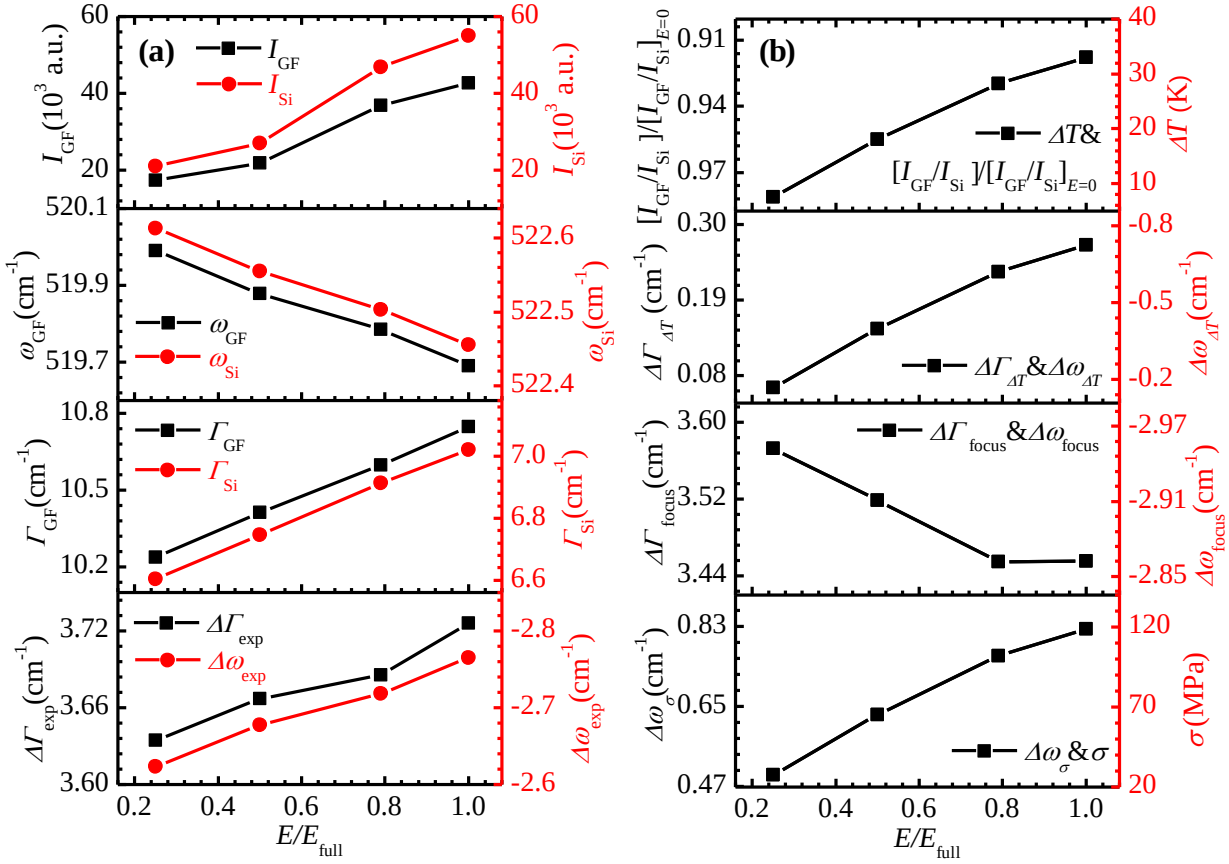


**Figure 4.6 Thermal probing inside silicon under single-fiber-focused laser irradiation. (a) How Raman data of silicon under glass fiber and that of pure silicon vary with energy percentage. (b) Temperature rise and thermal stress in silicon under different laser energies.**

intensity ratio at zero energy (0.00462). The uncertainties of $\Delta\omega_{exp}$ and $\Delta\omega_{exp}$ are $\pm 0.04\text{cm}^{-1}$ and $\pm 0.02$ cm$^{-1}$, respectively. The combined standard uncertainty of $\Delta\omega_{\sigma}$ is determined as $\pm 0.045$ cm$^{-1}$, and the uncertainty of thermal stress is $\pm 13$ MPa. The thermal stress for the silicon under the glass fiber is higher than that under the silica particle at the same temperature-rise situation. The experimental wavenumber and linewidth in the fiber case vary more linearly with the laser energy than those in the particle case. These phenomena are owing to the diameter difference and focusing effect. When the size of the focusing element

is larger, the laser is less focused on the substrate. While changing the laser energy filter in the experiment, there is a little change in the optical alignment, as well as the laser focusing condition. The diameter of glass fiber (6.24 μm) is five time that of silica particle (1.21 μm). So the focusing effect in the glass fiber is smaller, and it is less sensitive to the alignment change and out-of-focus effect. For the fiber case, $\Delta\omega_{exp}$ and $\Delta\Gamma_{exp}$ vary more linearly with the laser energy and the changing trends of $\Delta\omega_{focus}$ and $\Delta\Gamma_{focus}$ are better than the particle case.

### 4.3. Physics Interpretation of Near-Field Focusing and Heating

To understand the mechanism of temperature and stress rise in the silicon substrate under near-field focusing, simulation is performed to obtain the optical, thermal, and stress information. The simulation process and results for the microparticle induced laser heating with the highest energy flux are outlined below. Optical field simulation for microparticle-induced laser focusing is conducted using the high frequency structure simulator (HFSS V14). The model consists of a silicon substrate ($\varepsilon = 17.22 + 0.428i$) and a quarter of a 1.21 μm silica particle ($\varepsilon = 2.13 + 0i$) in the air. Perfect *H* and Perfect *E* symmetry boundaries are set at symmetrical planes, and radiation boundaries are applied for the other boundary planes. A plane wave ($\lambda = 532$ nm) with an amplitude of 1 V/m is incident normally from the top. Other details of the optical field simulation can be found in Chap. 2 [95]. $I_{si} = 0.5c\varepsilon_0 nE^2$ is the intensity inside the silicon substrate, where $c = 3 \times 10^8$ m/s, $\varepsilon_0 = 8.854 \times 10^{-12}$ F/m, $n = 4.15$, and $E$ (V/m) the magnitude of the electric field. Figure 4.7 shows the light intensity distribution inside the silicon substrate. In the figure, $I_{si}/I_0$ indicates the optical intensity

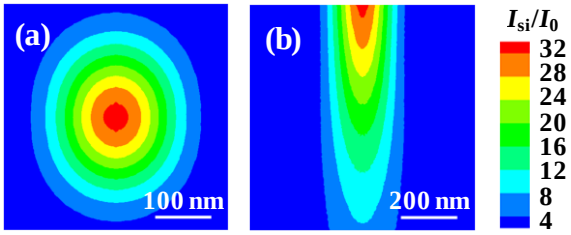


**Figure 4.7 Intensity of light distribution inside the silicon substrate. The amplitude indicates the optical intensity enhancement relative to the incident wave. (a) The top view of the substrate. (b) The vertical planes (side-view) in silicon under the particle center.**

enhancement in silicon relative to the incident wave. The photon energy is confined to a tiny region near the contacting point between the particle and the substrate with a radius of about 200 nm.

The temperature field distribution inside the silicon substrate is simulated using FLUENT V12. A quarter of cylinder model with a radius of 5 $\mu$m and a height of 10 $\mu$m is employed in the simulation. The top end surface of silicon is set as adiabatic. Both vertical cross-sections use symmetric boundary conditions. The peripheral and foot end surfaces of the domain and the initial temperature of the substrate are set at 300 K. The heat source is imported from the HFSS calculation results. The heat generation rate is $\dot{q} = I\beta$, where $I$ is the laser intensity, and $\beta$ is the absorption coefficient. Other details of the temperature simulation can be found in ref. [95]. Figure 4.8 shows the temperature distribution in the silicon substrate. The calculated maximum temperature rise inside the silicon is 51.0 K, agreeing well with the experimental result (58.5 K).

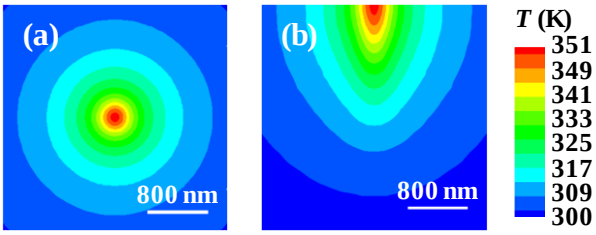


**Figure 4.8 Temperature distribution inside the silicon substrate. The initial temperature in silicon is 300 K. (a) The top view of the substrate. (b) The vertical planes (side-view) in silicon under the particle center.**

The thermal stress distribution inside the silicon substrate is simulated using ANSYS V14. The model as well as the temperature distribution is imported from the FLUENT calculation. The peripheral and foot end surfaces of the model are fixed. The top boundary is not constrained. Both vertical cross-sections are symmetric. The properties of silicon employed in both temperature and stress modeling are listed in Table 4.1 [97]. Figure 4.9 shows the thermal stress distribution in silicon. The maximum thermal stress observed in the simulation is 30 MPa, quite different from the experimental value of 160 MPa. There are four main factors that could lead to the differences between experiments and simulation. First, the incident laser employed in the optical field simulation is a uniform plane wave, while in the experiments the laser is focused by a 100× objective lens before it irradiates the sample. As a result, the focal size in the experiments could be smaller, and the temperature gradient is larger. Therefore, the thermal stress can be much higher than the simulation results. Second, the physical properties of silicon are assumed constant in the simulation. In fact, the properties vary with the temperature. The difference of properties in the temperature gradient regions would lead to a higher stress. Third, while calculating the experimental stress, the linewidth is assumed entirely stress independent. However, stress may have some effects on the linewidth [98]. Finally, the experimental relationship between wavenumber and linewidth

for out-of-focus status is achieved by moving pure silicon around the laser focal spot, which assumes that the out-of-focus status of silicon within the laser spot is all the same. However, while in the mapping and thermal probing experiments, both silicon signals from in-focus and out-of-focus statuses are collected, and only a small part of the sample is out of focus. In this case, the wavenumber and linewidth in the Gaussian function are actually summations of the two effects. These are different from the wavenumber and linewidth in the Gaussian function used in the relationship calibration, where only out-of-focus status is considered. It leads to some uncertainty in evaluating the out-of-focus effect, which could finally affect the stress calculation.

**Table 4.1 Physical properties of silicon wafer in the modeling**

| Density [$kg \cdot m^{-3}$] | Specific heat [$J \cdot Kg^{-1} \cdot K^{-1}$] | Thermal conductivity [$W \cdot m^{-1} \cdot K^{-1}$] | Young's modulus [GPa] | Thermal expansion coefficient [$K^{-1}$] | Poisson's ratio |
|---|---|---|---|---|---|
| 2329 | 705 | 148 | 117.4 | $2.62 \times 10^{-6}$ | 0.262 |

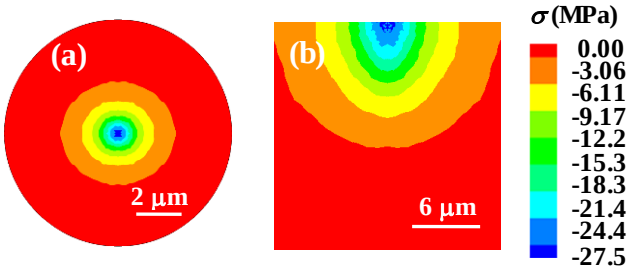


**Figure 4.9 The thermal stress distribution induced by temperature rise inside the silicon substrate. (a) The top view of the substrate. (b) The vertical planes (side-view) in silicon under the particle center.**

# CHAPTER 5. NANOSCALE WEAK CONTACT AT GRAPHENE/SUBSTRATE INTERFACES: UNCOVERED BY PHOTON EXCITATION AND PROBING

Previous work is focused on the Raman mapping and thermal probing of silicon under particles and fibers at the nanoscale. The resolution for thermal probing is about 200 nm in both horizontal and vertical directions, while for Raman mapping it is down to 20 nm in the horizontal direction. To explore the resolution limit in the vertical direction, the next work will move to the study of thermal characterization of graphene/substrate interfaces. As a two dimensional material, graphene exhibits great electronic quality, which gives the opportunity for broad potential applications in the future [42-45]. Its excellent thermophysical properties prompt potential applications in semiconductor devices [46, 52-54]. In its applications, a graphene sheet is often attached to a substrate. Heat dissipation in the in-plane direction would be greatly impeded due to the thin thickness of graphene (0.35 nm for a single layer). The thermal transport to the adjacent materials plays the major role in heat dissipation on graphene based electronic devices. Therefore, the knowledge of energy coupling at the interface is important to evaluate this out-of-plane heat dissipation. Very little research has been done on thermal transport at the interface of graphene/substrate [38, 55, 99].

In this chapter, the temperature difference of graphene and its substrate is distinguished and probed at the atomic level simultaneously using Raman spectroscopy while the graphene is under a second well-defined laser heating. The thermal contact resistances at CVD graphene/Si, CVD graphene/glass, and epitaxial graphene/SiC interfaces are evaluated with laser heating experiments and molecular dynamics simulations. Stress information of

graphene on substrate is obtained by comparison of Raman wavenumber and linewidth methods in temperature determination. The nanoscale weak contact between graphene and substrate under laser heating is characterized in four aspects: the anomalous interface resistance, comparison of linewidth and intensity methods, light interference theory, and AFM images.

## 5.1. Experimental Details

Figure 5.1 shows schematic of the experimental setup for interfacial energy coupling characterization between graphene and Si substrate. The substrate is Si, which the heating laser (1550 nm) cannot go through from its rough back surface. For transparent substrates like SiC and glass, a slightly different experiment is designed and will be detailed later. A single layer graphene (SLG) on silicon sample (ACS Material) is set on a 3-D nano-stage (MAX311D, Thorlabs). The piezoelectric actuator of the nano-stage is controlled in a feedback mode. The stability is significantly improved and the positioning resolution is down to 5 nm. The high resolution and stability of the stage reduces the possible noise to the Raman spectra to a great degree, which is critical to the success of our measurements. A probing laser ($\lambda$ = 532 nm) from a confocal Raman system irradiates the sample from the top. The Raman spectrometer (Voyage, B&W Tek) is confocal with a microscope (Olympus BX51). The spot size of the Raman laser focused through a $50\times$ objective lens is $2\times4$ $\mu m^2$, which is determined by using a blade method. The Raman laser power is small (6.9 mW) that the temperature rise induced by the Raman laser is negligible. Mainly, the sample is heated up by a second (heating) laser ($\lambda$ = 1550 nm) with a continuous energy power tuning up to 2 W. The laser propagation direction is $60^\circ$ to the vertical direction ($\alpha$ = $60^\circ$ as shown in

Figure 5.1) from above the sample, while the graphene is in the horizontal plane.

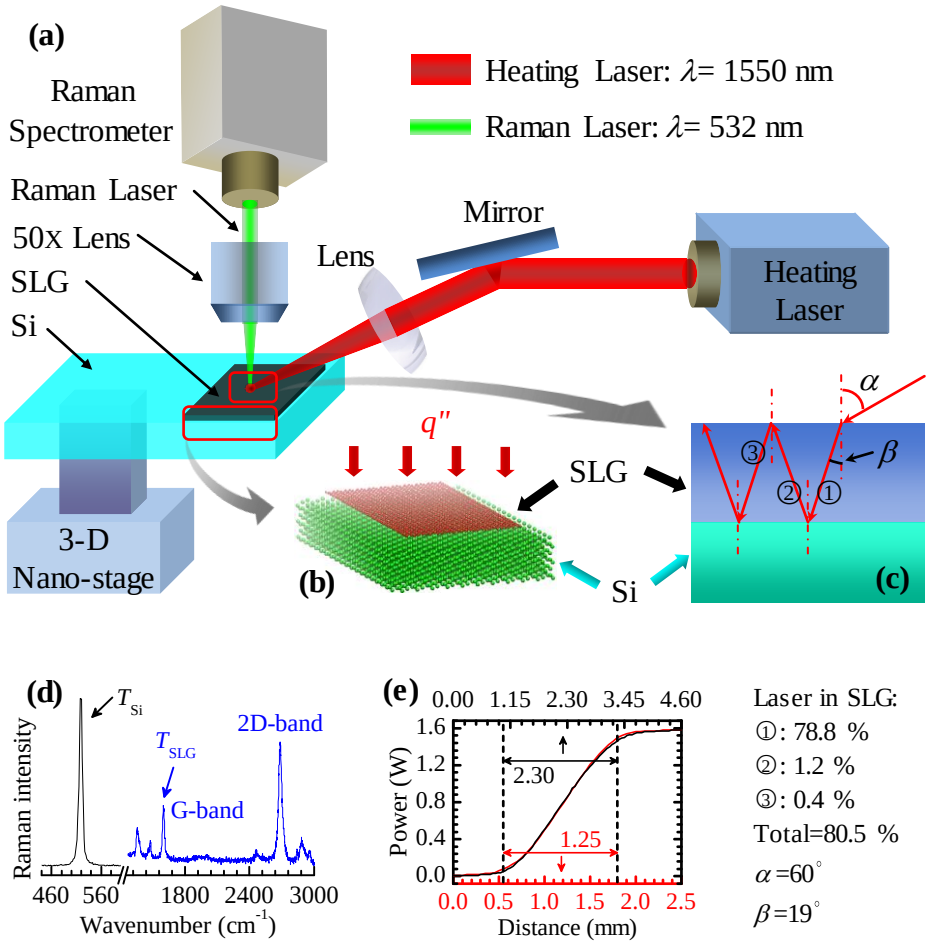


**Figure 5.1 Schematic of experimental setup for thermal characterization of SLG-Si interface. (a) A SLG-Si sample is heated up by a laser from above with an incident angle of 60°. Raman signals of SLG and Si are excited by a Raman laser and collected with a Raman spectrometer. The position of the sample is controlled by a 3-D nano-stage with a high resolution of 5 nm. (b) The graphene layer absorbs laser energy and dissipates heat to the Si substrate. (c) The laser propagation path and the accumulated energy passing the graphene. (d) Temperatures of both SLG and Si materials can be determined simultaneously by Raman spectrum. (e) The heating laser power is varied from 0.1-1.6 W and the spot size on the sample is $2.30 \times 1.25$ mm$^2$.**

The heating laser is focused by an optical lens before it reaches the sample, and the final focal spot size is $2.30 \times 1.25$ mm$^2$. Within the spot size, 90 % of the laser energy is covered. The light absorption in graphene can be calculated from Dirac fermions. For a single layer,

2.3 % of laser light is absorbed [100]. After reaching the surface of the graphene, the laser light is refracted and reflected multiple times at the air-SLG and SLG-Si interfaces. The refractive indices of SLG and Si are 2.69 and 3.47 respectively. About 1.85 % of the laser energy is absorbed in the graphene layer. The detailed path and absorbing percentage of the laser light is depicted in Figure 5.1. Little laser energy is absorbed in the silicon substrate. At $\lambda$ = 1550 nm, the heating photon energy is less than the bandgap of silicon, so the absorption in silicon is very small. The graphene layer is heated up by the heating laser and dissipates heat in three directions: one part crosses the plane to the interface, the second part dissipates along the graphene layer in the lateral direction, and the third part to the adjacent air via convection and radiation. In our experiment, the laser heating area is very large (1~2 mm) and the thermal probing area is very small (2~4 μm) and is in the middle of the heating region. Little temperature gradient exists in the in-plane direction in the μm central region. Heat is dissipated across the interface to the substrate. The temperature of the substrate would then increase. As the graphene layer is bonded with the substrate via van der Waals force (vdW), which is a loose contact, there would be large thermal contact resistance between them. To determine the thermal resistance across this weak contact, Raman spectra of graphene and silicon substrate are obtained during laser heating. The graphene is confirmed to be single layer according to the Raman intensity ratio of 2D peak and G peak shown in Figure 5.1 [101]. The Raman integration times for the silicon and graphene are 2 s and 40 s respectively. Based on the Raman signals of graphene and silicon, the temperatures of both layers are determined under different laser energies.

The Rama spectra are affected by factors including power of heating laser, focal level of

Raman laser, stability of sample and other related equipment factors. In the measurement, the focal level of Raman laser is first determined. When the Raman laser is focused on the graphene layer, the intensity of G peak is strong. A group of Raman spectra are obtained at several focal levels in the vertical direction. The background signal is subtracted to achieve sound Raman spectrum. The sample is fixed at the focal level that gives the highest graphene G peak intensity. While heating the sample, only the power of the heating laser is increased, no equipment is touched or changed. The effects of environmental changes are eliminated. It ensures the maximum measurement accuracy. In the measurement, the Raman laser also heats up the graphene and substrate. The heat induced by the Raman laser does not affect the results, however. First, all the results are obtained without changing the power of the Raman laser. The temperature rise changed observed versus the heating laser power variation is only induced by the heating laser while the effect of Raman laser is subtracted in the linear fitting process (detailed later). Second, the power of the Raman laser (6.9 mW) is much smaller than that of the heating laser (0.1-1.6 W). Thus, the temperature rise induced by the Raman laser is negligible.

## 5.2. Measurement of CVD Graphene on Si

### 5.2.1 Poor interface reflected by weak interfacial phonon coupling

Single layer graphene on silicon substrate (ACS Material) is used in the experiments. The graphene is fabricated on copper first by using the CVD method, and transferred to a silicon substrate. Raman intensity, wavenumber, and linewidth all can be employed to probe the temperature of materials. For graphene and silicon, the Raman intensity and wavenumber decrease, and linewidth broadens as their temperatures rise. Since linewidth is of closely

relevance with phonon lifetime, it is strongly affected by temperature with negligible effect from stress. Therefore, the linewidth method can be used to determine the temperature of both materials, and then to evaluate the thermal contact resistance. For wavenumber, previous research indicates that it is also dependent on the local stress in the materials. Therefore, the temperature based on wavenumber is different from that based on linewidth if a local stress exists. For Raman intensity, the light interference at the graphene-substrate interface (if local spacing exists) is an influence factor in addition to temperature. Interference at the interface enhances the Raman intensity.

The temperature coefficients of graphene and silicon Raman spectrum need to be calibrated in order to determine the local temperature during experiment. The G peak (~1580 $cm^{-1}$) of graphene is employed for temperature determination. The Raman spectrum of graphene is fitted with a Lorentz function to determine precise Raman parameters. The Raman peak (~518 $cm^{-1}$) of silicon is used for temperature determination. The calibration results for linewidth against are shown in the inset of Figure 5.2. The relationship between temperature and linewidth can be treated as linear within a small temperature range. The temperature coefficients of SLG and Si for linewidth are determined as 0.0255 and 0.00913 $cm^{-1}/K$ respectively in a range from room temperature to 180 °C. Yue *et al.* obtained a temperature coefficient of tri-layer graphene as 0.0127 $cm^{-1}/K$ [38]. The temperature of coefficient varies with the number of graphene. Tang *et al.* measured the temperature coefficient of Si and obtained a slope of 0.0082 $cm^{-1}/K$ [95, 102]. The work by Bauer *et al.* obtained a slope for temperature against linewidth as 0.01 $cm^{-1}/K$ [40]. Therefore, our

calibration results are in good agreement with the literature, considering the variation of experimental environments and samples.

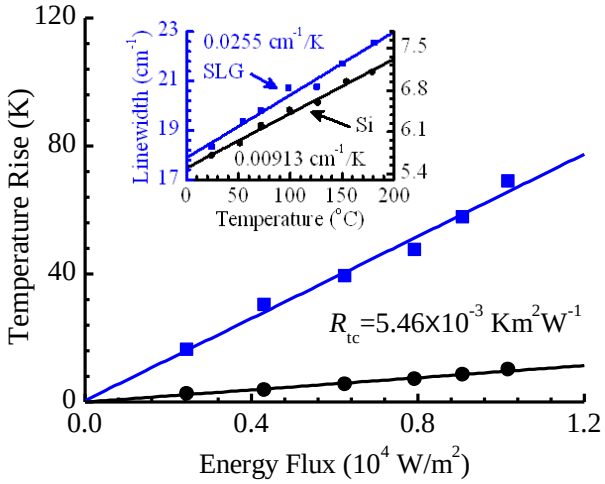


**Figure 5.2 Experimental results of interfacial thermal resistance ($R_{tc}$) at SLG-Si interface. $R_{tc}$ is determined as $5.46\times10^{-3}$ K·m$^2$·W$^{-1}$ according to linewidth broadening. The inset shows the calibration results of the temperature dependence of linewidth for Si and G-band of SLG.**

The thermal resistance at the SLG-Si interface is determined as $R_{tc} = (T_{SLG} - T_{Si})/q"$, where $T_{SLG}$ and $T_{Si}$ are temperatures of SLG and Si, and $q"$ the heat flux. Since the determination of resistance from a single point is of high uncertainty, six laser energy fluxes are used in the experiments to improve the accuracy. The temperature rise in Figure 5.2 is the value relative to room temperature. The effect of the Raman laser heating is subtracted since the Raman spectrum with Raman laser heating is used as the base to evaluate the linewidth change when the heating laser is applied. The temperature rise has a positive linear relationship with the energy flux. The fitted slopes for SLG and Si are $6.41 \times 10^{-3}$ and $9.50 \times 10^{-4}$ Km$^2$W$^{-1}$ respectively. Then the interfacial resistance can be calculated as $R_{tc} = (T'_{SLG} - T'_{Si})$, where $T'_{SLG}$ and $T'_{Si}$ are fitting slopes of temperature against heat flux for

SLG and Si respectively. For SLG-Si interface, the thermal resistance is determined as $5.46 \times 10^{-3}$ $Km^2W^{-1}$. The uncertainty of thermal resistance measurement can be analyzed according to the standard error of the linear fitting, which is $2.9 \times 10^{-4}$ $Km^2W^{-1}$. In the measurement, the temperature of Si is an average temperature within the skin depth of the Raman probing laser. It is not the temperature immediately next to the surface of Si. The skin depth of the Raman laser in silicon is $\tau = \lambda / (4\pi\kappa)$, where $\lambda$ is the wavelength of the laser and $\kappa$ is the extinction coefficient. At $\lambda = 532$ nm, $\kappa = 0.0516$ for silicon, and then $\tau = 820$ nm. The thermal conductivity of Si is $k$ = 148 $Wm^{-1}K^{-1}$. As the laser is focused on the surface of Si, the measured temperature of Si can be estimated at the half skin depth. Thus the heat conduction resistance within the Si is evaluated as $5.54 \times 10^{-9}$ $Km^2W^{-1}$. The thermal resistance in Si is much smaller than the measured interfacial thermal resistance of $5.46 \times 10^{-3}$ $Km^2W^{-1}$. The little thermal resistance of Si region has negligible effect on the total interface thermal resistance.

The measured thermal resistance at the SLG-Si interface is extremely large. For a normal full-contact interface with van der Waals force bond, a thermal resistance in the order of $10^{-8}$ $Km^2W^{-1}$ is expected. Our measured thermal resistance indicates very poor localized energy coupling. We speculate that a lot of areas at the graphene/Si substrate have poor contact, like some separation exists. To further elucidate the interfacial thermal resistance changes against the separation distance, molecular dynamics (MD) simulation is carried out. A silicon layer with dimensions of 5.8×20.0×5.4 $nm^3$ ($x$×$y$×$z$) is built and the supported graphene nanoribbon (GNR) is 4.1×18.3 $nm^2$ ($x$×$y$). The second generation of Brenner potential [103], reactive empirical bond-order (REBO), based on the Tersoff potential [104, 105] with interactions

between C-C bonds is employed to model the graphene system. It has been proposed that the interactions between carbon atoms and the substrate are primarily short-range van der Waals type (vdW) [106, 107]. Therefore, the C-Si couplings is modeled as vdW interactions using the Lennard-Jones (LJ) potential $V(r) = 4\varepsilon[(\sigma/r)^{12} - (\sigma/r)^{6}]$, where $\sigma$ is the distance parameter, $\varepsilon$ is the energy parameter and $r$ the interatomic distance. In this work, $\varepsilon$ and $\sigma$ are set as 8.909 meV and 0.3326 nm respectively [108]. The LJ potential is truncated at a cut-off distance of $r_c$ = 3.5$\sigma$. The step for time integration is 0.5 fs (1 fs = $10^{-15}$ s). All MD simulations are performed using the large-scale atomic/molecular massively parallel simulator (LAMMPS) package [109]. Periodic boundary conditions are applied to the $x$ and $y$ directions (lateral direction) and free boundary condition to the $z$ direction. The bottom layer of silicon substrate is fixed in position to avoid any vertical movement of the system. The two boundary layers of graphene in the $y$ direction are fixed to maintain the distance between graphene and Si substrate. Four cases with separation distances ($\delta$) of 0.4, 0.6, 0.65 and 0.7 nm are calculated and the thermal resistance results are shown in Figure 5.3. Take the 0.4 nm case as an example, after 300 ps canonical ensemble (NVT) and 100 ps microcanonical ensemble (NVE) calculations, the system reaches thermal equilibrium at temperature 300 K. Then a thermal impulse with $q_{in}$ equals $6.04\times10^{-4}$ W is added to the graphene system for 50 fs. After 150 ps thermal relaxation process, the thermal resistance is calculated at $7.31\times10^{-8}$ $Km^2W^{-1}$ by fitting the thermal relaxation process of graphene using this equation: $E_t = E_0 + (R/A)\cdot\int_0^t (T_{GNR} - T_{Si})dt$. Here $A$ is the graphene area, $E$ graphene energy, and $R$ the interfacial thermal resistance. As described by the LJ potential, when the separation distance between graphene and Si substrate increases, the interatomic forces between these two

materials decrease quickly. As a result, the thermal energy transport from graphene to Si system becomes slower and eventually leads to a larger thermal resistance value. For $\delta$ equals 0.6, 0.65, and 0.7 nm, the interfacial thermal resistance are $2.25\times10^{-7}$, $1.37\times10^{-6}$, and $4.53\times10^{-5}$ $Km^2W^{-1}$, respectively. Such results strongly demonstrate that the interfacial thermal resistance increase rapidly with the separation distance. We expect in many areas the distance between SLG and Si will be beyond Waals force interaction, resulting in a local high thermal resistance. The measured thermal resistance is an average over the whole probed region: tight contact and loose contact regions. In another word, many ripples exist in the SLG, leading to a rough contact with the Si substrate. Such loose contact will give the graphene a lot of flexibility to thermally expand/contract without inducing strong stress in graphene. This point is analyzed below in detail.

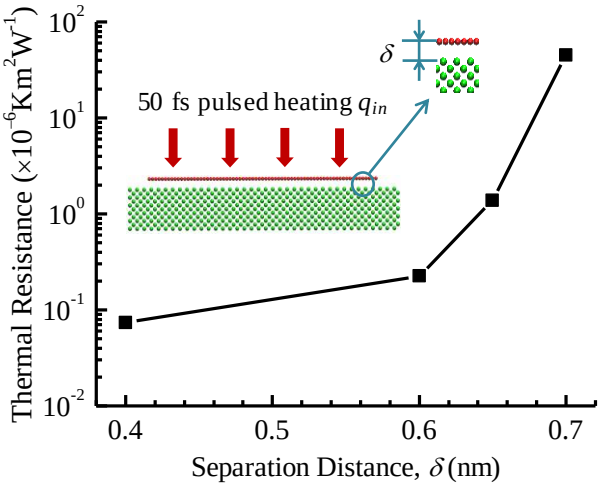


**Figure 5.3 Variation of interfacial thermal resistance with separation distance $\delta$ based on MD simulation. Atomic configuration of the system is shown in the inset. The thermal resistance increases rapidly with $\delta$ and reach a magnitude of $10^{-5}$ $Km^2W^{-1}$ when $\delta$ = 0.7 nm.**

5.2.2 Poor interface coupling revealed by negligible stress in graphene upon laser heating

To verify the rough contact at the SLG-Si interface, the wavenumber method is employed to evaluate the temperature. As mentioned above, the wavenumber is related to both temperature and thermal stress, and it is more sensitive to temperature than linewidth. Thermal stress can be reflected based on the difference between wavenumber temperature and linewidth temperature. Thermal expansion of SLG and Si should be considered in explaining the thermal stress. The thermal expansion coefficient of graphene was reported in a range from negative values to $1 \times 10^{-5}$ $K^{-1}$ [110]. At room temperature, the thermal expansion coefficient of Si is about $2.6 \times 10^{-6}$ $K^{-1}$ [111]. There is a significant difference between thermal expansion coefficients of graphene and Si. During laser heating, the degrees of expansion of graphene and Si are different. If perfect bonding exists between them, then a large thermal stresses would arise due to the mismatch in thermal expansion. Otherwise, a loose contact would lead to small stress.

The relationships of wavenumber temperature rise against heat flux for graphene and silicon are depicted in Figure 5.4 along with their temperature coefficients of wavenumber. The wavenumber decreases with slopes of -0.0240 and -0.0201 $cm^{-1}/K$ for G-band of SLG and Si respectively. Yue *et al.* obtained a temperature coefficient of -0.025 $cm^{-1}/K$ for triple layer graphene (TLG) [38]. Others' work reported the slope of temperature against wavenumber in a range from -0.015 to -0.038 $cm^{-1}/K$ for single and bilayer graphene [112-114]. The temperature coefficient varies with the number of graphene layers, the wavelength of probing lasers, and the temperature range in the calibration. Calizo *et al.* pointed out that the temperature coefficient decreases with the number of layers [113]. The linear fitting slope

of wavenumber against temperature for Si was reported as -0.022 $cm^{-1}/K$ [39, 95]. Therefore, the calibration results agree well with literature values.

With the knowledge of temperature coefficients against wavenumber for both SLG and Si, the relationships of temperature rise and laser heating flux are obtained. Figure 5.4 shows the slopes for SLG and Si as $6.74\times10^{-3}$ and $8.40\times10^{-4}$ $Km^2W^{-1}$ respectively. Their difference gives an interfacial thermal resistance for SLG-Si as $5.90\times10^{-4}$ $Km^2W^{-1}$ based on wavenumber, with an uncertainty of $2.84\times10^{-4}$ $Km^2W^{-1}$. This result is very close to the linewidth-method value of $5.46\times10^{-4}$ $Km^2W^{-1}$. The similar results strongly conclude that the thermal stress in the sample is not significant. It points out that the graphene placed on the Si substrate is very loose and flexible. Graphene expands freely above the Si surface to a large degree during laser heating. The contacting area between graphene and Si only counts a small part of the total graphene area. We feel confident the separation of graphene and Si substrate is the main factor causing the large thermal contact resistance at the interface.

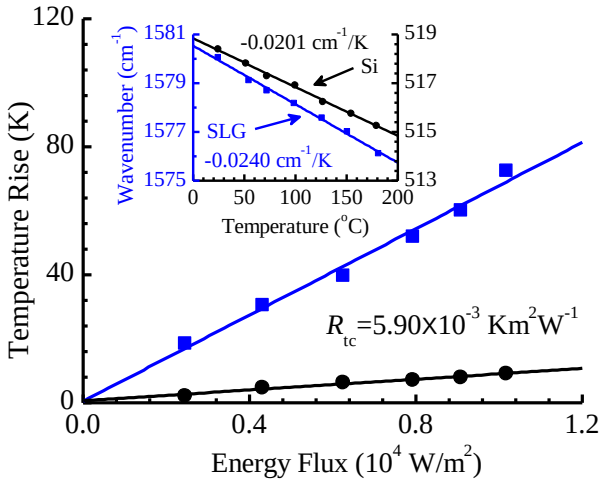


**Figure 5.4 Interfacial thermal resistance at SLG-Si interface obtained by wavenumber softening. The inset shows the fitting slopes of wavenumber against temperature for SLG and Si.**

5.2.3 SLG/Si separation revealed by Raman variation and AFM surface morphology

Raman intensity is further processed to explain the rough contact between SLG and Si. More importantly, with the help of laser light interference between SLG and Si, it can, for the first time, determine the mismatch distance of these two layers using Raman intensity. It has been proved that Raman intensity drops with the increase of temperature. High temperature has an effect on the band structure, which imposes restrictions on the photon interactions necessary to produce Raman scattering signals. Usage of absolute intensity difference is hard to determine the temperature rise, as intensity is sensitive to environmental factors, focal level of probing laser, and change of Raman system. To improve the measurement accuracy, normalized intensity is employed to determine temperature. Raman intensities of SLG and Si are calibrated at temperatures from 25 to 180 ˚C. Extrapolation is carried out to get the intensity value at 0 ˚C. The normalized intensity is the intensity at a certain temperature to that at 0 ˚C. The inset in Figure 5.5 shows that the normalized intensity decreases with

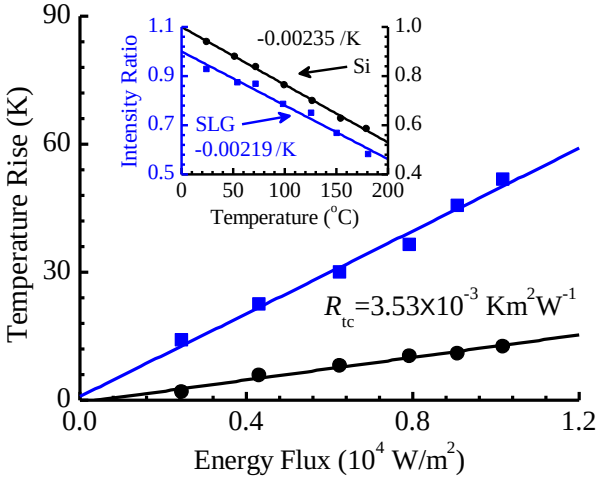


**Figure 5.5 Interfacial thermal resistance at SLG-Si interface obtained by intensity decreasing. The inset shows the fitting slopes of normalized intensity against temperature for SLG and Si.**

temperature. The fitting slopes for G-band of SLG and Si are -0.00219 and -0.00235 /K respectively. The coefficient of normalized intensity against temperature for Si is reported as -0.00249 $K^{-1}$ [102, 115]. To our best knowledge, no literature has reported the temperature coefficient for normalized intensity of graphene.

The slopes for temperature rise of SLG and Si with energy flux are 4.85 $\times 10^{-3}$ $Km^2W^{-1}$ and 1.32 $\times 10^{-3}$ $Km^2W^{-1}$ respectively. The thermal contact resistance based on intensity is determined as $3.53 \times 10^{-3}$ $Km^2W^{-1}$, as shown in Figure 5.5, with an uncertainty of $2.02 \times 10^{-4}$ $Km^2W^{-1}$. The thermal contact resistance obtained based on the Raman intensity is smaller than that based on linewidth and wavenumber. There are three factors combined together leading to the difference: deviated thermal expansion conditions for experiment and calibration, the air layer between SiC and Si, and light interference at the interface. The thermal expansion of SLG and Si should be first considered in explaining the intensity difference. The thermal expansion coefficient of graphene was reported in a range from negative values to $1 \times 10^{-5}$ $K^{-1}$ [110]. At room temperature, the thermal expansion coefficient of Si is about $2.6 \times 10^{-6}$ $K^{-1}$ [111]. There is a significant difference between thermal expansion coefficients of graphene and Si. In addition, the thermal expansion conditions for experiment and calibration are different, as shown in Figure 5.6. We take a case of graphene at 90 ˚C for the analysis. In the calibration, the sample is heated up by a round heater which is glued under Si with silver paste. The temperatures of SLG and Si are the same and uniformly distributed within the Raman probing area (~8 $\mu m^2$). In calibration, the distance between SLG and Si is $\delta_{cal}$, and the probed intensity is $I_{cal}$. In the laser heating experiment, the temperature distribution is different. Assume the temperature of SLG reaches the same level:

90 °C, the temperature of Si would be around 30 °C according to linewidth method. Si shrinks relative to the temperature of 90 °C scenario in the calibration. Consequently, the height of the ripple of SLG on Si is enlarged, which means $\delta_{\text{exp}} > \delta_{\text{cal}}$, and $I_{\text{exp}} > I_{\text{cal}}$. The Raman intensity enhancement factor ($F$) increases with the thickness ($\delta$) of the separation between SLG and Si if $\delta$ is not too large. The incident laser passes through the graphene flake since it only has one atomic layer. Raman scattering signal is generated because of the excitation of the incident laser. Both incident and Raman scattering lights are reflected multiple times on the SLG-air and air-Si interfaces. The interference effect of the Raman scattering signals enhances the Raman intensity. Considering the absorption and scattering of each layer, the normalized enhancement factor is calculated with optical constants of all layers according to literatures [116, 117]. The net absorption term ($F_{\text{ab}}$) is expressed as

$$F_{\text{ab}} = t_1 \frac{(1 + r_2 r_3 e^{-2i\beta_2}) e^{-i\beta_x} + (r_2 + r_3 e^{-2i\beta_2}) e^{-i(2\beta_1 - \beta_x)}}{1 + r_2 r_3 e^{-2i\beta_2} + (r_2 + r_3 e^{-2i\beta_2}) r_1 e^{-2i\beta_1}} \tag{5-1}$$

where $t_1 = 2n_0 / (n_0 + \tilde{n}_1)$ , $r_1 = (n_0 - \tilde{n}_1) / (n_0 + \tilde{n}_1)$ , $r_2 = (\tilde{n}_1 - \tilde{n}_2) / (\tilde{n}_1 + \tilde{n}_2)$ , and $r_3 = (\tilde{n}_2 - \tilde{n}_3) / (\tilde{n}_2 + \tilde{n}_3)$ are the Fresnel transmittance and reflection coefficients for the interfaces involving air (0), SLG (1), air (2), and Si (3). $n_0$, $\tilde{n}_1$, $\tilde{n}_2$, and $\tilde{n}_3$ are the refractive indices for air, SLG, air, and Si, respectively. $\beta_x = 2\pi x \tilde{n}_1 / \lambda$ , $\beta_1 = 2\pi d_1 \tilde{n}_1 / \lambda$ , and $\beta_2 = 2\pi d_2 \tilde{n}_2 / \lambda$, $x$ is the depth of the point where the interaction occurs, $\lambda$ is the wavelength of incident laser, and $d_1$ and $d_2$ are the thickness of graphene layer and the in-between air layer, respectively. The net scattering term ($F_{\text{sc}}$) is described as

$$F_{\text{sc}} = t_1' \frac{(1 + r_2 r_3 e^{-2i\beta_2}) e^{-i\beta_x} + (r_2 + r_3 e^{-2i\beta_2}) e^{-i(2\beta_1 - \beta_x)}}{1 + r_2 r_3 e^{-2i\beta_2} + (r_2 + r_3 e^{-2i\beta_2}) r_1 e^{-2i\beta_1}} \tag{5-2}$$

where $t_1^{'} = 2\tilde{n}_1 / (\tilde{n}_1 + n_0)$ and $\lambda$ is the wavelength of the G band of graphene. Thus, the total enhancement factor ($F$) is given by

$$F = N\int_0^{d_1} | F_{ab} F_{sc} |^2 \mathrm{d}x \tag{5-3}$$

where $N$ is a normalized factor, which is a reciprocal number of the total enhancement factor for a SLG layer on a Si substrate without the air layer between them, obtained by setting the thickness of the in-between air layer to be 0. In the calculation, the refractive index of graphene is $2.6-1.3i$. The refractive indices of Si are $4.15+0.05i$ and $3.99+0.03i$ for incident laser and Raman scattering respectively. Figure 5.6 shows how the enhancement factor varies against the separation distance. When $\delta$ increases to 8 nm, $F$ enhances exponentially to over 1.2.

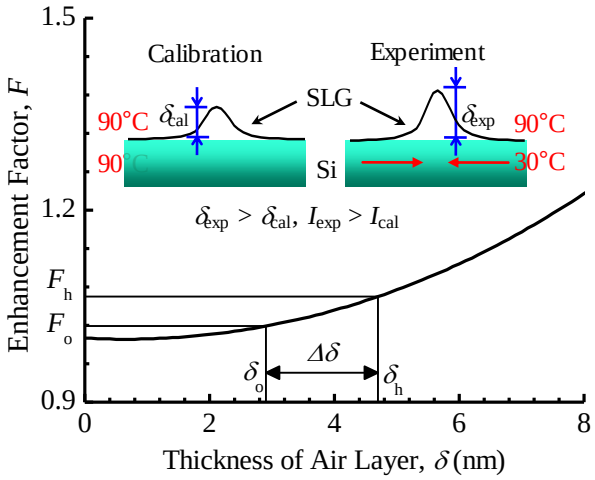


**Figure 5.6 Raman intensity enhancement factor $F$ of SLG increases with the thickness of air layer $\delta$. The inset delineates that $\delta_{exp}$ is larger than $\delta_{cal}$ due to the thermal expansion mismatch of SLG and Si in the experiment.**

According to the Raman intensity enhancement in the experiment, the thickness increment of air layer at the SLG-Si interface after laser heating can be calculated. The

temperature rises based on the intensity method ( $\Delta T_I$ ) and the linewidth method $\Delta T_\Gamma$ are described as the following equations:

$$\Delta T_I = (1 - I_{\exp} / I_0) / \chi_I \tag{5-4}$$

$$\Delta T_\Gamma = (1 - I_\Gamma / I_0) / \chi_I \tag{5-5}$$

where $I_{\exp}$ is collected Raman intensity during laser heating, $I_0$ is the intensity at room temperature, $\chi_I$ is the temperature coefficient of intensity, and $I_\Gamma$ the predicted intensity without extra enhancement. Due to the intensity enhancement, $I_{\exp}$ is higher than $I_\Gamma$, and their relationship is:

$$I_{\exp} = F I_\Gamma \tag{5-6}$$

where $F$ is the enhancement factor. From the above results, while the absorbed energy flux in SLG is $1.0 \times 10^4$ $\mathrm{Wm^{-2}}$, $\Delta T_I = 51.8$ K, $\Delta T_\Gamma = 69.1$ K, and $\chi_I = -0.00219$ /K. By solving the above equations, the enhancement factor for laser heating is determined as $F = 1.045$. Assume the original distance between SLG and Si is $\delta_o = 2.9$ nm, which will be demonstrated by AFM results later, the original enhancement would be $F_o = 1.019$. After intensity enhancement by laser heating, the final enhancement factor is $F_h = F_o F = 1.065$. The final separation distance is $\delta_h = 4.7$ nm after laser heating. The separation increment of air layer is then obtained as $\Delta\delta = \delta_h - \delta_o = 1.8$ nm according to Figure 5.6. The AFM images in Figure 5.7 show the height of surface variations for the SLG-Si and pure Si samples. Only a small portion of the SLG is in contact with the Si substrate. Ripples of SLG can be found in the image. The height of the red line in the SLG image varies from 2.1 to 10.8 nm, an

average height of 2.9 nm. For the AFM images for pure Si, the height variation is mainly concentrated in a range from 0.7-1.3 nm, with an average height of 0.3 nm. The calculated thickness increment of air layer at the SLG-Si interface (1.8 nm) after laser heating is reasonable according to the AFM results. The MD simulation gives an interfacial thermal resistance from $7.31\times10^{-8}$ to $4.53\times10^{-5}$ $K\cdot m^2\cdot W^{-1}$ while the separation distance increases from 0.4 to 0.7 nm. Based on the surface morphology revealed in Figure 5.7, we can conclude that only a small portion of the graphene has sound contact and phonon coupling with the substrate, while large areas are separated from the Si surface.

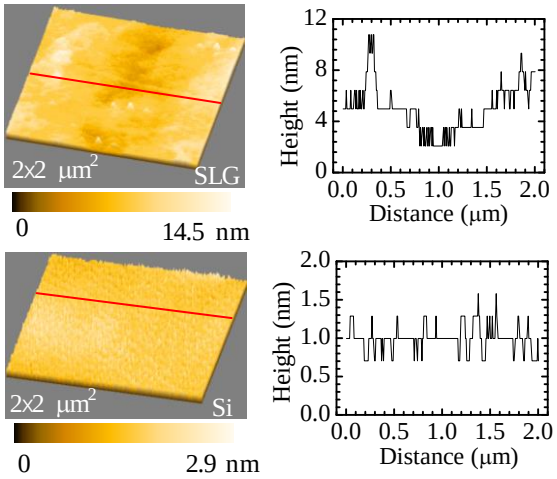


**Figure 5.7 AFM images of SLG on Si sample (upper) and pure Si (lower). The right two figures show the height variations of the Red lines in the left figures. The ranges of height variations are 8.7 and 0.5 nm for SLG-Si and pure Si respectively.**

From the above discussions, we conclude with great confidence that the contact between CVD graphene and Si substrate is poor. A separation layer exists at the interface with an increase during laser heating. The rough contact can be explained by the preparation method of the SLG-Si sample. In synthesis, copper foil based monolayer graphene was first prepared by the CVD method. PMMA was then deposited on the graphene layer and cured. An etching

process was taken to remove the copper foil. PMMA-SLG was washed in water and deposited onto Si substrate. After curing, PMMA was removed with acetone from the graphene layer. During this process, some residual atoms might stay between SLG and Si, which would reduce their contact significantly. As the contact is loose, during laser heating, little stress rises and ripples emerge strongly in the graphene layer.

### 5.3. Interface between Epitaxial Graphene and SiC

In this section, the rough contact and phonon coupling across epitaxial graphene-SiC interface is investigated. The graphene-SiC sample is obtained from Graphene Works. Epitaxial graphene is grown on the C-face of 4H-SiC by heating the sample up to 1300 °C in vacuum. Uniform triple layer graphene can be found on the SiC substrate. The experimental setup for the thermal resistance measurement of TLG-SiC interface, as shown in Figure 5.8, is similar to that for the SLG-Si interface. The difference lies in the propagation direction of the heating laser. In this experiment, the laser irradiates from under the TLG-SiC sample with an angle of 60° to the vertical direction. About 80 % of the laser energy passes through the SiC layer and reaches the TLG layer. A tri-layer graphene absorbs 6.9 % of the laser energy that passing through it [100]. After multiple times of reflection and absorption, the TLG layer absorbs 6.98 % of the incident laser energy. The detailed laser light path and energy absorption percentage in the TLG layer is delineated in Figure 5.8. The refractive indices for TLG and SiC are 2.27 and 2.56 respectively. At $\lambda$ = 1550 nm, the heating photon energy is less than the bandgap of SiC, so little energy absorption occurs in the SiC layer. The graphene layer is heated up by the heating laser and dissipates heat crosses the interface to

the SiC substrate. To determine the thermal contact resistance across the TLG-SiC interface, Raman spectra of both materials are obtained. The graphene layer is confirmed to be triple-layered according to the Raman intensity ratio of 2D peak to G peak, as shown in Figure 5.8 [101]. The Raman integration times for the SiC and TLG are 4 s and 40 s respectively. The $E_2$ peak (~775 $cm^{-1}$) of SiC is chosen for temperature determination due to its high intensity. The second order $E_2$ mode of SiC is weak and partly overlaps with the G-band of graphene. Double peak fitting is used to resolve the G peak of graphene from the second order $E_2$ peak of SiC. Based on the Raman spectra, the temperatures of both TLG and SiC layers are obtained under different laser energies.

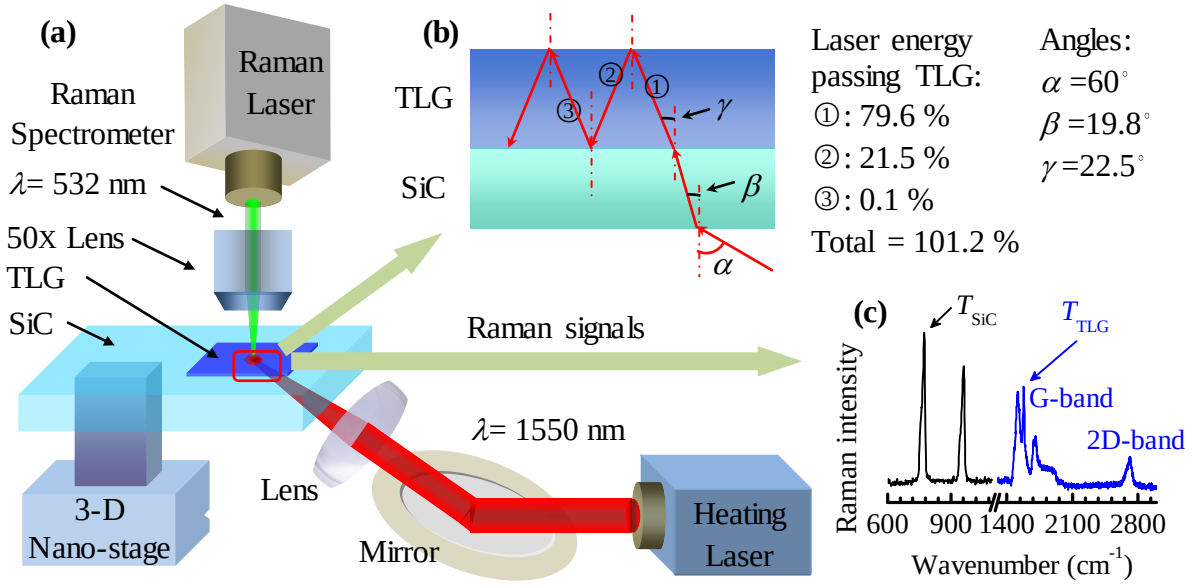


**Figure 5.8 Schematic of experimental setup for thermal characterization of TLG-SiC interface. (a) A TLG-SiC sample is heated up by a laser from below with an incident angle of 60°. (b) The laser propagation path and the accumulated energy passing the graphene. (c) Raman spectra for both TLG and SiC layers. Their temperatures can be determined simultaneously by Raman thermometry.**

Linewidth broadening is first employed to determine the thermal contact resistance at the TLG-SiC interface. The temperature coefficients of TLG and SiC for linewidth are calibrated as 0.0187 and 0.0141 $cm^{-1}/K$ respectively from room temperature to 180 °C, as shown in Figure 5.9(a). Yue *et al.* obtained fitting slopes for TLG and SiC as 0.0127 and 0.0087 $cm^{-1}/K$ respectively [38]. The temperature of sample rises as the laser energy flux increases. The fitted slopes of temperature rise against heat flux for TLG and SiC are $2.57 \times 10^{-3}$ and $3.00 \times 10^{-4}$ $Km^2W^{-1}$ respectively. The thermal resistance at the TLG-SiC interface is calculated as $2.27 \times 10^{-3}$ $Km^2W^{-1}$, with an uncertainty of $7.9 \times 10^{-5}$ $Km^2W^{-1}$. In the measurement, the temperature of SiC is an average temperature within the skin depth of the Raman probing laser, which is not the surface temperature. At $\lambda = 532$ nm, $\kappa = 0.001$ for SiC. Then skin depth $\tau = 42$ μm. The thermal conductivity of 4H-SiC is 390 $Wm^{-1}K^{-1}$. The heat conduction resistance within the SiC is $5.38 \times 10^{-8}$ $Km^2W^{-1}$, which is estimated at half of the skin depth. The thermal conduction resistance in SiC is much smaller than the measured interfacial thermal resistance of $2.27 \times 10^{-3}$ $Km^2W^{-1}$. The effect of thermal resistance of SiC region is negligible to the total interface thermal resistance. In the work by Yue *et al.*, the thermal contact resistance is reported as $5.30 \times 10^{-5}$ $Km^2W^{-1}$ [38], which is much lower than our measurement result. The difference could be attributed to sample to sample difference, and effect of different heating conditions. MD simulation in ref. [38] reported a TLG-SiC thermal resistance as $7.01 \times 10^{-10}$ $Km^2W^{-1}$. The simulation result is much lower than our measurement value. A detailed discussion is provided in the following to interpret the difference.

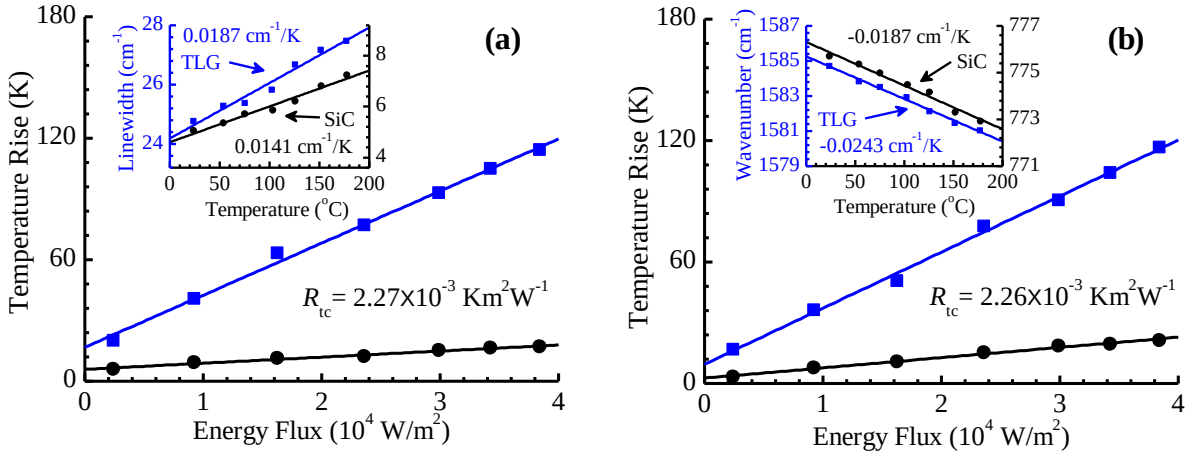


**Figure 5.9 Experimental results of interfacial thermal resistance ($R_{tc}$) at TLG-SiC interface. (a) $R_{tc}$ is determined as $2.27\times10^{-3}$ according to linewidth broadening. The inset shows the temperature dependence of linewidth for TLG and SiC. (b) $R_{tc}$ based on wavenumber softening. The inset shows the temperature dependence of wavenumber for TLG and SiC respectively. —■—: TLG; —●—: SiC.**

The thermal contact resistance is obtained by using the wavenumber method to prove the loose contact and high thermal resistance at the TLG-SiC interface. Figure 5.9(b) shows temperature coefficients of wavenumber for TLG and SiC. Wavenumber decreases with slopes of -0.0243 and -0.0187 cm$^{-1}$/K for G-band of TLG and SiC respectively. The fitting slopes of temperature rise against heat flux for TLG and SiC are $2.77\times10^{-3}$ and $5.05\times10^{-4}$ Km$^2$W$^{-1}$ respectively. Thus, the interfacial thermal resistance at TLG-SiC interface is determined as $2.26\times10^{-3}$ Km$^2$W$^{-1}$ based on wavenumber, with an uncertainty of $7.21\times10^{-5}$ Km$^2$W$^{-1}$. This result is nearly the same with the thermal resistance obtained by the linewidth-method ($2.27\times10^{-3}$ Km$^2$W$^{-1}$). Therefore, it is conclusive that the graphene experiences little stress during laser heating, and poor contact exists at the TLG-SiC interface. Graphene can expand on the SiC surface with large degree of freedom during laser heating. The TLG layer on the SiC substrate is very loose. The separation of TLG and SiC causes large thermal contact resistance at the interface.

Raman intensities of TLG and SiC are analyzed to explain the roughness of the sample and the thickness of air layer between TLG and SiC layers. In the calibration, Raman intensities are obtained at temperatures from 25 to 180 °C. Extrapolation is carried out to get the intensities for TLG and SiC at 0 °C. Normalized intensity, which is the ratio of the intensity at a certain temperature to that at 0 °C, decreases as the temperature increases. The inset in Figure 5.10(a) shows fitting slopes for G-band of TLG and $E_2$ mode of SiC as -0.00131 and -0.00237 $K^{-1}$ respectively. The slopes for temperature rise of TLG and SiC with heat flux are $2.06 \times 10^{-3}$ $Km^2W^{-1}$ and $6.43 \times 10^{-4}$ $Km^2W^{-1}$ respectively. The interfacial thermal resistance based on Raman intensity is determined as $1.42 \times 10^{-3}$ $Km^2W^{-1}$ with an

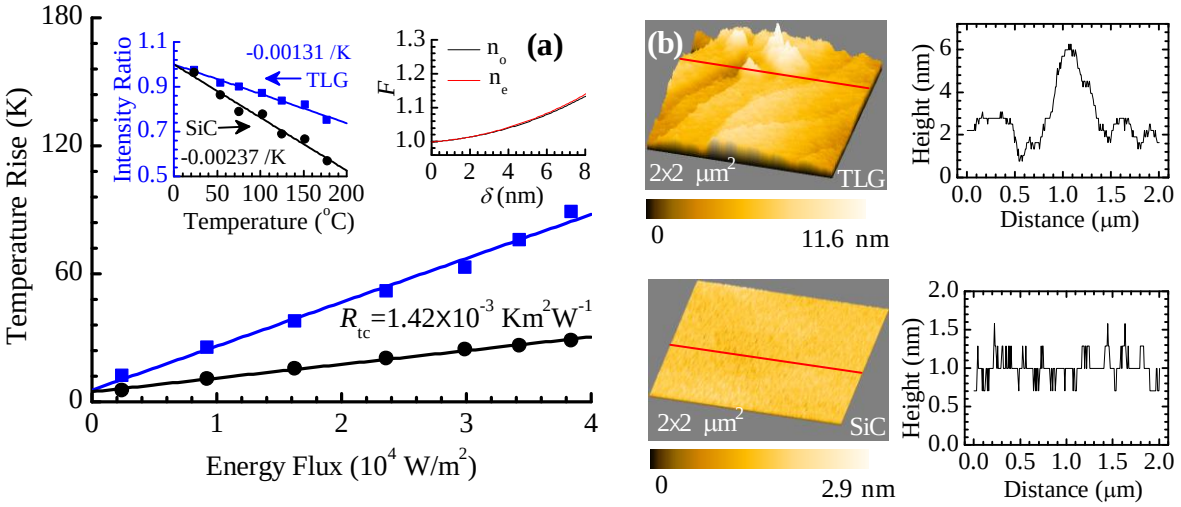


**Figure 5.10 Experimental results of interfacial thermal resistance and rough contact at TLG-SiC interface. (a) Interfacial thermal resistances are determined as $1.42\times10^{-3}$ $Km^2W^{-1}$ according to intensity variation. The left inset shows the temperature dependence of intensity for TLG and SiC respectively. The relationship of intensity enhancement factor ($F$) and the thickness of air layer $\delta$ between TLG and SiC is shown in the right inset. (b) AFM images of TLG on SiC sample (top left) and pure SiC (bottom left). The right two figures show the height variations of the Red lines in AFM images. The variation ranges of height are 5.5 and 0.5 nm for TLG-SiC and pure Si samples respectively. —■—: TLG; —●—: SiC.**

uncertainty of $9.32\times10^{-5}$ $Km^2W^{-1}$. This result is smaller than the results based on linewidth and wavenumber methods. Like the SLG-Si interface, here three factors leading to the difference: various thermal expansion conditions for experiment and calibration, the air layer between SiC and Si, and light interference at the interface. The thermal expansion coefficient of graphene was reported in a range from negative values to $1\times10^{-5}$ $K^{-1}$, while the coefficient of SiC is about $4.5\times10^{-6}$ $K^{-1}$ [110, 118]. The difference between them causes mismatch during laser heating. In addition, the thermal expansion conditions for experiment and calibration are different as discussed in the above section. The mismatch distance between the TLG on SiC is increased during laser heating experiment. The interference effect of the Raman scattering signals at the interface enhances the Raman intensity. The normalized enhancement factor ($F$) increases exponentially with the thickness ($\delta$) of the air layer between TLG and SiC, as shown in Figure 5.10(a) [116, 117]. When a nonpolarized light enters SiC at a nonzero acute angle to the optical axis, the light will split into two linearly polarized beams. One beam that parallel to the optical axis has refractive index of $n_e$. The other beam that perpendicular to the optical axis has refractive index of $n_o$. For the parallel beam ($n_e$), the refractive indices of SiC are $2.74+0i$ and $2.72+0i$ for incident laser and Raman scattering respectively. For the perpendicular beam ($n_o$), the refractive indices of SiC are $2.68+0i$ and $2.66+0i$ for incident laser and Raman scattering respectively. The reference thickness of the air layer is set as 0. The normalized enhancement factor $F$ increases to 1.47 as $\delta$ rises to 15 nm. The average separation distance increment at the TLG-SiC interface is obtained based on the Raman intensity enhancement. According to equations (5-1) to (5-3) and Figures 5.9-5.10, while the absorbed energy flux in TLG is $3.8\times10^{4}$ $Wm^{-2}$,

$\Delta T_I = 89.1\,\mathrm{K}$ , $\Delta T_\Gamma = 114.3\,\mathrm{K}$ , and $\chi_I = -0.00131\,/\mathrm{K}$ . The enhancement factor is determined as $F = 1.039$. Assume the original separation distance at the TLG-SiC interface is 2.1 nm (detailed later with AFM images), $F_o$ would be 1.015. After intensity enhancement by laser heating, $F_h$ would be 1.055. Therefore, the final separation distance after laser heating is 4.7 nm for both parallel- and perpendicular-beam cases. The calculated thickness increment of air layer between TLG and SiC is 2.6 nm and verified with AFM results. The surface height variations for the TLG-SiC and pure SiC samples are shown in Figure 5.10(b). Many ripples of TLG can be found in the AFM image. The height of the red line in the TLG image varies from 0.8 to 6.3 nm, with an average height of 2.1 nm. The height variation of pure Si is mainly concentrated in a range from 0.7-1.3 nm, with an average height of 0.3 nm.

From the above discussion, we can conclude a separation layer exists at the TLG-SiC interface, causing poor contact between epitaxial graphene and SiC substrate. The rough contact can be explained by the synthesis method of the TLG-SiC sample. During synthesis, the temperature is over 1300 °C, and the graphene and SiC has perfect match. When the sample is taken out of the oven, it cools down to room temperature. Graphene and SiC has different thermal expansion coefficients, so they will have different contraction, leading to interface delamination. Therefore, the interface resistance can be quite high.

### 5.4. Single Temperature Probing: CVD Graphene on Glass

Graphene has important application in electronics and semiconductor devices when it is attached on glass substrate. The contact condition and heat dissipation across the graphene-

glass interface is critical to the stability and safety of devices. In this section, the rough contact and phonon coupling at CVD graphene-glass interface is characterized. The SLG-glass sample is obtained from ACS Material. In synthesis, monolayer graphene is first fabricated on copper foil using the CVD method. PMMA is then deposited on SLG and cured. Etching process is taken to remove the copper foil. Finally, the SLG is transferred to glass and the PMMA is removed with acetone. The bonding between the SLG layer and glass substrate is van der Waals force, leading to a weak contact and large interfacial thermal resistance.

The experimental setup for the thermal resistance measurement of SLG-glass interface is the same with that for the TLG-SiC interface. The heating laser reaches the glass layer from below with an angle of 60° to the vertical direction. The refractive indices for SLG and glass are 2.69 and 1.44 respectively. About 92.4 % of the laser energy passes through the glass and reaches the SLG layer. The percentages of laser energy passing through the graphene are 83.6 %, 26.8 %, 2.9 %, and 0.9 % for the first four reflection process of light, respectively. The accumulated passing energy percentage is 114.2 %. A total of 2.63 % of incident laser energy can be absorbed in SLG during the light propagation. At the wavelength ($\lambda$ = 1550 nm) of the heating laser, little laser energy is absorbed in the glass. The graphene layer is heated up by the heating laser and dissipates heat crosses the interface to the glass substrate. A long integration time of 40 s is taken to collect strong Raman signals. The graphene layer is identified as monolayer according to the intensity ratio of 2D-band and G-band. The G-band of graphene is preferred for temperature probing of SLG layer. Since there is no Raman peak to characterize glass, the temperature of glass cannot be determined precisely. Here a

heat conduction model is employed to calculate the surface temperature of glass. Figure 5.11(a) shows the heat transfer model and the area of the graphene layer. Heat transfers from a graphene flake to a semi-infinite glass plate. The heat transfer rate, *q*, is expressed in the following equation: [119]

$$q = \zeta q_{ss}^{*} k_{glass} A_s \Delta T / L_c \tag{5-7}$$

where $q = 0.023 p A_s / A$, laser power $p = (0.1\text{-}1.6)$ W, laser spot size $A = 2.88\times10^{-6}$ m$^2$, $\zeta = 0.5$ for a semi-infinite plate, graphene surface area $A_s = 2wL$, $w = 1.74\times10^{-5}$ m, $L = 1.56\times10^{-5}$ m, characteristic length $L_c = (A_s/4\pi)^{1/2}$, thermal conductivity $k_{glass} = 1.4$ Wm$^{-1}$K$^{-1}$, dimensionless conduction heat rate $q_{ss}^{*} = 0.932$, and $\Delta T$ is the temperature rise of the glass surface. Under a laser power of 1.58 W, the temperature of glass increases by 6.6 K. The temperature rises of glass under different heat fluxes are calculated and shown in Fig. 5(c).

To determine the temperature rise of graphene, Raman linewidth, wavenumber, and intensity are employed. Calibration results for temperature coefficients of G-band of SLG are illustrated in Fig. 5(b). The temperature coefficients are 0.01791 cm$^{-1}$/K, -0.02471 cm$^{-1}$/K, and -0.00239 /K for linewidth, wavenumber, and normalized intensity, respectively. Temperature rises of graphene under different laser heat fluxes are probed and shown in Fig. 5(c). The fitting slopes of temperature rise against heat flux are $4.21\times10^{-3}$, $4.70\times10^{-3}$, and $2.21\times10^{-3}$ Km$^2$W$^{-1}$ based on linewidth, wavenumber, and intensity, respectively. The calculated slope of temperature rise of glass against heat flux is $4.54\times10^{-4}$ Km$^2$W$^{-1}$. Thus, the thermal resistances at the graphene-glass interface are determined as $3.76\times10^{-3}$, $4.25\times10^{-3}$,

and $1.76\times10^{-3}$ $Km^2W^{-1}$, with uncertainties of $1.47\times10^{-4}$, $1.23\times10^{-4}$, and $1.13\times10^{-4}$ $Km^2W^{-1}$, from the linewidth, wavenumber, and intensity methods, respectively. The large thermal resistance at the SLG-glass interface indicates rough contact between the two materials. A separation layer exists at the interface, which significantly slows the heat dissipation from graphene to glass. The thermal resistances calculated by wavenumber and linewidth agree well with each other. The difference of temperature obtained by wavenumber and linewidth lies in some heat induced thermal stress in graphene. The small difference illustrates that graphene experiences little stress. The bonding between graphene and glass is weak, and the graphene is loose. The thermal resistance based on intensity method is only 47 % of that

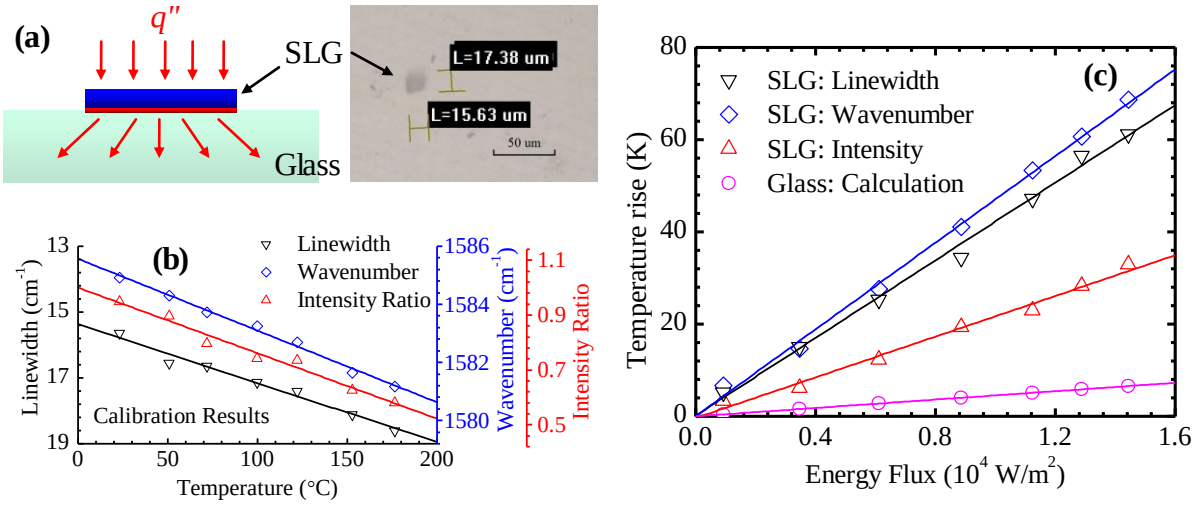


**Figure 5.11 Experimental results of interfacial thermal resistance and rough contact at SLG-glass interface. (a) Heat dissipation from SLG to glass substrate. Glass is treated as a semi-infinite plate. The area of SLG is shown in the right panel. (b) The fitting slopes for linewidth, wavenumber, and normalized intensity of SLG against temperature are 0.01791 $cm^{-1}$/K, -0.02471 $cm^{-1}$/K, and -0.00239 /K, respectively. (c) The fitting slopes of experimental temperature rise against laser heat flux are $4.21\times10^{-3}$, $4.70\times10^{-3}$, and $2.21\times10^{-3}$ $Km^2W^{-1}$ for linewidth, wavenumber, and intensity of SLG, respectively. A heat transfer model is employed to calculate the temperature rise of the glass substrate heated up by graphene. The slope of temperature rise of glass with heat flux is $4.54\times10^{-4}$ $Km^2W^{-1}$. Interfacial thermal resistance is determined as $3.76\times10^{-3}$ $Km^2W^{-1}$ according to the slope difference between linewidth of SLG and glass.**

based on linewidth, which further proves the rough contact at the interface as discussed for the SLG-Si, and TLG-SiC interfaces. The thermal expansion coefficient of glass is about $5.5\times10^{-7}$ $K^{-1}$, significantly different from that of graphene. The thermal expansion difference leads to mismatch in the laser heating. Light interference happens due to the existence of the separation layer between graphene and glass. The interference effect of the Raman signals at the SLG-air-glass interface enhances the Raman intensity. The intensity enhancement decreases the calculated temperature rise of graphene. Consequently, the thermal contact resistance based on intensity is smaller than that based on linewidth and wavenumber. According to the foregoing discussions, the contact between CVD monolayer graphene and glass substrate is poor. The separation of graphene and glass causes large thermal contact resistance at the interface.

The thermal contact resistances between CVD SLG/Si, epitaxial TLG/SiC, and CVD SLG/glass based on linewidth, wavenumber, and intensity methods are listed in Table 5.1. As linewidth is mainly dependent on temperature, the thermal resistances obtained by linewidth are close to reality. The results based on wavenumber agree qualitatively with the linewidth method, which indicates that little stress is experienced in graphene. The contact between graphene and substrate is rough. Raman intensity yielded smaller interfacial thermal resistances than linewidth and wavenumber, which further proves that air layer do exist between graphene and its substrate. The interfacial thermal resistances for CVD graphene-substrate are larger than that for epitaxial graphene/substrate. The original ripples of CVD graphene on substrate are deeper than that of epitaxial graphene. The bonding between CVD graphene and substrate is through a weak van der Waals force, while for epitaxial graphene,

it is a strong covalent bonding. The covalent bonding is more effectively for phonon transport due to its semimetallic or semiconducting characteristics [120]. After the same incident laser irradiation, the separation distance at the epitaxial-graphene/SiC interface is as large as that at the CVD-graphene/Si interface. The number of graphene layers is a main factor. The tri-layer graphene absorbs more laser energy than monolayer graphene, which leading to more temperature difference between the graphene and substrate. The increase in thermal expansion mismatch thus causes larger layer separation at the interface.

**Table 5.1 Interfacial thermal resistances for graphene/substrate with linewidth, wavenumber, and intensity methods**

| Sample | Thermal contact resistance [$K \cdot m^2 \cdot W^{-1}$] | | |
|---|---|---|---|
| | Linewidth | Wavenumber | Intensity |
| CVD SLG/Si | $5.46\times10^{-3}$ | $5.90\times10^{-3}$ | $3.53\times10^{-3}$ |
| Epitaxial TLG/SiC | $2.27\times10^{-3}$ | $2.26\times10^{-3}$ | $1.42\times10^{-3}$ |
| CVD SLG/Glass | $3.76\times10^{-3}$ | $4.25\times10^{-3}$ | $1.76\times10^{-3}$ |

# CHAPTER 6. CONCLUSIONS AND FUTURE WORK

## 6.1. Conclusions

Thermal response of a silicon substrate beneath silica particles under laser irradiation was probed based on Raman spectroscopy. The laser energy was focused within sub-wavelength areas inside the substrate by particles. Silica particles of three diameters (400, 800 and 1210 nm) under incident laser of four energy fluxes ($2.5 \times 10^8$, $3.8 \times 10^8$, $6.9 \times 10^8$ and $8.6 \times 10^8$ W/m$^2$) were used in the experiment. The results indicated that, the temperature rise increased as the particle size of silica increased. The incident laser intensity also had a positive effect on the near-field heating. Stronger laser irradiation resulted in a higher temperature rise in the substrate. The measurement was interpreted by optical and thermal field simulations. The highest electric field enhancement factors were 2.8 inside the silicon substrate and 6.0 inside the silica particle. The calculated highest temperature rise was 9.0 K inside the substrate under particles of 1210 nm diameter with an incident laser of $8.6 \times 10^8$ W/m$^2$, while the corresponding measured temperature rise was 55.8 K based on the Raman linewidth method, and 29.3 K based on the wavenumber method. For the effect of particle size, the modeling results agreed with the measurement qualitatively. The difference could be due to the pre-focused laser beam by the objective lens in the experiment, poor mesh quality in the HFSS simulation, and Raman signal from not-focused silicon wafer regions among particles.

Far-field nanoscale imaging of near-field focusing, thermal and stress fields in a silicon substrate beneath silica particles and glass fiber was conducted for the first time using Raman spectroscopy. Imaging based on Raman intensity decrease, wavenumber shift, and linewidth

broadening all reflected conjugated near-field focusing, thermal, and stress effects. Difference in the imaging based on these three parameters was largely induced by the non-coincidence between the laser focal center and the focal center of the Raman spectrometer backscattering path. Our detailed analysis revealed that such imaging can achieve a resolution better than 20 nm ($< \lambda/26$). The nanoscale imaging capacity was fully demonstrated by studying the near-field focus under silica particles from 1210 nm down to 160 nm. Physical methodologies were developed to separate the near-field focusing, thermal, and stress effects and evaluate the temperature rise and local stress in near-field focusing. Under 1210 nm monolayer silica particles, the temperature rise in the near-field focusing region in silicon substrate reaches 56.1 K under a laser fluence of $3.9 \times 10^9$ W/m$^2$, and the local stress is 370 MPa. The temperature rise and thermal stress in silicon under a 6.24 μm glass fiber induced laser heating are 33.0 K and 230 MPa, respectively. Our study under different energy levels revealed that the temperature rise and local stress increased almost linearly with the energy fluence. The electromagnetic and temperature fields inside the substrate-particle system were simulated to interpret the measured temperature rise with sound agreement.

The interfacial thermal characterization of graphene on substrates was carried out under laser heating by using Raman linewidth method. Energy coupling at the graphene-substrate interfaces was explored. The contacts were proved to be rough at the interfaces, and the average distances between graphene and substrate layers were calculated. The thermal contact resistances between CVD graphene/Si, epitaxial graphene/SiC, and CVD graphene/glass were probed as high as $5.46 \times 10^{-3}$, $2.27 \times 10^{-3}$, $3.76 \times 10^{-3}$ Km$^2$W$^{-1}$,

respectively. Lower thermal resistances in the molecule dynamics simulations predicted large separation distances between graphene and substrates. The thermal contact resistances based on wavenumber shift agreed qualitatively with the linewidth method. Little stress was experienced in graphene, and the graphene layer was loose on the substrates. Raman intensity yielded smaller interfacial thermal resistances than linewidth and wavenumber. It further proved that air layer did exist between graphene and substrates. Strategies were developed to calculate the thickness increment of the air layer between graphene and substrates based on light interference at the interface. AFM images were taken to verify the obtained thicknesses of air layers at both interfaces of graphene/Si and graphene/SiC.

## 6.2. Future Work

This research examines the Raman mapping and thermal characterization in the near-field laser heating. As an optical characterization method, Raman thermometry is capable of probing both temperature and stress of materials simultaneously. It has been broadly applied in thermal characterization of carbon nanotube, graphene, bismuth telluride, and other materials and micro-devices. Raman thermometry can also be used in time-resolved thermal characterization besides steady-state temperature and stress measurements. Transient temperature evolution of materials under joule heating can be probed by a modulated pulsed laser, as long as the pulsed probing laser can overcome the integration time required in collecting the Raman signals. In this case, the temporal resolution can be improved to the duration time of the modulated pulsed laser, which is on the order of several hundred microseconds. The transient thermal characterization would be a promising direction for the future work.

The interfacial thermal characterization examines the energy coupling capacity between graphene and its substrate. For three-layer nanomaterials, such as graphene/$Bi_2Te_3$/GaAs and graphene/BN/SiC, the work to characterize the thermal transport across their interfaces is valuable in their applications. The surface contact features at the graphene/substrate interfaces are examined in this work. Rough contact has been demonstrated and the separation distance between the graphene and substrate increases while it is under heating. Large thermal resistances impede the heat dissipation from graphene-based devices to a large extent. A new technique to smooth ripples of graphene on substrates is promising in speeding heat dissipation and improving electronic properties of graphene-based devices. It is also of great importance to develop new methods to characterize the surface variation of graphene at nano- and subnano-scale. Once ripples can be controlled and diminished to the minimum, the thermal contact resistance at the graphene/substrate interface would be reduced to a magnitude of $10^{-8}$ $Km^2W^{-1}$. The temperature differences between graphene and its substrate under heating would be pretty small. In this case, Raman thermometry is not preferred in thermal characterization across graphene/substrate interfaces. A new technique development to characterize the interfacial thermal transport is promising for the future research.

## REFERENCES


1. Bar, G., S. Rubin, R.W. Cutts, T.N. Taylor, and T.A. Zawodzinski Jr, *Dendrimer-Modified Silicon Oxide Surfaces as Platforms for The Deposition of Gold and Silver Colloid Monolayers: Preparation Method, Characterization, and Correlation between Microstructure and Optical Properties.* Langmuir, 1996. **12**(5): 1172-1179.
2. Endo, Y., M. Ono, T. Yamada, H. Kawamura, K. Kobara, and T. Kawamura, *A Study of Antireflective and Antistatic Coating with Ultrafine Particles.* Advanced Powder Technology, 1996. **7**(2): 131-140.
3. Sanders, J.V., *Colour of Precious Opal.* Nature, 1964. **204**(496): 1151-1153.
4. Bogomolov, V.N., S.V. Gaponenko, I.N. Germanenko, A.M. Kapitonov, E.P. Petrov, N.V. Gaponenko, A.V. Prokofiev, A.N. Ponyavina, N.I. Silvanovich, and S.M. Samoilovich, *Photonic Band Gap Phenomenon and Optical Properties of Artificial Opals.* Physical Review E, 1997. **55**(6): 7619-7625.
5. Park, J.S., S.O. Meade, E. Segal, and M.J. Sailor, *Porous Silicon-Based Polymer Replicas Formed by Bead Patterning.* Physica Status Solidi A-Applications and Materials Science, 2007. **204**(5): 1383-1387.
6. Shelekhina, V.M., O.A. Prokhorov, P.A. Vityaz, A.P. Stupak, S.V. Gaponenko, and N.V. Gaponenko, *Towards 3D Photonic Crystals.* Synthetic Metals, 2001. **124**(1): 137-139.
7. Xia, F. and L. Jiang, *Bio - Inspired, Smart, Multiscale Interfacial Materials.* Advanced Materials, 2008. **20**(15): 2842-2858.

8. Yang, M.X., D.H. Gracias, P.W. Jacobs, and G.A. Somorjai, *Lithographic Fabrication of Model Systems in Heterogeneous Catalysis and Surface Science Studies*. Langmuir, 1998. **14**(6): 1458-1464.

9. Aminuzzaman, M., A. Watanabe, and T. Miyashita, *Direct Writing of Conductive Silver Micropatterns on Flexible Polyimide Film by Laser-Induced Pyrolysis of Silver Nanoparticle-Dispersed Film*. Journal of Nanoparticle Research, 2010. **12**(3): 931-938.

10. Deckman, H.W., J.H. Dunsmuir, S. Garoff, J.A. Mchenry, and D.G. Peiffer, *Macromolecular Self-Organized Assemblies*. Journal of Vacuum Science & Technology B, 1988. **6**(1): 333-336.

11. Hayashi, S., Y. Kumamoto, T. Suzuki, and T. Hirai, *Imaging by Polystyrene Latex-Particles*. Journal of Colloid and Interface Science, 1991. **144**(2): 538-547.

12. Halfpenny, D.R. and D.M. Kane, *A Quantitative Analysis of Single Pulse Ultraviolet Dry Laser Cleaning*. Journal of Applied Physics, 1999. **86**(12): 6641-6646.

13. Li, L.P., Y.F. Lu, D.W. Doerr, D.R. Alexander, J. Shi, and J.C. Li, *Fabrication of Hemispherical Cavity Arrays on Silicon Substrates Using Laser-Assisted Nanoimprinting of Self-Assembled Particles*. Nanotechnology, 2004. **15**(3): 333-336.

14. Li, L.P., Y.F. Lu, D.W. Doerr, and D.R. Alexander, *Laser-Assisted Nanopatterning of Aluminium Using Particle-Induced Near-Field Optical Enhancement and Nanoimprinting*. Nanotechnology, 2004. **15**(11): 1655-1660.

15. Li, L.P., Y.F. Lu, D.W. Doerr, D.R. Alexander, and X.Y. Chen, *Parametric Investigation of Laser Nanoimprinting of Hemispherical Cavity Arrays*. Journal of Applied Physics, 2004. **96**(9): 5144-5151.

16. McLeod, E. and C.B. Arnold, *Subwavelength Direct-Write Nanopatterning Using Optically Trapped Microspheres.* Nature Nanotechnology, 2008. **3**(7): 413-417.

17. Piglmayer, K., R. Denk, and D. Bäuerle, *Laser-Induced Surface Patterning by Means of Microspheres.* Applied Physics Letters, 2002. **80**(25): 4693.

18. Chou, S.Y., P.R. Krauss, W. Zhang, L.J. Guo, and L. Zhuang, *Sub-10 nm Imprint Lithography and Applications.* Journal of Vacuum Science & Technology B, 1997. **15**(6): 2897-2904.

19. Chou, S.Y., P.R. Krauss, and P.J. Renstrom, *Imprint Lithography with 25-Nanometer Resolution.* Science, 1996. **272**(5258): 85-87.

20. Huang, S.M., M.H. Hong, B.S. Luk'yanchuk, Y.W. Zheng, W.D. Song, Y.F. Lu, and T.C. Chong, *Pulsed Laser-Assisted Surface Structuring with Optical Near-Field Enhanced Effects.* Journal of Applied Physics, 2002. **92**(5): 2495-2500.

21. Munzer, H.J., M. Mosbacher, M. Bertsch, J. Zimmermann, P. Leiderer, and J. Boneberg, *Local Field Enhancement Effects for Nanostructuring of Surfaces.* Journal of Microscopy, 2001. **202**(1): 129-135.

22. Born, M. and E. Wolf, *Principles of Optics: Electromagnetic Theory of Propagation, Interference and Diffraction of Light*. 7th ed, 1999, Cambridge: Cambridge University Press.

23. Mie, G., *Contributions to the Optics of Turbid Media, Particularly of Colloidal Metal Solutions.* Ann. Phys.(Leipzig), 1908. **25**(3): 377-445.

24. Luk'yanchuk, B.S., Y.W. Zheng, and Y.F. Lu, *Laser Cleaning of Solid Surface: Optical Resonance and Near-Field Effects.* High-Power Laser Ablation III, 2000. **4065**: 576-587.

25. Frey, H.G., F. Keilmann, A. Kriele, and R. Guckenberger, *Enhancing the Resolution of Scanning Near-Field Optical Microscopy by a Metal Tip Grown on an Aperture Probe*. Applied Physics Letters, 2002. **81**(26): 5030-5032.

26. Zenhausern, F., Y. Martin, and H.K. Wickramasinghe, *Scanning Interferometric Apertureless Microscopy - Optical Imaging at 10 Angstrom Resolution*. Science, 1995. **269**(5227): 1083-1085.

27. Taubner, T., D. Korobkin, Y. Urzhumov, G. Shvets, and R. Hillenbrand, *Near-field Microscopy Through a SiC Superlens*. Science, 2006. **313**(5793): 1595.

28. Liu, Z.W., S. Durant, H. Lee, Y. Pikus, N. Fang, Y. Xiong, C. Sun, and X. Zhang, *Far-Field Optical Superlens*. Nano Letters, 2007. **7**(2): 403-408.

29. Rust, M.J., M. Bates, and X.W. Zhuang, *Sub-Diffraction-Limit Imaging by Stochastic Optical Reconstruction Microscopy (STORM)*. Nature Methods, 2006. **3**(10): 793-795.

30. Wang, Z.B., W. Guo, L. Li, B. Luk'yanchuk, A. Khan, Z. Liu, Z.C. Chen, and M.H. Hong, *Optical Virtual Imaging at 50 nm Lateral Resolution with a White-Light Nanoscope*. Nature Communications, 2011. **2**: 218.

31. Rho, J., Z.L. Ye, Y. Xiong, X.B. Yin, Z.W. Liu, H. Choi, G. Bartal, and X.A. Zhang, *Spherical Hyperlens for Two-Dimensional Sub-Diffractional Imaging at Visible Frequencies*. Nature Communications, 2010. **1**: 143.

32. Smolyaninov, I.I., Y.J. Hung, and C.C. Davis, *Magnifying Superlens in the Visible Frequency Range*. Science, 2007. **315**(5819): 1699-1701.

33. Liu, Z.W., H. Lee, Y. Xiong, C. Sun, and X. Zhang, *Far-Field Optical Hyperlens Magnifying Sub-Diffraction-Limited Objects*. Science, 2007. **315**(5819): 1686.

34. Lee, J.Y., B.H. Hong, W.Y. Kim, S.K. Min, Y. Kim, M.V. Jouravlev, R. Bose, K.S. Kim, I.C. Hwang, L.J. Kaufman, C.W. Wong, P. Kim, and K.S. Kim, *Near-Field Focusing and Magnification Through Self-Assembled Nanoscale Spherical Lenses.* Nature, 2009. **460**(7254): 498-501.

35. Shi, L., S. Plyasunov, A. Bachtold, P.L. McEuen, and A. Majumdar, *Scanning Thermal Microscopy of Carbon Nanotubes Using Batch-Fabricated Probes.* Applied Physics Letters, 2000. **77**(26): 4295-4297.

36. Wischnath, U.F., J. Welker, M. Munzel, and A. Kittel, *The Near-Field Scanning Thermal Microscope.* Review of Scientific Instruments, 2008. **79**(7): 073708.

37. Yue, Y., X. Chen, and X. Wang, *Noncontact Sub-10 nm Temperature Measurement in Near-Field Laser Heating.* ACS Nano, 2011. **5**(6): 4466-4475.

38. Yue, Y., J. Zhang, and X. Wang, *Micro/Nanoscale Spatial Resolution Temperature Probing for the Interfacial Thermal Characterization of Epitaxial Graphene on 4H-SiC.* Small, 2011. **7**(23): 3324-3333.

39. Beechem, T., S. Graham, S.P. Kearney, L.M. Phinney, and J.R. Serrano, *Invited Article: Simultaneous Mapping of Temperature and Stress in Microdevices Using Micro-Raman Spectroscopy.* Review of Scientific Instruments, 2007. **78**(6): 061301.

40. Bauer, M., A.M. Gigler, C. Richter, and R.W. Stark, *Visualizing Stress in Silicon Micro Cantilevers Using Scanning Confocal Raman Spectroscopy.* Microelectronic Engineering, 2008. **85**(5-6): 1443-1446.

41. Reserbat-Plantey, A., L. Marty, O. Arcizet, N. Bendiab, and V. Bouchiat, *A Local Optical Probe for Measuring Motion and Stress in a Nanoelectromechanical System.* Nature Nanotechnology, 2012. **7**(3): 151-155.

42. Novoselov, K.S., A.K. Geim, S.V. Morozov, D. Jiang, Y. Zhang, S.V. Dubonos, I.V. Grigorieva, and A.A. Firsov, *Electric Field Effect in Atomically Thin Carbon Films.* Science, 2004. **306**(5696): 666-669.

43. Novoselov, K.S., A.K. Geim, S.V. Morozov, D. Jiang, M.I. Katsnelson, I.V. Grigorieva, S.V. Dubonos, and A.A. Firsov, *Two-Dimensional Gas of Massless Dirac Fermions in Graphene.* Nature, 2005. **438**(7065): 197-200.

44. Geim, A.K. and K.S. Novoselov, *The Rise of Graphene.* Nature Materials, 2007. **6**(3): 183-191.

45. Zhang, Y., Y.-W. Tan, H.L. Stormer, and P. Kim, *Experimental Observation of the Quantum Hall effect and Berry's Phase in Graphene.* Nature, 2005. **438**(7065): 201-204.

46. Balandin, A.A., S. Ghosh, W. Bao, I. Calizo, D. Teweldebrhan, F. Miao, and C.N. Lau, *Superior Thermal Conductivity of Single-Layer Graphene.* Nano Letters, 2008. **8**(3): 902-907.

47. Ghosh, S., I. Calizo, D. Teweldebrhan, E.P. Pokatilov, D.L. Nika, A.A. Balandin, W. Bao, F. Miao, and C.N. Lau, *Extremely High Thermal Conductivity of Graphene: Prospects for Thermal Management Applications in Nanoelectronic Circuits.* Applied Physics Letters, 2008. **92**(15): 151911-151913.

48. Lee, J.-U., D. Yoon, H. Kim, S.W. Lee, and H. Cheong, *Thermal Conductivity of Suspended Pristine Graphene Measured by Raman Spectroscopy.* Physical Review B, 2011. **83**(8): 081419-081414.

49. Ghosh, S., W. Bao, D.L. Nika, S. Subrina, E.P. Pokatilov, C.N. Lau, and A.A. Balandin, *Dimensional Crossover of Thermal Transport in Few-Layer Graphene.* Nature Materials, 2010. **9**(7): 555-558.

50. Evans, W.J., L. Hu, and P. Keblinski, *Thermal Conductivity of Graphene Ribbons from Equilibrium Molecular Dynamics: Effect of Ribbon Width, Edge Roughness, and Hydrogen Termination.* Applied Physics Letters, 2010. **96**(20).

51. Balandin, A.A., *Thermal Properties of Graphene and Nanostructured Carbon Materials.* Nature Materials, 2011. **10**(8): 569-581.

52. Bolotin, K.I., K.J. Sikes, J. Hone, H.L. Stormer, and P. Kim, *Temperature-Dependent Transport in Suspended Graphene.* Physical Review Letters, 2008. **101**(9): 096802-096804.

53. Du, X., I. Skachko, A. Barker, and E.Y. Andrei, *Approaching Ballistic Transport in Suspended Graphene.* Nature Nanotechnology, 2008. **3**(8): 491-495.

54. Wu, Y.Q., P.D. Ye, M.A. Capano, Y. Xuan, Y. Sui, M. Qi, J.A. Cooper, T. Shen, D. Pandey, G. Prakash, and R. Reifenberger, *Top-Gated Graphene Field-Effect-Transistors Formed by Decomposition of SiC.* Applied Physics Letters, 2008. **92**(9): 092102-092103.

55. Chen, Z., W. Jang, W. Bao, C.N. Lau, and C. Dames, *Thermal Contact Resistance between Graphene and Silicon Dioxide.* Applied Physics Letters, 2009. **95**(16).

56. Hopkins, P.E., M. Baraket, E.V. Barnat, T.E. Beechem, S.P. Kearney, J.C. Duda, J.T. Robinson, and S.G. Walton, *Manipulating Thermal Conductance at Metal-Graphene Contacts via Chemical Functionalization.* Nano Letters, 2012. **12**(2): 590-595.

57. Koh, Y.K., M.H. Bae, D.G. Cahill, and E. Pop, *Heat Conduction across Monolayer and Few-Layer Graphenes.* Nano Letters, 2010. **10**(11): 4363-4368.

58. Mak, K.F., C.H. Lui, and T.F. Heinz, *Measurement of the Thermal Conductance of the Graphene/$SiO_2$ Interface.* Applied Physics Letters, 2010. **97**(22).

59. Meyer, J.C., A.K. Geim, M.I. Katsnelson, K.S. Novoselov, T.J. Booth, and S. Roth, *The Structure of Suspended Graphene Sheets.* Nature, 2007. **446**(7131): 60-63.

60. Geringer, V., M. Liebmann, T. Echtermeyer, S. Runte, M. Schmidt, R. Ruckamp, M.C. Lemme, and M. Morgenstern, *Intrinsic and Extrinsic Corrugation of Monolayer Graphene Deposited on $SiO_2$.* Physical Review Letters, 2009. **102**(7).

61. Balkanski, M., R. Wallis, and E. Haro, *Anharmonic Effects in Light Scattering Due to Optical Phonons in Silicon.* Physical Review B, 1983. **28**(4): 1928-1934.

62. Menéndez, J. and M. Cardona, *Temperature Dependence of the First-Order Raman Scattering by Phonons in Si, Ge, and α-Sn: Anharmonic Effects.* Physical Review B, 1984. **29**(4): 2051-2059.

63. Konstantinović, M., S. Bersier, X. Wang, M. Hayne, P. Lievens, R. Silverans, and V. Moshchalkov, *Raman Scattering in Cluster-Deposited Nanogranular Silicon Films.* Physical Review B, 2002. **66**(16).

64. Hart, T., R. Aggarwal, and B. Lax, *Temperature Dependence of Raman Scattering in Silicon.* Physical Review B, 1970. **1**(2): 638-642.

65. Antunes, E.F., A.O. Lobo, E.J. Corat, V.J. Trava-Airoldi, A.A. Martin, and C. Veríssimo, *Comparative Study of First- and Second-Order Raman Spectra of MWCNT at Visible and Infrared Laser Excitation.* Carbon, 2006. **44**(11): 2202-2211.

66. Costa, S., E. Borowiak-Palen, M. Kruszyñska, A. Bachmatiuk, and R.J. Kalenczuk, *Characterization of Carbon Nanotubes by Raman Spectroscopy.* Materials Science, 2008. **26**(2): 433-441.

67. Su, Z., J. Sha, G. Pan, J. Liu, D. Yang, C. Dickinson, and W. Zhou, *Temperature-Dependent Raman Scattering of Silicon Nanowires.* The Journal of Physical Chemistry B, 2006. **110**(3): 1229-1234.

68. Yue, Y.N., J.C. Zhang, and X.W. Wang, *Micro/Nanoscale Spatial Resolution Temperature Probing for the Interfacial Thermal Characterization of Epitaxial Graphene on 4H-SiC.* Small, 2011. **7**(23): 3324-3333.

69. Iler, R.K., *Adhesion of Submicron Silica Particles on Glass.* Journal of Colloid and Interface Science, 1972. **38**(2): 496-&.

70. Fischer, U.C. and H. Zingsheim, *Submicroscopic Pattern Replication with Visible Light*. Journal of Vacuum Science and Technology, 1981. **19**(4): 881-885.

71. Deckman, H.W., *Natural Lithography*. Applied Physics Letters, 1982. **41**(4): 377.

72. Dimitrov, A.S., T. Miwa, and K. Nagayama, *A Comparison between the Optical Properties of Amorphous and Crystalline Monolayers of Silica Particles.* Langmuir, 1999. **15**(16): 5257-5264.

73. Denkov, N.D., O.D. Velev, P.A. Kralchevsky, I.B. Ivanov, H. Yoshimura, and K. Nagayama, *Mechanism of Formation of 2-Dimensional Crystals from Latex-Particles on Substrates.* Langmuir, 1992. **8**(12): 3183-3190.

74. Hulteen, J.C., D.A. Treichel, M.T. Smith, M.L. Duval, T.R. Jensen, and R.P. Van Duyne, *Nanosphere Lithography: Size-Tunable Silver Nanoparticle and Surface Cluster Arrays.* Journal of Physical Chemistry B, 1999. **103**(19): 3854-3863.

75. Micheletto, R., H. Fukuda, and M. Ohtsu, *A Simple Method for the Production of a 2-Dimensional, Ordered Array of Small Latex-Particles.* Langmuir, 1995. **11**(9): 3333-3336.

76. Hulteen, J.C. and R.P. Van Duyne, *Nanosphere Lithography: A Materials General Fabrication Process for Periodic Particle Array Surfaces.* Journal of Vacuum Science & Technology A: Vacuum, Surfaces, and Films, 1995. **13**(3): 1553-1558.

77. Ng, V., Y. Lee, B. Chen, and A. Adeyeye, *Nanostructure Array Fabrication with Temperature-Controlled Self-Assembly Techniques.* Nanotechnology, 2002. **13**: 554-558.

78. Wang, Y., L. Chen, H. Yang, Q. Guo, W. Zhou, and M. Tao, *Spherical Antireflection Coatings by Large-Area Convective Assembly of Monolayer Silica Microspheres.* Solar Energy Materials and Solar Cells, 2009. **93**(1): 85-91.

79. Prevo, B.G. and O.D. Velev, *Controlled, Rapid Deposition of Structured Coatings From Micro- and Nanoparticle Suspensions.* Langmuir, 2004. **20**(6): 2099-2107.

80. Garnett, E. and P. Yang, *Light Trapping in Silicon Nanowire Solar Cells.* Nano Letters, 2010. **10**(3): 1082-1087.

81. Huang, J., A.R. Tao, S. Connor, R. He, and P. Yang, *A General Method for Assembling Single Colloidal Particle Lines.* Nano Letters, 2006. **6**(3): 524-529.

82. Hsu, C.M., S.T. Connor, M.X. Tang, and Y. Cui, *Wafer-Scale Silicon Nanopillars and Nanocones By Langmuir–Blodgett Assembly and Etching.* Applied Physics Letters, 2008. **93**: 133109.

83. Jeong, S., L. Hu, H.R. Lee, E. Garnett, J.W. Choi, and Y. Cui, *Fast and Scalable Printing of Large Area Monolayer Nanoparticles for Nanotexturing Applications.* Nano Letters, 2010. **10**(8): 2989-2994.

84. Dimitrov, A.S. and K. Nagayama, *Continuous Convective Assembling of Fine Particles into Two-Dimensional Arrays on Solid Surfaces.* Langmuir, 1996. **12**(5): 1303-1311.

85. Doerk, G., C. Carraro, and R. Maboudian, *Temperature Dependence of Raman Spectra for Individual Silicon Nanowires.* Physical Review B, 2009. **80**(7).

86. Khachadorian, S., H. Scheel, A. Colli, A. Vierck, and C. Thomsen, *Temperature Dependence of First- and Second-Order Raman Scattering in Silicon Nanowires.* Physica Status Solidi (B), 2010. **247**(11-12): 3084-3088.

87. Tsu, R. and J.G. Hernandez, *Temperature Dependence of Silicon Raman Lines.* Applied Physics Letters, 1982. **41**(11): 1016-1018.

88. Novotny, L., R.X. Bian, and X.S. Xie, *Theory of Nanometric Optical Tweezers.* Physical Review Letters, 1997. **79**(4): 645-648.

89. Klemens, P.G., *Anharmonic Decay of Optical Phonons.* Physical Review, 1966. **148**(2): 845-848.

90. Tang, H. and I. Herman, *Raman Microprobe Scattering of Solid Silicon and Germanium at The Melting Temperature.* Physical Review B, 1991. **43**(3): 2299-2304.

91. Chen, Y., B. Peng, and B. Wang, *Raman Spectra and Temperature-Dependent Raman Scattering of Silicon Nanowires.* The Journal of Physical Chemistry C, 2007. **111**(16): 5855-5858.

92. Abel, M.R., S. Graham, J.R. Serrano, S.P. Kearney, and L.M. Phinney, *Raman Thermometry of Polysilicon Microelectromechanical Systems in the Presence of an Evolving Stress.* Journal of Heat Transfer-Transactions of the ASME, 2007. **129**(3): 329-334.

93. Weaver, J. and H. Frederikse, *Optical Properties of Selected Elements.* CRC Handbook of Chemistry and Physics, CRC Press, Boca Raton, 2001: 12-133.

94. Hulteen, J.C. and R.P. Van Duyne, *Nanosphere Lithography: A Materials General Fabrication Process for Periodic Particle Array Surfaces.* Journal of Vacuum Science & Technology A, 1995. **13**(3): 1553-1558.

95. Tang, X., Y. Yue, X. Chen, and X. Wang, *Sub-Wavelength Temperature Probing in Near-Field Laser Heating by Particles.* Optics Express, 2012. **20**(13): 14152-14167.

96. Kouteva-Arguirova, S., T. Arguirov, D. Wolfframm, and J. Reif, *Influence of Local Heating on Micro-Raman Spectroscopy of Silicon.* Journal of Applied Physics, 2003. **94**(8): 4946-4949.

97. Zheng, Y.W., B.S. Luk'yanchuk, Y.F. Lu, W.D. Song, and Z.H. Mai, *Dry Laser Cleaning of Particles From Solid Substrates: Experiments and Theory.* Journal of Applied Physics, 2001. **90**(5): 2135-2142.

98. Abel, M.R., *Thermal Metrology of Polysilicon MEMS using Raman Spectroscopy*, in *Mechanical Engineering*2005, Georgia Institute of Technology.

99. Schmidt, A.J., K.C. Collins, A.J. Minnich, and G. Chen, *Thermal Conductance and Phonon Transmissivity of Metal - Graphite Interfaces.* Journal of Applied Physics, 2010. **107**(10): 104907.

100. Nair, R.R., P. Blake, A.N. Grigorenko, K.S. Novoselov, T.J. Booth, T. Stauber, N.M.R. Peres, and A.K. Geim, *Fine Structure Constant Defines Visual Transparency of Graphene*. Science, 2008. **320**(5881): 1308-1308.

101. Graf, D., F. Molitor, K. Ensslin, C. Stampfer, A. Jungen, C. Hierold, and L. Wirtz, *Spatially Resolved Raman Spectroscopy of Single- and Few-Layer Graphene*. Nano Letters, 2007. **7**(2): 238-242.

102. Tang, X., S. Xu, and X. Wang, *Thermal Probing in Single Microparticle and Microfiber Induced Near-Field Laser Focusing*. Optics Express, 2013. **21**(12): 14303-14315.

103. Brenner, D.W., O.A. Shenderova, J.A. Harrison, S.J. Stuart, B. Ni, and S.B. Sinnott, *A Second-Generation Reactive Empirical Bond Order (REBO) Potential Energy Expression For Hydrocarbons*. Journal of Physics-Condensed Matter, 2002. **14**(4): 783-802.

104. Tersoff, J., *Empirical Interatomic Potential for Carbon, with Applications to Amorphous-Carbon*. Physical Review Letters, 1988. **61**(25): 2879-2882.

105. Dodson, B.W., *Development of a Many-Body Tersoff-Type Potential for Silicon*. Physical Review B, 1987. **35**(6): 2795-2798.

106. Hertel, T., R.E. Walkup, and P. Avouris, *Deformation of Carbon Nanotubes by Surface van der Waals Forces*. Physical Review B, 1998. **58**(20): 13870-13873.

107. Xiao, J.L., S. Dunham, P. Liu, Y.W. Zhang, C. Kocabas, L. Moh, Y.G. Huang, K.C. Hwang, C. Lu, W. Huang, and J.A. Rogers, *Alignment Controlled Growth of Single-Walled Carbon Nanotubes on Quartz Substrates*. Nano Letters, 2009. **9**(12): 4311-4319.

108. Ong, Z.Y. and E. Pop, *Molecular Dynamics Simulation of Thermal Boundary Conductance between Carbon Nanotubes and $SiO_2$*. Physical Review B, 2010. **81**(15).

109. Plimpton, S., *Fast Parallel Algorithms for Short-Range Molecular-Dynamics.* Journal of Computational Physics, 1995. **117**(1): 1-19.

110. Jiang, J.W., J.S. Wang, and B.W. Li, *Young's Modulus of Graphene: A Molecular Dynamics Study*. Physical Review B, 2009. **80**(11).

111. Watanabe, H., N. Yamada, and M. Okaji, *Linear Thermal Expansion Coefficient of Silicon from 293 to 1000 K*. International Journal of Thermophysics, 2004. **25**(1): 221-236.

112. Zhang, L., Z. Jia, L.M. Huang, S. O'Brien, and Z.H. Yu, *Low-Temperature Raman Spectroscopy of Individual Single-Wall Carbon Nanotubes and Single-Layer Graphene*. Journal of Physical Chemistry C, 2008. **112**(36): 13893-13900.

113. Calizo, I., A.A. Balandin, W. Bao, F. Miao, and C.N. Lau, *Temperature Dependence of the Raman Spectra of Graphene and Graphene Multilayers.* Nano Letters, 2007. **7**(9): 2645-2649.

114. Allen, M.J., J.D. Fowler, V.C. Tung, Y. Yang, B.H. Weiller, and R.B. Kaner, *Temperature Dependent Raman Spectroscopy of Chemically Derived Graphene.* Applied Physics Letters, 2008. **93**(19).

115. Tang, X., S. Xu, and X. Wang, *Nanoscale Probing of Thermal, Stress, and Optical Fields under Near-Field Laser Heating.* PLoS ONE, 2013. **8**(3): e58030.

116. Yoon, D., H. Moon, Y.W. Son, J.S. Choi, B.H. Park, Y.H. Cha, Y.D. Kim, and H. Cheong, *Interference Effect on Raman Spectrum of Graphene on $SiO_2$/Si.* Physical Review B, 2009. **80**(12).

117. Jung, N., A.C. Crowther, N. Kim, P. Kim, and L. Brus, *Raman Enhancement on Graphene: Adsorbed and Intercalated Molecular Species*. ACS Nano, 2010. **4**(11): 7005-7013.

118. Li, Z. and R.C. Bradt, *Thermal Expansion of the Hexagonal (4H) Polytype of SiC*. Journal of Applied Physics, 1986. **60**(2): 612-614.

119. Bergman, T.L., F.P. Incropera, A.S. Lavine, and D.P. DeWitt, *Fundamentals of Heat and Mass Transfer*. 7th ed, 2011: John Wiley & Sons.

120. Mattausch, A. and O. Pankratov, *Ab Initio Study of Graphene on SiC*. Physical Review Letters, 2007. **99**(7).